3D MODELING OF COUPLED ROCK DEFORMATION AND THERMO-PORO-MECHANICAL PROCESSES IN FRACTURES

A Dissertation

by

CHAKRA RAWAL

Submitted to the Office of Graduate Studies of
Texas A&M University
in partial fulfillment of the requirements for the degree of

DOCTOR OF PHILOSOPHY

May 2012

Major Subject: Petroleum Engineering

3D Modeling of Coupled Rock Deformation and Thermo-Poro-Mechanical Processes in Fractures

3D MODELING OF COUPLED ROCK DEFORMATION AND THERMO-PORO-MECHANICAL PROCESSES IN FRACTURES

A Dissertation

by

CHAKRA RAWAL

Submitted to the Office of Graduate Studies of
Texas A&M University
in partial fulfillment of the requirements for the degree of

DOCTOR OF PHILOSOPHY

Approved by:

Chair of Committee,	Ahmad Ghassemi
Committee Members,	Stephen A. Holditch
	Peter P. Valkó
	Theofanis Strouboulis
Head of Department,	A. Daniel Hill

May 2012

Major Subject: Petroleum Engineering

ABSTRACT

3D Modeling of Coupled Rock Deformation and Thermo-Poro-Mechanical Processes in Fractures. (May 2012)

Chakra Rawal, B.E.; M.Sc., Tribhuvan University

Chair of Advisory Committee: Dr. Ahmad Ghassemi

Problems involving coupled thermo-poro-chemo-mechanical processes are of great importance in geothermal and petroleum reservoir systems. In particular, economic power production from enhanced geothermal systems, effective water-flooding of petroleum reservoirs, and stimulation of gas shale reservoirs are significantly influenced by coupled processes. During such procedures, stress state in the reservoir is changed due to variation in pore fluid pressure and temperature. This can cause deformation and failure of weak planes of the formation with creation of new fractures, which impacts reservoir response. Incorporation of geomechanical factor into engineering analyses using fully coupled geomechanics-reservoir flow modeling exhibits computational challenges and numerical difficulties. In this study, we develop and apply efficient numerical models to solve 3D injection/extraction geomechanics problems formulated within the framework of thermo-poro-mechanical theory with reactive flow.

The models rely on combining Displacement Discontinuity (DD) Boundary Element Method (BEM) and Finite Element Method (FEM) to solve the governing

equations of thermo-poro-mechanical processes involving fracture/reservoir matrix. The integration of BEM and FEM is accomplished through direct and iterative procedures. In each case, the numerical algorithms are tested against a series of analytical solutions.

3D study of fluid injection and extraction into the geothermal reservoir illustrates that thermo-poro-mechanical processes change fracture aperture (fracture conductivity) significantly and influence the fluid flow. Simulations that consider joint stiffness heterogeneity show development of non-uniform flow paths within the crack. Undersaturated fluid injection causes large silica mass dissolution and increases fracture aperture while supersaturated fluid causes mineral precipitation and closes fracture aperture. Results show that for common reservoir and injection conditions, the impact of fully developed thermoelastic effect on fracture aperture tend to be greater compare to that of poroelastic effect.

Poroelastic study of hydraulic fracturing demonstrates that large pore pressure increase especially during multiple hydraulic fracture creation causes effective tensile stress at the fracture surface and shear failure around the main fracture. Finally, a hybrid BEFEM model is developed to analyze stress redistribution in the overburden and within the reservoir during fluid injection and production. Numerical results show that fluid injection leads to reservoir dilation and induces vertical deformation, particularly near the injection well. However, fluid withdrawal causes reservoir to compact. The Mandel-Cryer effect is also successfully captured in numerical simulations, i.e., pore pressure increase/decrease is non-monotonic with a short time values that are above/below the background pore pressure.

DEDICATION

To my beloved parents, my wife and siblings

ACKNOWLEDGEMENTS

I would like to express my deep and sincere gratitude to my advisor, Dr. Ahmad Ghassemi for his continuous enlightenment, academic guidance, encouragement and financial support. Dr. Ghassemi introduced me into the field of Rock Mechanics and provided me with the opportunity to learn and do research in Geomechanics.

I am grateful to Dr. Valkó for his valuable suggestions during various stages of my PhD studies. I would also like to acknowledge Dr. Strouboulis for providing much valuable information on numerical methods and Dr. Holditch for his valuable comments and suggestions that have shaped this dissertation.

I would also like to thank ExxonMobil Upstream Research Company and SAIC for providing me internship opportunities. I am especially thankful to Shekhar Gosavi, Sabodh K. Garg and John W. Pritchett for their precious support and guidance during my internship where I gained a lot of experiences and motivations for my research.

I thank my colleagues in Rock Mechanics group Xioxian Zhou, Sanghoon Lee, Jun Ge, and Reza for their constructive discussions and knowledge sharing over the years.

I would like to extend my heartfelt gratitude to my dear wife Bluena for her unconditional care and endless support during the preparation of this dissertation.

NOMENCLATURE

A	Fracture plane, m^2
B	Skempton's pore pressure coefficient
c	Concentration, ppm
c_0	Initial concentration, ppm
c_i	Injecting fluid concentration, ppm
c_{eq}	Equilibrium concentration, ppm
c_j	Joint cohesion, MPa
c^F	Fluid diffusivity, m^2/s
c_F	Specific heat of the fluid, J/(Kg.K)
c_R	Specific heat of the rock matrix, J/(Kg.K)
c^S	Solute diffusivity coefficient, m^2/s
c^T	Thermal diffusivity coefficient, m^2/s
D_n	Displacement discontinuity, m
D_F	fluid flux discontinuity, m/s
D_H	Heat flux discontinuity, W/m^2
D_S	Solute flux discontinuity, m/s
f_Q	Mineral fraction in the reservoir
G	Shear modulus, MPa

k	Rock matrix permeability, md
K	Bulk Modulus, MPa
K_f	Reaction rate constant, m/s
K_R	Thermal conductivity of reservoir matrix, W/(m.K)
K_n	Joint normal stiffness, MPa/m
TN	Total number of element nodes
M	Total number of elements
$\mathbf{N}^{(m)}$	Element shape function
n	Outward normal to surface
p	Excess pore pressure, MPa
p_0	Ambient reservoir pore pressure, MPa
p_n^{cD}	Pore pressure caused by a continuous displacement discontinuity, MPa
p^{cF}	Pore pressure caused by a continuous fluid source, MPa
p^{cH}	Pore pressure caused by a continuous heat source, MPa
p_n^{iD}	Pore pressure caused by an instantaneous displacement discontinuity, MPa
p^{iF}	Pore pressure caused by an instantaneous fluid source, MPa
p^{iH}	Pore pressure caused by an instantaneous heat source, MPa
p_i	Pressure at injection well, MPa
p_e	Pressure at extraction well, MPa
q	Fluid discharge in the fracture, m^2/s

q_H	Heat source intensity, W/m^2
q_S	Solute source intensity, m/s
Q_i	Fluid injection rate, m^3/s
Q_e	Fluid extraction rate, m^3/s
v_L	Fluid leak-off velocity, m/s
T	Temperature, K
t	Time, s
T_R	Rock temperature, K
T_i	Injection fluid temperature, K
T_0	Ambient rock temperature, K
u_i	Solid displacement components, m
w	Fracture aperture, m
w_0	Initial fracture aperture, m
$\mathbf{x}$	Vector of influence point coordinates, m
$\mathbf{x}'$	Vector of influencing point coordinates, m

Greek symbols

α	Biot's effective stress coefficient
α_T	Linear thermal expansion coefficient, 1/K
β_s	Volumetric thermal expansion coefficient, 1/K

δ	Dirac delta function
ε_{ij}	Strain components
ε	Volumetric strain
μ	Viscosity of the fluid, Pa-s
υ	Drained Poisson's ratio
υ_u	Undrained Poisson's ratio
ϕ	Joint friction angle, degree
ρ_F	Density of the fluid, Kg/m^3
ρ_Q	Density of the mineral, Kg/m^3
ρ_R	Bulk density of the reservoir matrix, Kg/m^3
σ_{nn}^{cD}	Stress components caused by a continuous displacement discontinuity, MPa
σ_n^{cF}	Stress components caused by a continuous fluid source, MPa
σ_n^{cH}	Stress components caused by a continuous heat source, MPa
σ_{n0}	Initial stress components, MPa
σ_n	Normal stress component to fracture, MPa
σ_v	Vertical in-situ stress, MPa
σ_h	Minimum horizontal in-situ stress, MPa
σ_H	Maximum horizontal in-situ stress, MPa

TABLE OF CONTENTS

Page

Page

LIST OF FIGURES

Page

Page

Page

Page

Page

LIST OF TABLES

Page

1. INTRODUCTION

1.1 Reservoir Geomechanics

Geomechanics has an important role in petroleum and geothermal systems that are naturally fractured or exhibit stress-sensitivity. Understanding of geomechanical aspects is essential in successful exploitation of resources from the subsurface. The properties of the "intact" rock and the discontinuities within the rock mass both contribute to the mechanical and hydraulic behavior of petroleum and geothermal reservoirs. In addition, the stress state in the reservoir and its variation in time and space are key in many aspects of field development such as hydraulic fracturing, injectivity and injection induced fracturing (Coats 1982; Chen et al. 1995; Koutsabeloulis and Hope 1996; Settari and Mourits 1998).

The significance of geomechanical effects has resulted in progresses towards incorporation of geomechanics factor into reservoir engineering analyses. In particular, the influence of coupling between stress, pressure and temperature and chemistry within a single framework is becoming increasingly necessary in reservoir management.

This dissertation follows the style of *SPE Journal.*

1.2 Overview of Coupled Processes

Coupled poro-thermo-chemo-mechanical processes are observed in response to injection/production of the fluid from the subsurface. They impact the reservoir reaction by affecting rock deformation and thus, fracture and matrix permeability. To investigate the effects of fluid injection and production procedures while considering coupled processes, usually a three-dimensional numerical modeling is necessary. An efficient numerical model with suitable discretization procedures can be devised to solve non-linear partial differential and integral equations governing the coupled behavior.

Simulating chemical and thermo-poro-mechanical processes in fracture-matrix system involves solving equations that describe transport within the fracture and poro-mechanical rock matrix deformation, fluid diffusion, heat transport, and solute transport/reactions. These are obtained by considering constitutive models, transport and balance laws (e.g., fluid momentum, fluid continuity) and are generally coupled and occur in an inhomogeneous rock mass that require complex numerical solutions. Various methodologies and solution strategies have been proposed from the interest of geological, geothermal (Kohl and Hopkirk 1995; Rutqvist et al. 2001; Rutqvist et al. 2006; Ghassemi and Zhou 2011) and petroleum applications (Settari and Mourits 1998; Gui et al. 2007; Yin et al. 2010).

In geothermal reservoirs, heat energy is extracted by circulating injected fluid in natural and/or hydraulically created fractures, creating pathways for fluid flow. During extraction of the thermal energy, fluid that flows through natural fracture/fracture

networks interacts with adjacent matrix. The interaction leads to the variation in fracture geometry and alteration in fracture permeability in response to mechanical, thermal and chemical processes. Such phenomena have been reported from the studies of Coso and Geysers geothermal fields (Rutqvist et al. 2006). Early works on coupled poroelastic fracture deformation and fluid injection and extraction has been formulated with the assumption of uniform pressure and one-dimensional fluid and heat diffusion in reservoir matrix (Nygren and Ghassemi 2006). In similar fashion, Ghassemi and Zhang (2006) studied the combined influence of poroelastic and thermoelastic processes on evolution of width of a stationary, uniformly pressurized and cooled fracture. However, three-dimensional studies have demonstrated the importance of coupling, for example, significant impact of poro-thermoelastic stresses on crack aperture and potentially on reservoir seismicity (Sekine and Mura 1980; Kohl et al. 1995; Kolditz and Clauser 1998; Mossop 2001; Ghassemi et al. 2003, 2007) and importance of joint slip under geothermal injection procedure introducing time dependent fracture slip and induced seismicity (Ghassemi et al. 2008; Zhou et al. 2009).

Aspects of coupling between chemical process with thermal and mechanical response of the geothermal reservoirs during injection and extraction procedures have been studied using two-dimensional numerical formulations (Kumar and Ghassemi 2005; Ghassemi and Kumar 2007). It has been observed that the thermoelastic effects dominate near the injection region when compared to those of poroelasticity and under some conditions silica reactivity may govern permeability.

Kohl et al.(1995), Kohl and Hopkirk (1995) and Ghassemi and Zhou (2011) have studied hydraulic, thermal and elastic perturbations arising from poroelastic and thermoelastic effects in hydraulic fracture and joints. However, chemical reactivity was not treated. Similarly, problem of non-isothermal reactive flow in fracture has also been treated both in the context of geological problems and geothermal reservoir development [see, for example, Pruess (1991), Wells and Ghiorso (1991), and Xu and Pruess (1998; 2001)], however, chemical, mechanical and thermal mechanisms were not coupled.

Furthermore, numerical as well as experimental examinations have shown the importance of dissolution, precipitation and pressure solution within rock fractures during fluid injection at geothermal sites (Liu et al. 2006; Yasuhara and Elsworth 2006; Taron and Elsworth 2009). Moreover, experimental studies (Carroll et al. 1998; Johnson et al. 1998; Dobson et al. 2003) show that chemical precipitation and dissolution of minerals can significantly affect fracture aperture.

The response of formation in the form of rock deformation and failure by fracture initiation and/or activation of discontinuities such as joints and bedding planes during hydraulic fracturing and fluid injection procedures has been the subject of many studies (Koning 1985; Perkins and Gonzalez 1985; Warpinski et al. 2001; Palmer et al. 2005, 2007; Ge and Ghassemi 2008), however, literature pertaining to the subject of rock failure around hydraulic fracture is limited. Warpinski et al. (2001) presented a semi-analytical method to calculate the stress and pore pressure variations induced by a hydraulic fracture and evaluated the likelihood and potential causes of micro-seismic activity in the vicinity of a major fracture. The semi-analytical method was based on

simple crack geometry and approximation of the pore pressure in the reservoir without flow considerations in the fracture. Palmer et al. (2007) adopted a 2D model to study the impact of stimulation of Barnett Shale on permeability enhancement. Ge and Ghassemi (2008) also used a 2D approach and studied the impact of the in-situ stress, pore pressure, as well as poroelastic and thermoelastic phenomena on the rock failure around a hydraulic fracture. The resulting stresses were also used to calculate the stimulated volume and permeability enhancement.

In petroleum engineering problems of coupled fluid flow and reservoir geomechanics, the interactions of solid mechanics and fluid flow have been studied and various techniques have been evolved over the years (Fung et al. 1994; Chin et al. 1998; Settari and Mourits 1998; Rutqvist et al. 2001; Tran et al. 2002; Gui et al. 2007; Krogstad and Durlofsky 2007; Yin et al. 2010).

In early works for coupled stress modeling with reservoir simulation, linear elasticity has been a popular choice. However, extensive experimental data on hydrocarbon reservoir rocks indicate extremely complex constitutive behavior at elevated pore pressure and temperature, which can only be solved using coupled modeling approach. In petroleum reservoir engineering systems, most commonly “one-way coupling” or “partial coupling” between the reservoir simulation and the geomechanics model was used. This coupling provides the weakest link between reservoir flow and deformation and therefore referred as “one-way” since the information is transferred only in one way from a simulator to a geomechanics model.

This means changes in the pore pressure field induce changes in stress and strains, but changes in the stress and strain do not affect pore pressure.

An improvement over “one-way coupling” between the reservoir simulation and geomechanics model is the “two-way full coupling”. In this category, mainly two schemes– “iteratively coupled” and “fully coupled” exist. In “iteratively coupled”, the reservoir flow variables and geomechanics variables are solved separately and sequentially by a reservoir simulator and geomechanics model and the coupling terms are iterated on at each time step. The coupling iteration is controlled by a convergence criterion that is usually based on pressure or stress change between two iterations of the solution. The iterative method consists of a repeated solution of the flow and stress equations during the timestep (Settari and Mourits 1998; Tran et al. 2002; Thomas et al. 2003; Gai et al. 2005; Bagheri and Settari 2008).

In fully coupled schemes, field variables such as pressure, temperature and geomechanical response such as displacements are calculated simultaneously through a system of equations with pressure, temperature and displacements as unknowns. The method is also called implicit coupling since the whole system is discretized on one grid domain and solved simultaneously. The fully coupled approach has the advantages of internal consistency. However, fully coupled models are not widely used in large scale numerical problems because of large development effort and are difficult and expensive to use and its due to the larger matrix bandwidth associated with fully implicit approach (Pointing et al. 1983; Fung 1992; Li and Zienkiewicz 1992; Tortike and Ali 1993;

Gutierrez and Lewis 1998; Lewis and Schrefler 1998; Osorio et al. 1999; Settari and Walters 2001; Dean et al. 2003).

Moreover, the importance of coupled modeling is of great interest (Lewis et al. 1991; Gutierrez et al. 2001; Yale 2002). It has pointed out that uncoupled or simplified geomechanical parameter model has shown to be insufficient in representing aspects of rock behavior. Also, predictions made with the coupled model are closer to what is observed experimentally, e.g., in a subsidence problem (Lewis et al. 1991).

1.3 Motivation and Objectives of the Study

Problems such as fluid injection/extraction, hydraulic fracturing and reservoir layer deformation are complex. This is particularly true when attempting to solve in the framework of thermo-poroelasticity. These complex problems are characterized by fluid flow and rock deformation, heat transfer and fracture propagation. The difficulties arise from solid-fluid coupling and the challenge is to correctly and adequately represent the reservoir response. The effects of interaction between fluid with the rock matrix and discontinuities can be studied by considering thermal, mechanical, chemical processes in problem formulation and solutions and it is only possible with numerical methods.

Although there are several numerical models addressing the coupling mechanism, often they lack the complete representation or expensive to use due to the large domain. Therefore, we attempt to achieve the advantage of Boundary Element Method in solving of the problems in infinite domains, integrated with Finite Element Method for its superiority in solving the flow-deformation systems, to present a hybrid BEFEM model

for solving problems of coupled reservoir geomechanics and fluid flow. We adopt direct and iterative procedures to integrate these two methods. The computational ease in coupling basic reservoir geomechanics and fluid flow is the attraction of this hybrid approach. The objective of this study is to develop a numerical model to study poro-thermo-mechanical processes in problems such as:

1) Injection and extraction in fracture in geothermal reservoir
2) Stress and rock failure analysis around hydraulic fractures
3) Reservoir deformation during injection and production

1.4 Dissertation Outline

In Section **2**, we describe the theory of coupled deformation-diffusion processes within the framework of extended theory of poro-thermoelasticity and theory of silica transport and its reactivity. The subsections cover these discussions– formulation of theory of poro-thermoelasticity, transport mechanisms and rock deformation.

In Section **3**, we explain the modeling approach and basis of numerical methods adopted to formulate the hybrid BEFEM model. Fundamentals of each module (thermo-poroelastic and -chemo, poroelastic hydraulic fracturing and poroelastic reservoir layer deformation) in integrated BEFEM are elucidated in separate subsections for clarity.

In Section **4**, we then verify the developed hybrid BEFEM model with known analytical solutions such as uniformly pressurized crack, classical one-dimensional consolidation and Mandel’s problem.

In Section **5**, we apply the hybrid BEFEM model to the problems of fracture response to non-isothermal reactive flow in the geothermal systems, hydraulic fracture simulation and reservoir layer deformation.

2. THERMO-PORO-MECHANICAL AND TRANSPORT PROCESSES

Freely moving fluid in porous media in the subsurface modifies its mechanical response. Characteristics of fluid and solid interactions in the rock govern the coupled processes relating pore pressure, temperature and dilation of rock. The foundation work that led to consideration of coupled poro-mechanical processes is the solution of soil consolidation problem by Terazaghi (1923). He proposed the one-dimensional consolidation theory which considers the influence of pore fluid diffusion on quasi-static deformation of soils. Biot (1941) formed the general theory of three-dimensional consolidation, which later named by theory of poroelasticity by Geertsma (1966). It accounts the coupled mechanisms between solid and fluid including (i) solid-fluid coupling: change in applied stress produces a change in fluid pressure or fluid mass and (ii) fluid-to-solid coupling: a change in fluid pressure or fluid mass produces a change in the volume of the porous material.

Rice and Cleary (1976) reformulated Biot's linear poroelasticity theory in terms of poroelastic parameters which emphasized two limiting behaviors of a fluid-filled porous material namely, drained and undrained and the constituent compressibilities. Their presentation simplifies the coupled deformation/diffusion field equations and is analogous to coupled thermoelasticity. Fundamentally, the same theory has been extended in soil mechanics (Verruijt 1969), in non-isothermal field (McTigue 1986; Kurashige 1989; Li et al. 1998) and in a chemically-active environment (Heidug and Wong 1996; Ghassemi and Diek 2003).

2.1 Thermo-Poroelasticity and Deformation of Rock Matrix

Thermo-poroelasticity introduces the theory of heat flow in porous fluid flow. It is based on Biot's original theory of poroelasticity generalized to consider thermal effects, which fully couples the rock deformation and temperature field. The basic approach is to introduce constitutive equations by extending the Biot's poroelastic theory for the non-isothermal case, so the transient heat transfer process is coupled with poroelastic behavior (Small et al. 1976; Aboustit et al. 1982; Palciauskas and Domenico 1982; McTigue 1986; Coussy 1989; Kurashige 1989; Chen 1992; Lewis and Schrefler 1998; Pao et al. 2001). It is important in investigating rock deformation and fracture permeability evolution during geothermal energy extraction, also such analysis can be extended to design hydraulic fracture stimulation, e.g., thermal cracking, when thermal effects are taken into account. Heat transfer "in or out" (thermal loading) can appreciably change the surrounding stress and pore pressure field in fluid-saturated porous rock and it induces volumetric deformation in response to expansion/contraction of both the pore fluid and the rock solid. For example, while cooling the rock, the contraction of the fluid can lead to a significant decrease in pore pressure when the pore space is confined, however, this phenomenon is reverse in case of rock heating.

Although heat transfer can alter pore pressure and volumetric stress, generally, the influences of fluid and rock matrix deformation on the temperature field are negligible. Therefore, heat flux and temperature can be calculated independently without the

contribution of pore pressure and stresses. The main mechanism of thermo-poroelastic process can be summarized as:

(1) Change in pore pressure and volumetric stresses due to rock heating/cooling

(2) Volumetric deformation of rock due to change in pore pressure

(3) Change in pore pressure due to rock compression/expansion

The theory of thermo-poroelasticity is derived by considering the typical linear elastic assumptions as well as following:

(1) Homogeneous, isotropic, infinite porous medium

(2) Transient fluid flow governed by Darcy's Law

(3) Transient linear heat conduction

(4) Constant material parameters

2.1.1 Governing Equations of Thermo-Poroelasticity

The governing equations of thermo-poroelasticity can be found from works of McTigue (1986) and Coussy (1989). The constitutive equations, transport laws and balance laws are summarized below:

2.1.1.1 Constitutive Equations

In isotropic thermo-poroelasticity, the constitutive equations comprise of deviatoric and volumetric response of the solid and the fluid (volumetric only). The deviatoric strain components are given as:

$$\varepsilon_{ij} = \frac{\sigma_{ij}}{2G}, i \neq j \quad \text{.....(2.1)}$$

where ε_{ij} is the total strain tensor, σ_{ij} is the stress tensor and G is the shear modulus. Here, the summation convention is used over repeated indices. Similarly, the volumetric response of the solid contains both hydraulic and thermal coupling terms:

$$\varepsilon_{kk} = \frac{\sigma_{kk}}{3K} + \frac{\alpha p}{K} + \beta_s T \quad \text{.....(2.2)}$$

where ε_{kk} (also denoted as ε) is volumetric strain, $\frac{\sigma_{kk}}{3}$ is volumetric stress (mean stress), p is pore pressure and T is temperature change. The constant K is the bulk modulus of rock, α is Biot's effective stress coefficient, which can be computed using $\alpha = \left(1 - K / K_s\right)$, where K_s is the bulk modulus of solid grains; β_s is the volumetric thermal expansion coefficient of the bulk solid under constant pore pressure and stress.

Note that Eq. 2.1 (with Eq. 2.2) degenerates to classical elastic relation without the pore pressure term and temperature term. Eq. 2.2 can also be written in stress form as:

$$\sigma_{ij} = 2G\varepsilon_{ij} + \frac{2G\upsilon}{1-2\upsilon}\varepsilon_{kk}\delta_{ij} - \alpha p\delta_{ij} + K\beta_s T\delta_{ij} \quad \text{.....(2.3)}$$

The volumetric response of the fluid can be written as (influx positive):

$$\zeta = \frac{\alpha}{3K}\sigma_{ij} + \frac{\alpha p}{BK} - \phi\left(\beta_f - \beta_s\right)T \quad \text{.....(2.4)}$$

where ζ is the variation of the fluid content per unit volume of the porous material, B is Skempton's pore pressure coefficient, β_f is volumetric thermal expansion coefficient

of the fluid and ϕ is porosity. Physical meaning of B is the increase in pore pressure due to an increase of mean stress under isothermal undrained condition $(\zeta = 0)$.

Eq. 2.4 can be written in terms of pore pressure as:

$$p = M\left(\zeta - \alpha\sigma_{kk} + \beta_m T\right) \quad \text{.....(2.5)}$$

where M is the Biot modulus given as $M = \dfrac{BK}{\alpha(1 - B\alpha)}$ and β_m is the hydro-thermal expansion coefficient given as $\beta_m = \alpha\beta_s + \phi\left(\beta_f - \beta_s\right)$.

2.1.1.2 Transport Laws

The transient fluid flow in porous rocks is governed by the well-known Darcy's law, which can be described as:

$$q_i = -\kappa p_{,i} \quad \text{.....(2.6)}$$

where q_i is the fluid flux (fluid volume per unit area per unit time); κ is defined as k/μ (k is the intrinsic permeability having dimension of length squared and μ the fluid dynamic viscosity).

The heat flow is governed by Fourier's law, which is written as:

$$q_i^T = -K_R T_{,i} \quad \text{.....(2.7)}$$

Here, q_i^T is the heat flux and K_R is the thermal conductivity. One can see that the transport laws for fluid flow and heat flow are analogous to each other.

2.1.1.3 Balance Laws

For local stress balance, standard considerations of static equilibrium lead to the equilibrium equation used in elasticity:

$$\sigma_{ij,j} = 0 \quad \text{.....(2.8)}$$

Considerations of mass conservation for a compressible fluid yield the local continuity equation:

$$\frac{\partial \zeta}{\partial t} + q_{i,i} = 0 \quad \text{.....(2.9)}$$

Similarly, the energy balance equation can be expressed as:

$$\rho_R c_R \frac{\partial T}{\partial t} + q^T_{i,i} = 0 \quad \text{.....(2.10)}$$

where ρ_R and c_R are the rock density and specific heat capacity respectively.

2.1.1.4 Field Equations of Thermo-Poroelasticity

Using the constitutive, transport and balance laws presented earlier, the field equations for temperature (T), displacement (u_i) and pore pressure (p) are derived next. First, by substituting the stress from Eq. 2.3 into equilibrium equation (Eq. 2.8), the Navier-type equation for thermo-poroelasticity is obtained as:

$$G\Delta^2 u_i + \frac{1}{3}(G + 3K)\varepsilon_{,i} = \alpha p_{,i} + K\beta_s T_{,i} \quad \text{.....(2.11)}$$

The fluid diffusion equation is obtained by inserting Darcy's law (Eq. 2.6) and the constitutive pore pressure relation (Eq. 2.5) into the continuity equation (Eq. 2.9) as:

$$\kappa\Delta^2 p = \frac{1}{M}\frac{\partial p}{\partial t} + \alpha\frac{\partial \varepsilon}{\partial t} - \beta_m \frac{\partial T}{\partial t} \quad \text{……(2.12)}$$

Furthermore, the heat diffusion equation is derived by inserting Fourier's law (Eq. 2.7) into the energy balance equation (Eq. 2.10):

$$c^T \Delta^2 T = \frac{\partial T}{\partial t} \quad \text{……....(2.13)}$$

In the above equations, u_i denotes the solid displacement vector and c^T represents thermal diffusivity. As mentioned above, heat transfer is calculated separately because stress and pressure changes do not significantly alter the temperature field. Also, note that convective heat transport is neglected.

There are ten independent parameters needed for thermo-poroelastic theory (e.g., $K, G, \alpha, B, \kappa, \beta_s, \beta_f, c^T, K_R, \gamma_f$). Among them, five parameters $(K, G, \alpha, B, \kappa)$ from poroelasticity, with (K, G) as the pure elastic parameters.

2.1.1.5 Field Equations of Poroelasticity and Thermoelasticity

Poroelasticity and thermoelasticity can be considered as two special cases for thermo-poroelasticity. Derivations of field equations for isothermal poroelasticity can be found in the literature [see, for example, Rice and Cleary (1976), and Detournay and Cheng (1993)]. These equations can also be found from the thermo-poroelastic ones by neglecting the thermal effect. For example, letting $T = 0$ in Eqs. 2.11 and 2.12, the Navier-type equation for solid displacement and diffusion equation for pore pressure are expressed as:

$$G\Delta^2 u_i + \frac{1}{3}(G+3K)\varepsilon_{,i} = \alpha p_{,i} \quad \text{.....(2.14)}$$

$$\kappa\Delta^2 p = \frac{1}{M}\frac{\partial p}{\partial t} + \alpha\frac{\partial \varepsilon}{\partial t} \quad \text{.....(2.15)}$$

Similarly, neglecting the pore pressure term from the field equation of thermo-poroelasticity (Eq. 2.11), it will result field equations for thermoelasticity:

$$G\Delta^2 u_i + \frac{1}{3}(G+3K)\varepsilon_{,i} = K\beta_s T_{,i} \quad \text{.....(2.16)}$$

Diffusion equation for temperature (T) is the same as the thermo-poroelastic Eq. 2.13 in which effects of pore pressure and stress on temperature are ignored. Derivations of thermoelasticity equations and poroelasticity equations are analogous and the theories have been discussed in detail [see, for example, Rice and Cleary (1976), McTigue (1986) and Norris (1992)].

2.1.2 Thermo-Poroelastic Constant Relationships

$$M = \frac{2GB^2(1-2\upsilon)(1+\upsilon_u)^2}{9(\upsilon_u-\upsilon)(1-2\upsilon_u)} \quad \text{.....(2.17)}$$

$$\alpha = \frac{3(\upsilon_u-\upsilon)}{B(1-2\upsilon)(1+\upsilon_u)} \quad \text{.....(2.18)}$$

$$c^F = \frac{2\kappa B^2 G(1-\upsilon)(1+\upsilon_u)^2}{9(1-\upsilon_u)(\upsilon_u-\upsilon)} \quad \text{.....(2.19)}$$

$$c^T = \frac{K_R}{\rho_R c_R} \quad \text{.....(2.20)}$$

where c^F is the fluid diffusivity, also known as generalized consolidation coefficient.

2.2 Transport Equations in the Fracture

For fracture-matrix system, in addition to governing equations for thermo- and poro-elastic diffusion/deformation in rock-matrix, transport equations in the fractures are needed. For a complete representation of thermo-poroelastic and reactivity analysis of rock-matrix system, the fluid, heat and solute flow in the fracture are described in following subsections.

2.2.1 Fluid Flow in the Fracture

The general phenomenon of fluid flow in the fracture is described by Navier-Stokes equation, which relates the flow velocity to the pressure gradient, body force and viscous force (Batchelor 1967; Zimmerman and Bodvarsson 1996). A simpler form of Navier-Stokes equation can be obtained with the assumptions that the fracture aperture is of smaller magnitude than fracture length and varies smoothly such that the lubrication theory applies, e.g., well-known “cubic law” (Witherspoon et al. 1980). The momentum balance for the fluid can be written in terms of pressure in the fracture as (see Appendix A for derivation):

$$\nabla p(x,y,0,t) = -\frac{12\mu}{w^3(x,y,t)}\mathbf{q}(x,y,t) \quad \text{.....(2.21)}$$

where p is the fluid pressure in the fracture, μ is the fluid viscosity; w is the fracture aperture, $\mathbf{q} = v(x,y,t)w(x,y,t)$ is the fluid flux and ∇ is the gradient operator. The rectilinear axes x and y are in the fracture plane $(z=0)$ and t is time.

Similarly, considering mass balance of incompressible flow, the continuity equation is derived as (see Appendix B for derivation):

$$-\nabla \cdot \mathbf{q}(x,y,t) - 2v_L(x,y,t) = \frac{\partial w(x,y,t)}{\partial t} \quad \text{.....(2.22)}$$

where $\nabla\cdot$ is divergence operator and v_L is the leak-off velocity, which can be computed using Darcy's Law.

Eliminating fluid flux by substituting it into Eq. 2.22 from Eq. 2.21, the fracture flow equation in terms of fluid pressure is given as:

$$\nabla.\left[\frac{w^3}{12\mu}\nabla p(x,y,0,t)\right] - 2v_L(x,y,t) = \frac{\partial w(x,y,t)}{\partial t} \quad \text{.....(2.23)}$$

The leak-off velocity in Eq. 2.23 is computed using Darcy's law assuming fracture fluid leaks into permeable formation due to the pressure differential at the fracture-matrix interface.

$$v_L(x,y,t) = -\frac{k}{\mu}\left.\frac{\partial p(x,y,z,t)}{\partial n}\right|_{z=0} \quad \text{.....(2.24)}$$

where k is the formation rock permeability and n is the outward normal of the fracture surface.

To solve for unknown fluid pressure in Eq. 2.23, either flow or pressure boundary condition is required. The choice of respective boundary conditions depends upon the

known field variables in the problem. The boundary conditions considered for the problems solved in this dissertation are presented next.

2.2.1.1 Boundary Conditions for Injection/Extraction Problems

In problems of fluid injection/extraction presented in this dissertation, constant flow rate and constant pressure are prescribed at injection and extraction wells respectively, for example:

$$Q(x_i, y_i, t) = Q_i; \quad p(x_e, y_e, t) = P_e \qquad \text{.....(2.25)}$$

where units of Q_i and P_e are volumetric rate and pressure, respectively.

Importantly, prescribing pressure while solving Neumann-type equation (Eq. 2.23) enables us to find a unique pressure.

2.2.1.2 Boundary Conditions for Hydraulic Fracture Simulation

In hydraulic fracturing treatment, pump rate at the wellbore is known and is used to prescribe the boundary condition required in the hydraulic fracture simulation model. In addition to the pumping rate, a zero-flux boundary is imposed at the fracture font (this is done implicitly when using the FEM without prescribing a BC at the front). However, for the solution (fluid pressure) to be unique (for a given fracture geometry), global mass balance is utilized. For example, the boundary conditions for Eq. 2.23 can be written as follows, (i) the fluid is pumped into the fracture through a section ∂A_p, so that:

$$-\frac{w^3}{12\mu}\left(\frac{\partial p}{\partial n}\right)=Q \text{ ……...……...(2.26)}$$

for that section, and (ii) the flux at crack front ∂A_f , is zero:

$$-\frac{w^3}{12\mu}\left(\frac{\partial p}{\partial n}\right)=0 \text{ ……..…….(2.27)}$$

Note that ∂A_p and ∂A_f are the sections of fracture initiation (perforation of wellbore) and fracture front; Q is the pumping rate per unit length of the section ∂A_p, and $\vec{n}$ is the outward normal vector of the fracture surface.

For the fracture surface, A, created at time t with pumping rate of Q through ∂A_p, the global mass balance is written as, e.g., in (Yew 1997) .

$$-\int_A 2v_l dxdy-\int_A \frac{\partial w}{\partial t}dxdy+\int_{\partial A_p} Qds=0 \text{ ……..…….(2.28)}$$

As will be shown later, the last expression is used in the last row of the stiffness matrix for the fluid pressure.

2.2.2 Heat Transport in the Fracture

Heat transfer in the fracture/fracture zone occurs mainly via advection due to fluid motion and conduction of heat through the fracture walls. Heat transport equation in the fracture can be written as (see Appendix C for derivation):

$$\rho_F c_F \mathbf{q}(x,y).\nabla T\left(x,y,0,t\right)+q_H\left(x,y,0,t\right)=0 \text{ …….(2.29)}$$

where T is the temperature, ρ_F is the fluid density, c_F is the specific heat of the fluid and q_H is the heat source intensity, which represents the heat conduction rate between the reservoir matrix and the fracture. q_H is computed using well-known Fourier's law as:

$$q_H(x, y, 0, t) = -2K_R \left.\frac{\partial T(x, y, z, t)}{\partial z}\right|_{z=0} \quad \text{.....(2.30)}$$

where K_R is the rock thermal conductivity.

2.2.3 Solute Transport in the Fracture and Rock Matrix

Mineral "solubility" under large thermal gradient between the fracture and reservoir matrix determines the amount of solutes that will be carried within the fracture. Although in geothermal injection/extraction systems, mineral dissolution and precipitation process is complex involving multi-components, considering reactivity of silica using a single-component reactive-transport model is adequate under many conditions of interest (Tang et al. 1981; Steefel and Lichtner 1998; Wangen and Munz 2004; Kumar and Ghassemi 2005). In this formulation, advection, first order reaction and diffusion of silica in the reservoir matrix are considered as the principal transport mechanisms as in (Ghassemi and Kumar 2007; Rawal and Ghassemi 2010b, 2010c). Often reactive modeling of minerals is accomplished using the local equilibrium approach without considering mineral reaction kinetics. However, a complete description of quartz dissolution and precipitation kinetics is impossible without accurate values for quartz solubility (Rimstidt and Barnes 1980). This is because as it equilibrates

at a slower rate than other minerals and hence, consideration of kinetics becomes inevitable in modeling quartz precipitation/dissolution. The quartz-water system governed by Eq. 2.31 is a simple surface reaction to form silicic acid monomer otherwise called as dissolved silica:

$$2H_2O + SiO_2 \Leftrightarrow H_4SiO_4 \quad \text{.....(2.31)}$$

Changes in pressure, in the range occurring in geothermal systems, have much lesser effect on changes in the state of mineral saturation than temperature changes. This is exemplified for quartz (Arnórsson and Gudmundsson 2003), the solubility of which has been well established experimentally over a wide range of temperature and pressure (Manning 1994; Arnórsson and Gudmundsson 2003). The equilibrium solubility of silica and especially quartz is low (amorphous silica 100-140 mg/l, quartz 6-14 mg/l at earth surface temperature) as described by Yariv and Cross (1979). As a result, the impact of pressure on solubility is neglected in this work. Using the above approach, we developed a model to quantify the evolution of fracture aperture during the dissolution/precipitation of quartz in the reservoir under laminar flow conditions. The geothermal fluid is injected either supersaturated or undersaturated with respect to the equilibrium state of quartz, into initially smooth-walled fractures.

Assuming the fluid and rock characteristics (e.g., diffusivity coefficients, porosity) as constant, the single-component solute transport system considering temperature-dependent both reaction rate and equilibrium concentration can be expressed in a planar fracture as (Rawal and Ghassemi 2010b, 2010c); (see Appendix D for derivation):

$$\mathbf{q}(x,y).\nabla c\left(x,y,0,t\right) + 2K_f c\left(x,y,0,t\right) + q_S(x,y,0,t) = 2K_f c_{eq} \quad \text{.....(2.32)}$$

where c and c_{eq} are total and equilibrium mineral concentration, respectively. K_f is intrinsic reaction-rate constant (here assumed temperature-dependent only). Similarly, q_S is the solute source intensity and can be computed using Fick's Law as:

$$q_S(x,y,0,t) = -2\phi c^S \left.\frac{\partial c(x,y,z,t)}{\partial z}\right|_{z=0} \quad \text{.....(2.33)}$$

Here, c^S is effective solute diffusion coefficient and ϕ is porosity of the reservoir matrix. With the assumption of negligible mineral reaction in the reservoir matrix, solute transport in the reservoir matrix is diffusion-dominated and governed as:

$$\frac{\partial c(x,y,z,t)}{\partial t} = c^S \nabla^2 c(x,y,z,t) \text{.....(2.34)}$$

Eqs. 2.32 through 2.34 are subjected to the initial and boundary conditions and are summarized:

$$c(x,y,z,0) = c_0; c(x_i,y_i,0,t) = c_i \text{.....(2.35)}$$

where c_0 is the initial solute concentration (here assumed as equilibrium state) and c_i is the injecting fluid concentration.

2.2.3.1 Fracture Aperture Change Due to Mineral Dissolution and Precipitation

The change in fracture aperture due to mineral dissolution and precipitation is computed using mass balance of mineral that is lost or gained at the fracture surface (Robinson and Pendergrass 1989).

$$w(x,y,0,t) = w_0 - \frac{2\times10^{-6} f_Q \rho_F K_f \Delta t}{\rho_Q}\left(c - c_{eq}\right) \quad \text{……...……...(2.36)}$$

In which w_0 is the initial average fracture aperture. Similarly, the distribution of mineral concentration, temperature dependent intrinsic reaction rate and equilibrium concentration are considered after solute transport computation. Furthermore, the temperature dependent expressions for reaction rate constant and equilibrium concentration are given as (Robinson 1982; Robinson and Pendergrass 1989):

$$K_f(T) = 10^{0.433-4090/T}$$
$$c_{eq}(T) = 6\times10^4 \times 10^{1.881-2.028\times10^{-3}T-1560/T} \quad \text{……..(2.37)}$$

2.3 Concept of Rock Joints

Rock joints are often known as fractures in rock mechanics literatures; both fracture and joint define two contacting rough surfaces with voids that are completely connected. The rough fracture under stress deforms with change in applied stresses. There are three types of deformation (e.g., normal deformation, shear deformation and dilation). The deformation causes the fracture opening or closure. The constitutive models of stress-displacement relationship of natural or artificially created fractures have been developed from the laboratory experiments (Barton 1976; Goodman 1976; Bandis et al. 1981; Bandis et al. 1983; Barton 1986; Huang et al. 2002).

2.3.1 Normal Deformation

The normal deformation of the fracture is defined by the relationship between the effective stresses across the rough surface and fracture closure. Moreover, the rough surfaces of fracture are weaker and are more deformable than intact rock and normal deformation of the two rough surfaces subjected to change in normal stresses or fluid pressure in the void space will have impact on fracture aperture and fracture permeability.

Goodman (1976) measured the fracture closure as a function of normal stress on artificially induced tensile fractures in rock cores. He measured the axial displacement of an intact rock core under axial stress and axial displacement of the rock core of the same size and an artificially induced tensile fracture perpendicular to the axis under the same axial stress. The difference of the two displacements is the fracture closure. Fracture closure measurements were made for both mated fractures, for which the two surfaces of the fracture were placed the same relative positions that they occupied before fracturing core, and non-mated fractures, for which the two surfaces of the fracture were rotated from their original positions relative to one another. The stress-closure curves (normal stress vs. fracture closure) are non-linear **(Fig. 2.1).**

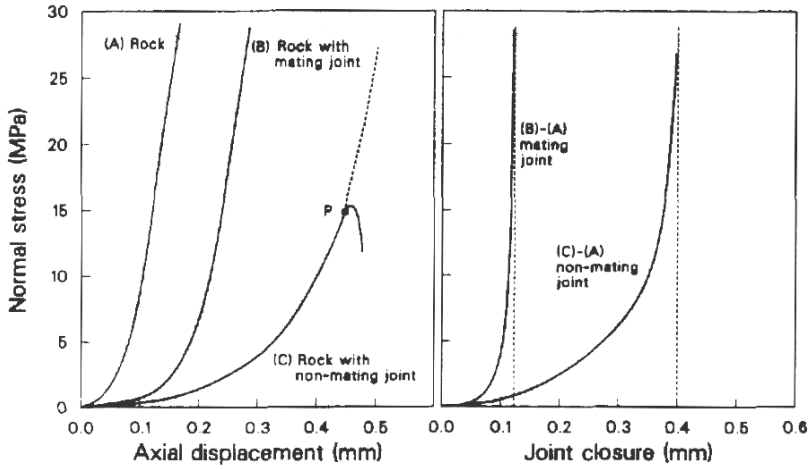

Fig. 2.1 Measurements of the closure under normal stress of an artificially-induced tensile fracture in a rock core (Goodman 1976).

Goodman (1976) described the joint closure to the normal stress using an empirical relationship:

$$\sigma_n = \sigma_i \left[1 + c_1 \left(\frac{\Delta a}{a_m - \Delta a} \right)^{c_2} \right] \text{.....(2.38)}$$

where c_1 and c_2 are the empirical parameters, Δa are the joint closure under a given σ_n; a_m is the maximum possible joint closure and σ_i is the initial stress.

Bandis et al.(1983) measured closure curves for a joint under normal stress for a variety of natural and unfilled joint with different degrees of weathering and roughness in slate, dolerite, limestone, siltstone and sandstone **(Figs. 2.2a and 2.2b).** Under the same condition, fracture closures in weathered fractures (Fig. 2.2b) were much greater than those in fresh fractures (Fig. 2.2a). With the increase of normal stress (σ_n), the

stress-closure curves became gradually steeper and developed into virtually straight lines where the fractures have reached their fully closed state. There was permanent deformation observed during the loading–unloading cycle so the deformation characteristics of fractures also depend on the stress history of the fractures.

Similar to Goodman (1976), Bandis et al. (1983) suggested the joint closure function as:

$$\sigma_n = \frac{K_{ni}\Delta a}{1-\Delta a / a_m} \qquad \text{.....(2.39)}$$

where K_{ni} is the normal stiffness at low confining stress. Eq. 2.38 by Goodman (1976) reduces to Eq. 2.39 when $c_1 = 1, c_2 = 1$ and $\sigma_n \gg \sigma_i$ .The normal stiffness of the fracture is given as:

$$K_n = \frac{\partial \sigma_n}{\partial \Delta a} = \frac{K_{ni}}{\left(1-\Delta a / a_m\right)^2} \qquad \text{.....(2.40)}$$

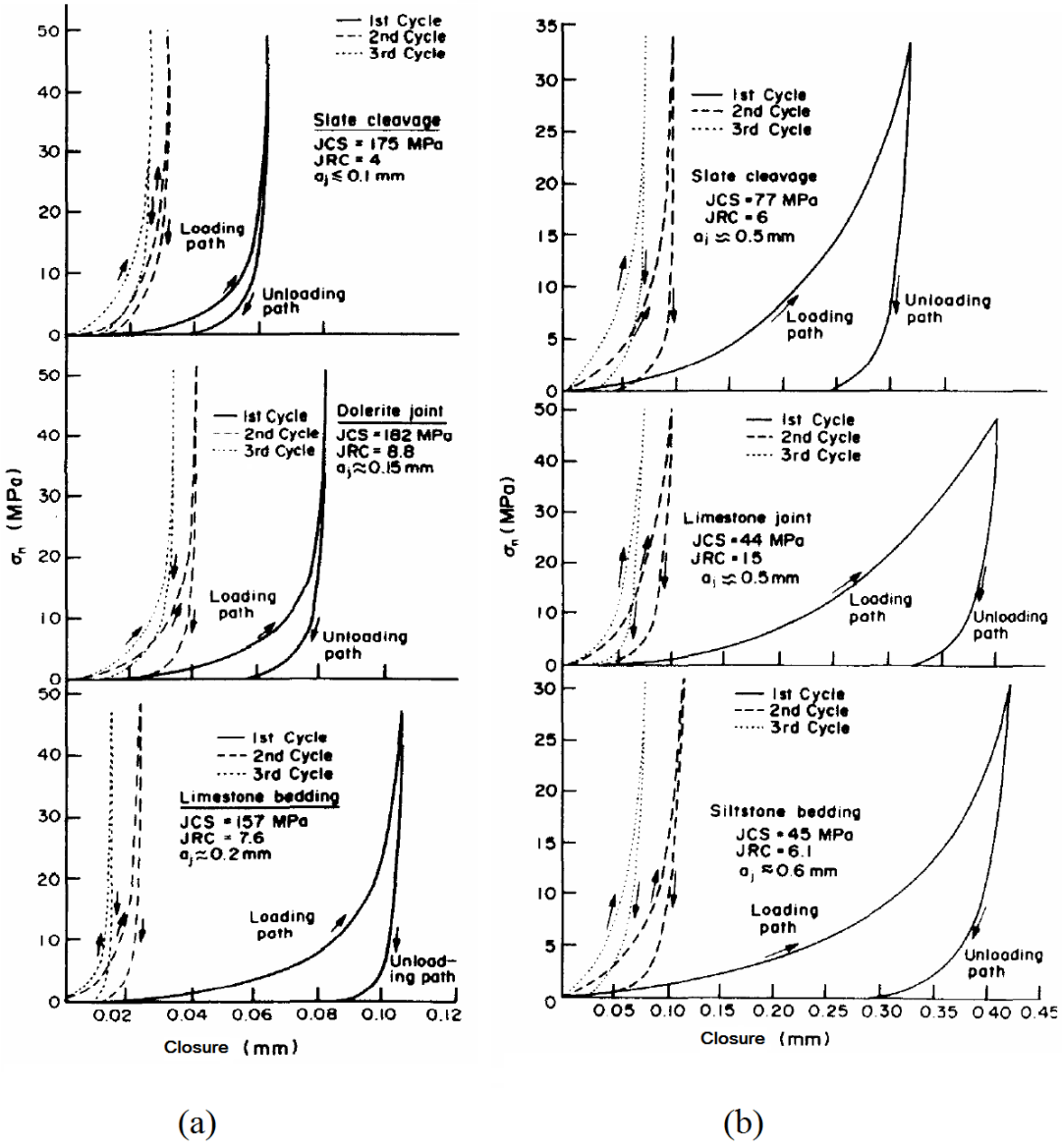

Fig. 2.2 Normal stress vs. closure curves for a range of (a) fresh (b) weathered joints in different rock types, under repeated loading cycles (Bandis et al. 1983).

2.3.2 Shear Deformation

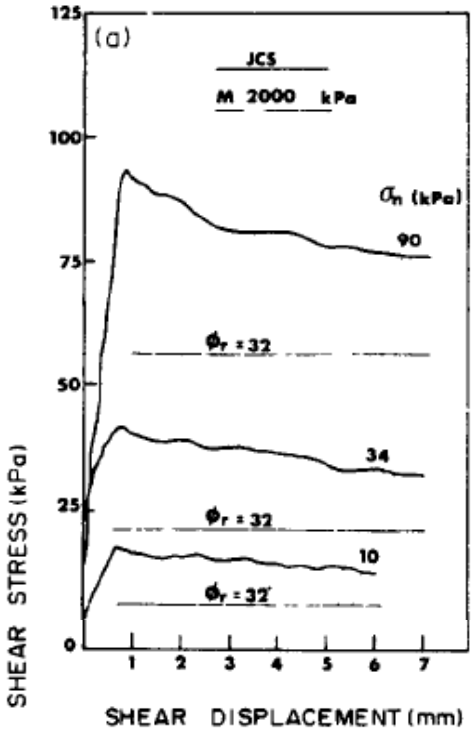

Fig. 2.3 Shear stress-shear displacement for joints with different normal stress (Barton et al. 1985).

The relative deformation parallel to the nominal fracture plane caused due to the shear traction on the rough fracture surface is known as shear deformation. Similarly, the tangential traction that causes the fracture aperture to increase is referred as dilation. Therefore, shear deformation is caused by both normal and shear displacement. The shear stiffness can be computed using the linear section until the peak stress from stress-shear displacement curve (e.g., Fig. 2.3) as:

$$K_s = \frac{\tau_{peak}}{\Delta a_s} \quad \text{.....(2.41)}$$

where τ_{peak} and Δa_s are the peak shear stress and shear displacement, respectively, at peak shear stress.

2.3.3 Joint Element

In this section, the procedures of modeling joints are described. In problems of rock mechanics, the discontinuities present in the rock mass such as joints, faults, bedding planes are described using joint models, for example, linear elastic joints, Mohr-Coulomb joints or non-linear joints. The joint model delineates the relationship between stress increment and displacement discontinuity. In this dissertation, we use constant joint normal and shear stiffness.

The "total stresses" at any point in the rock can be expressed as the sum of the "initial stresses" and stress change at that point, which are called the "induced stress" (Crouch and Starfield 1983).

$$\sigma_{ij} = \left(\sigma_{ij}\right)_0 + \sigma_{ij}^{'} \quad \text{.....(2.42)}$$

Similarly, the total displacements are expressed as:

$$u_i = \left(u_i\right)_0 + u_i^{'} \quad \text{.....(2.43)}$$

where $\left(\sigma_{ij}\right)_0$, $\sigma_{ij}^{'}$ and σ_{ij} are the initial, induced and total stresses, respectively. $\left(u_i\right)_0$, $u_i^{'}$ and u_i are the initial, induced and total displacements, respectively.

2.3.3.1 Elastic Joint Elements

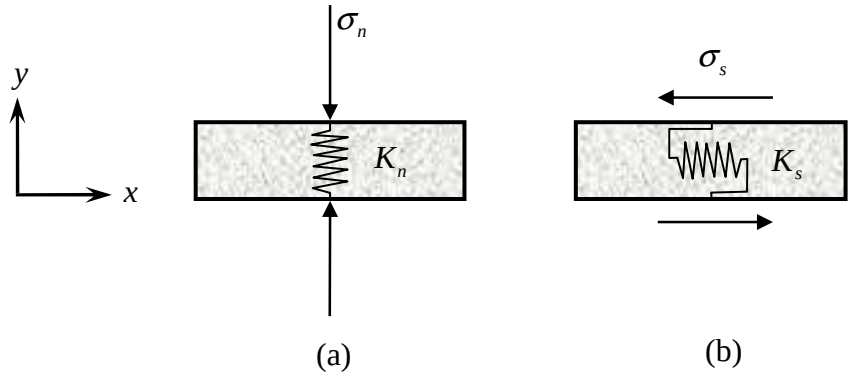

Fig. 2.4 Elastic joint element representation (a) normal stiffness (b) shear stiffness.

Considering that the joint-filling or joint surface is linearly elastic with Young's modulus and shear modulus of the rock mass and that the initial deformations to be zero, the induced normal and shear stresses are given as:

$$\begin{bmatrix} \sigma_n^{'} \\ \sigma_s^{'} \end{bmatrix} = -\begin{bmatrix} K_n & 0 \\ 0 & K_s \end{bmatrix} \begin{Bmatrix} D_n^{'} \\ D_s^{'} \end{Bmatrix} \quad \text{.....(2.44)}$$

where $\sigma_n^{'}$ and $\sigma_s^{'}$ are the induced normal and shear stresses and $D_n^{'}$ and $D_s^{'}$ are the components of induced normal and shear DD. Similarly, K_n and K_s are the stiffness of idealized springs for joint filling material or fracture surface.

2.3.3.2 Mohr-Coulomb Criterion for Joint Elements

The normal and shear stresses across the joint are constrained by Mohr-Coulomb condition (see **Fig. 2.5**), for example:

$$\left|\sigma_s^{'}\right| \le c_j + \left(-\sigma_n\right)\tan\phi \qquad \text{.....(2.45)}$$

where c_j and ϕ are the cohesion and angle of friction of joint material.

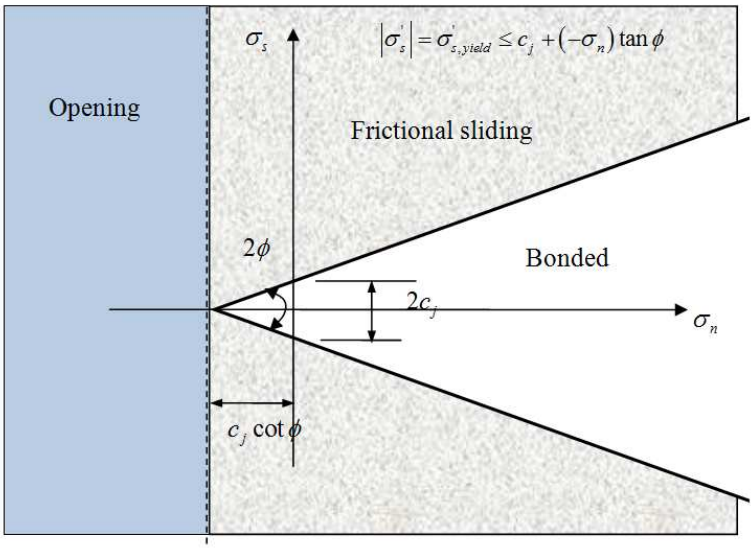

Fig. 2.5 Mohr-Coulomb element under different stress conditions.

An element in joint model that subjected to the constrain Eq. 2.45, called Mohr-Coulomb element. It behaves exactly as an ordinary joint element, except that the total shear stresses cannot exceed the value in right hand side of Eq. 2.45. Satisfying this

condition requires that the joint can only undergo certain amount of inelastic deformation, or permanent slip (Crouch and Starfield 1983).

2.3.3.3 Joint Separation Mode

A joint can be assessed whether or not it is opened using the Mohr-Coulomb condition, Eq. 2.45. This criterion is called joint separation or tensile failure. For example, according to Mohr-Coulomb condition Eq. 2.45, tensile strength of the joint is given as:

$$T_0 = c_j \operatorname{cotan} \phi \quad \text{.....(2.46)}$$

Therefore, when the tensile stress on the joint is greater than the tensile strength (T_0), the joint is opened.

2.4 Rock Failure Criterion

The joint deformation and failure is a function of effective principal stress acting normal to the joint. The Coulomb failure criterion in effective principal stress form is (Jaeger et al. 2007):

$$\sigma'_1 = C_0 + q\sigma'_3 \quad \text{.....(2.47)}$$

where

$$C_0 = 2c_0\left[\left(\mu_i^2+1\right)^{1/2}+\mu_i\right]$$
$$q = \left[\left(\mu_i^2+1\right)^{1/2}+\mu_i\right]^2 \quad \text{.....(2.48)}$$

and μ is the friction coefficient.

2.5 Fracture Propagation

The characteristics of fracture propagation and/or stability of propagation are subject of fracture mechanics and have been described by fundamental works of (Griffith 1921; Irwin 1957; Barenblatt 1962). Griffith's theory deals with the energy dissipation required in an increment of fracture extension and known as energy release rate. It describes the energy balance which leads to critical condition for fracture propagation.

In general, linear elastic fracture mechanics (LEFM) describes how much stress (energy) is required to propagate fracture, assuming brittle fracture and that the energy stored as stress in the material is transmitted directly to fracturing the material and no energy is lost to non-elastic effects (Martin and Valkó 2007). Furthermore, LEFM relates the rock strength with the stress intensity factor K, which is the measure of magnitude of stresses at the fracture tip (Knott 1973).

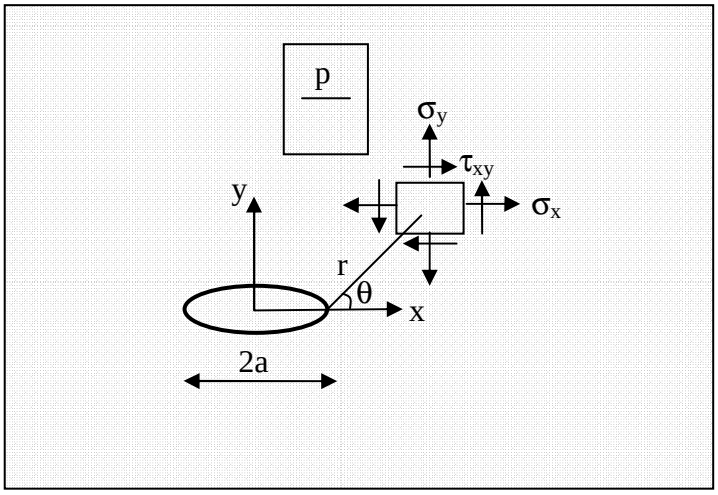

Fig. 2.6 Stress near the crack tip: p is the internal pressure and a is fracture half length, after (Ghassemi 1996).

For example, the stress field in the vicinity of the tip of a two-dimensional crack is given as (see **Fig. 2.6**):

$$\sigma_y = \frac{K}{\sqrt{2\pi(x-a)}} \quad \text{.....(2.49)}$$

Stress-intensity factor (K) depends on the geometry and loading. For limiting value it can be written as:

$$K = \sigma\sqrt{2\pi a}; \sigma = \lim_{x \to a} \sigma_y \quad \text{.....(2.50)}$$

Fracture propagates when the value of stress intensity reaches a critical value characteristic of rock. This parameter.is known as the fracture toughness, K_c, which is the material property and can be determined experimentally (Roegiers and Zhao 1991). The general methods to define fracture propagations are based on conventional energy-release rate approach or stress intensity factor (SIF) approach and maximum tensile stress approach.

Three fundamental modes of fracture propagation are Mode-I, Mode-II, and Mode-III **(Fig. 2.7).** Mode-I is tensile or opening mode, in which crack surfaces move apart in a direction perpendicular to the surfaces; Mode-II is in-plane shear or sliding mode, in which the crack surfaces slide over one another in a direction perpendicular to the leading edge of the crack and Mode-III is antiplane shear or tearing mode, in which the crack surfaces move relative to one another in a direction parallel to the leading edge of the crack.

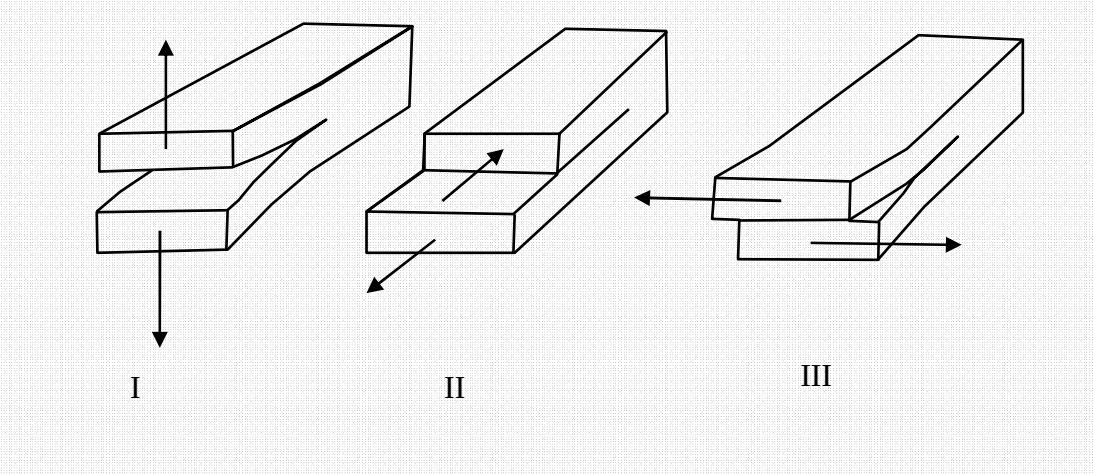

Fig. 2.7 Sketch of three fundamental modes of fracture propagation.

In modeling hydraulic fracture, it is assumed that fracture propagation occurs when the stress intensity at the tip equals the fracture toughness: $K_I = K_{IC}$; in which K_I and K_{IC} are Mode-I stress intensity factor and fracture toughness, respectively. This propagation criterion is widely used in LEFM and it is a common assumption in models of hydraulic fracture propagation in rock (Rice 1968; Geertsma and Klerk 1969; Clifton and Abou-Sayed 1979; Gidley et al. 1989; Valkó and Economides 1995). Furthermore, propagation of hydraulic fracture is assumed to be in quasi-static and mobile equilibrium. However, extensive works on topic has been published and it has found that other effects such as (fluid lag, crack tip plasticity and fluid rheology) might influence the regime of fracture propagation (Yew and Liu 1993; Ghassemi 1996; Detournay 2004; Martin and Valkó 2007).

3. NUMERICAL FORMULATION

In order to solve governing equations representing different coupled poro-thermo-mechanical systems described in previous chapter, numerical modeling is required. Traditionally, in reservoir simulation, Finite Difference Method (FDM) is the most commonly used technique because of its comparatively simplicity and ease in implementation. Theoretically, FDM is straightforward. Early works in application of theory of finite difference to petroleum reservoir engineering (Peaceman 1977; Aziz and Settari 1979) have been motivations in evolution of reservoir simulation works.

An early application of Finite Element Method (FEM) in petroleum reservoir engineering is the classic paper by Price (1968). Since then, other researchers have used FEM for different purposes– waterflooding in petroleum reservoirs (Douglas et al. 1969; Settari et al. 1977; Douglas 1997); hydraulic fracture simulation (Clifton and Abou-Sayed 1981; Advani and Lee 1982; Boone and Detournay 1990; Boone and Ingraffea 1990) and coupled multi-physical problems (Zienkiewicz 1976; Zienkiewicz 1984; Zienkiewicz and Taylor 1991).

Boundary Element Method (BEM) has been applied extensively to varieties of engineering problems, for example, reservoir flow problems (Gringarten et al. 1973; Liggett and Liu 1979; Numbere and Tiab 1988; Kikani and Horne 1989; Kikani and Horne 1992, 1993; Archer and Horne 1998; Jongkittinarukorn and Tiab 1998; Samardzioska 2009) as well as geomechanical aspects of petroleum development such as hydraulic fracturing (Detournay et al. 1986; Vandamme et al. 1988; Vandamme et al.

1989; Ghassemi 1996; Pecher 1999; Yamamoto et al. 2004), wellbore stress analysis and subsidence (Vandamme 1986; Cheng and Predeleanu 1987; Vandamme et al. 1988; Detournay and Cheng 1991; Ghassemi and Diek 2003; Suzuki and Morita 2004). Significant developments of BEM have resulted from interest by civil, mining and petroleum applications (Banerjee and Butterfield 1981; Crouch and Starfield 1983; Cheng and Detournay 1988; Vandamme and Curran 1989; Detournay and Cheng 1993; Cheng et al. 2001; Ghassemi et al. 2003, 2007; Zhou et al. 2009). Particularly, this is because of BEM's flexibility in handling infinite domain, complex geometries and boundary conditions.

Therefore, in this dissertation, both the FEM and BEM approaches are used to solve the problem of interest. The BEM is considered to take care of reservoir infinite domain (thus, it removes the need of full domain discretization), while the FEM used to treat the linear and non-linear processes within the fracture and/or the reservoir. The coupling between these two methods is achieved by using direct substitution or iterative procedure. These developments are described next.

3.1 Integral Equation Method for Treating the Infinite Matrix Around Fractures

Boundary Element Method is a powerful numerical tool of solving linear partial differential equations which are formulated in terms of integral equations (Brebbia et al. 1984; Brebbia and Dominguez 1992).

BEM is derived through the discretization of integral equations which are considered mathematically equivalent to the governing partial differential equations. The

analytical solutions of the integral equations correspond to some form of singular impulse at a point in an infinite region, are called “fundamental solutions”. For example, in solid mechanics, the impulse can represent a point force applied within an elastic solid or in problems of thermo-poroelasticity; impulse could be of a point fluid source, a point heat source or a displacement discontinuity. The fundamental solutions are also known as “singular solutions” because of their singularity at the point of impulse; except that point, they are well behaved everywhere in the region. BEM unlike other numerical methods (FEM or FDM−which approximate values throughout the space defined by a partial differential equation) uses the prescribed boundary conditions to fit boundary values into the integral equation. Once this process is completed, the integral equation is used to find the solution at any point in the interior domain.

Thus, the technique of BEM formulation is first, to specify some conditions in the governing partial differential equations on the boundary of region of interest, Ω, enclosed within a boundary, Γ and then to solve like boundary value problem. For example, as depicted in **Fig. 3.1,** BEM makes approximations only on the boundary Γ by dividing it into M elements, therefore, it removes the need of discretization of whole domain, Ω (Crouch and Starfield 1983). At any element, by expressing the combined effect of all N singular impulses (of fluid source, heat source, solute sources or displacement discontinuity) in terms of the “strengths” of the impulses, a system of N linear algebraic equations can be formed (unknowns are strengths of impulses). Once this system of equation is solved, the solution at any point in Ω can be completed.

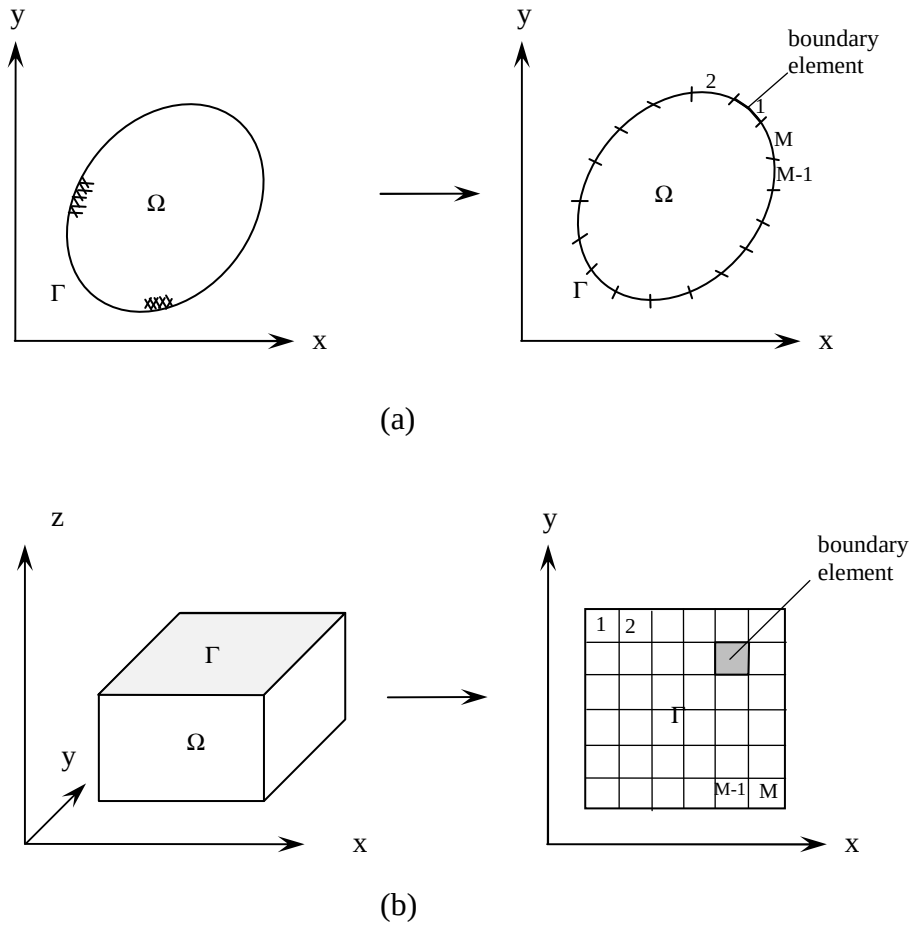

Fig. 3.1 BEM discretization (a) in two dimensions and (b) in three dimensions. Ω and Γ represent problem domain and its boundary, respectively.

The main advantage of BEM is the significant reduction in spatial discretization since it uses boundary-only discretization. Therefore, it simplifies in modeling by generating a smaller number of equations while solving a boundary value problem compared to other numerical methods. However, the global stiffness matrix is fully

populated as each singular impulse plays a part in every equation (Crouch and Starfield 1983).

There are two types of BEM, “direct” and “indirect”. The direct method represents the integral equations based on the generalized Green’s theorem, which sometimes are expressed in the form of an energy reciprocity theorem (Cheng and Detournay 1998) and gives displacements at internal and boundary points in terms of boundary tractions and displacements. However, in indirect boundary element method, the displacements are written in functions of variables which are not explicitly the boundary displacements and tractions (Brebbia and Dominguez 1992; Ghassemi 1996) but can be based on distributions of influence functions such as (fluid, heat or solute source etc. with “fictitious densities”). Moreover, the indirect boundary element method consists of two different procedures viz. the fictitious stress method, suitable in problems when two surfaces of boundary do not coincide in space (e.g., in underground opening) and the displacement discontinuity method, suitable in problems when two surfaces of boundary do coincide in space (e.g., involving fractures), as shown in **Fig. 3.2.**

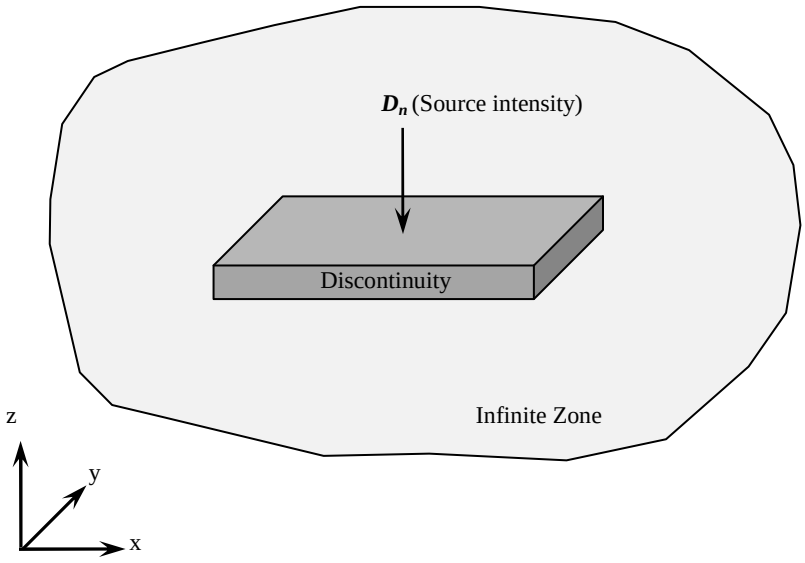

Fig. 3.2 Displacement discontinuity formulation in 3D BEM.

In the displacement discontinuity formulation, the fundamental solutions for source densities are required to integrated over an element (after spatial discretization) to form global “stiffness matrix”. The fundamental solutions for source densities (e.g., of fluid sources and displacement discontinuity) used in this dissertation can be found in (Carvalho 1990; Cheng and Detournay 1998), in which the fundamental solutions are derived using an unified approach of various singular integral equations for solutions of linear, quasi-static and isotropic poroelasticity. The fundamental solutions for the solute diffusion are constructed by analogy with pore pressure source solution (Rawal and Ghassemi 2010a, 2010b, 2010c) whereas the fundamental solutions of integral equations for transient heat flow are adopted similar to Zhou et al.(2009). The fundamental solutions used in this dissertation are summarized in Appendix E.

3.1.1 3D Boundary Integral Equations for Thermo-Chemo-Poroelasticity

With fundamental solutions, the stress, pore pressure, temperature and concentration fields on the boundary are approximated at any time, by performing spatial integration over all boundary elements and temporal integration in time. Therefore, determination of field variables needs history of the strengths of the displacement discontinuity (DD), fluid source, heat source and solute source. Moreover, computation of their history requires solution of the singular integral equations. These integral equations can be found using the principle of superposition in a heuristic approach or in a rigorous fashion based on the reciprocal theorem (Cheng and Detournay 1998; Ghassemi and Zhang 2004).

$$\begin{aligned}\sigma_{ij}(\mathbf{x},t) &= \int_0^t\int_A \sigma_{ijkn}^{iD}(\mathbf{x}-\mathbf{x}',t-t')\,D_{kn}(\mathbf{x}',t')\,dA(\mathbf{x}')dt' \\ &+ \int_0^t\int_A \sigma_{ij}^{iF}(\mathbf{x}-\mathbf{x}',t-t')\,D_F(\mathbf{x}',t')\,dA(\mathbf{x}')dt' \\ &+ \int_0^t\int_A \sigma_{ij}^{iH}(\mathbf{x}-\mathbf{x}',t-t')\,D_H(\mathbf{x}',t')\,dA(\mathbf{x}')dt' + \sigma_{ij0}(\mathbf{x})\end{aligned} \quad \ldots\ldots\ldots\ldots\ldots\ldots\ldots\ldots(3.1)$$

$$\begin{aligned}p(\mathbf{x},t) &= \int_0^t\int_A p_{ij}^{iD}(\mathbf{x}-\mathbf{x}',t-t')\,D_{ij}(\mathbf{x}',t')\,dA(\mathbf{x}')dt' \\ &+ \int_0^t\int_A p^{iF}(\mathbf{x}-\mathbf{x}',t-t')\,D_F(\mathbf{x}',t')\,dA(\mathbf{x}')dt' + p_0(\mathbf{x})\end{aligned} \quad \ldots\ldots\ldots\ldots\ldots\ldots\ldots\ldots(3.2)$$

$$T(\mathbf{x},t) = \int_0^t\int_A T^{iH}(\mathbf{x}-\mathbf{x}',t-t')\,D_H(\mathbf{x}',t')\,dA(\mathbf{x}')dt' + T_0(\mathbf{x}) \quad \ldots\ldots\ldots\ldots\ldots\ldots\ldots\ldots(3.3)$$

$$c(\mathbf{x},t) = \int_0^t\int_A c^{iS}(\mathbf{x}-\mathbf{x}',t-t')\,D_S(\mathbf{x}',t')\,dA(\mathbf{x}')dt' + c_0(\mathbf{x}) \quad \ldots\ldots\ldots\ldots\ldots\ldots\ldots\ldots(3.4)$$

In above equations, A boundary surface; t is time; $\mathbf{x}$ and $\mathbf{x}'$ are three-dimensional coordinate tensors and subscripts $i, j, k\,(=1-3)$ denote thee directions.

$\sigma_{ij}(\mathbf{x},t)$ is the stress component. Similarly, $p(\mathbf{x},t), T(\mathbf{x},t)$ and $c(\mathbf{x},t)$ are pore pressure, temperature and concentration, respectively, at coordinates $\mathbf{x}$ and at time t. The fundamental solution $\sigma_{ijkn}^{iD}(\mathbf{x}-\mathbf{x}', t-t')$ represents stress component $\sigma_{ij}(\mathbf{x},t)$ due to an instantaneous DD located at $\mathbf{x}'$ and taking place at time t'.

Similarly, σ_{ijkn}^{iF} , σ_{ij}^{iH} , p_{ij}^{iD} , p^{iF} , T^{iH} and c^{iS} are the instantaneous fundamental solutions of- incremental stresses, pore pressure, temperature and concentration due to unit impulse of displacement discontinuity ("iD"), fluid source intensity ("iF") , heat source intensity ("iH") and solute source intensity ("iS"). $D_{kn}(\text{or } D_{ij}), D_F$, D_H and D_S are the displacement discontinuity, fluid solute source intensity, heat source intensity and solute source intensity, respectively,. Likewise, σ_{ij0} , p_0 , T_0 and c_0 are the initial stresses, pore pressure, temperature and concentration, respectively.

3.1.1.1 Numerical Implementation of Integral Equations

To solve the boundary integral equations of transient thermo-poroelasticity and mineral diffusion, the fundamental solutions needs to be discretized in both the space and time. The spatial discretization is completed by dividing the boundary of the problem into a number of elements (like "finite elements") and replacing the integrals over the boundary by sum of integrals over these elements. In this dissertation, space integrals over the elements are completed numerically; the weakly- and hyper- singularities arising from integrating the kernel in boundary surface are treated using algorithms proposed by Guiggiani et al. (1992), in which the singular integrals are transformed into

a sum of double and one-dimensional regular integrals using series expansion and polar coordinate transformation [see, for example, Zhou et al. (2009)]. Similarly, temporal discretization is completed by dividing the time domain into a number of time increments and utilizing a time marching scheme. Following assumptions are made to implement integral equations in BEM:

1. the boundary elements are isoparametric quadrilaterals.
2. the singular impulse for (DD) is located at the midpoint, whereas single impulses for fluid source, heat source and solute source are located at the nodes of each element. The intensity of the impulses is linearly varies over each element except DD (constant element), shown in **Fig. 3.3.**
3. the time increment (Δt) is constant.

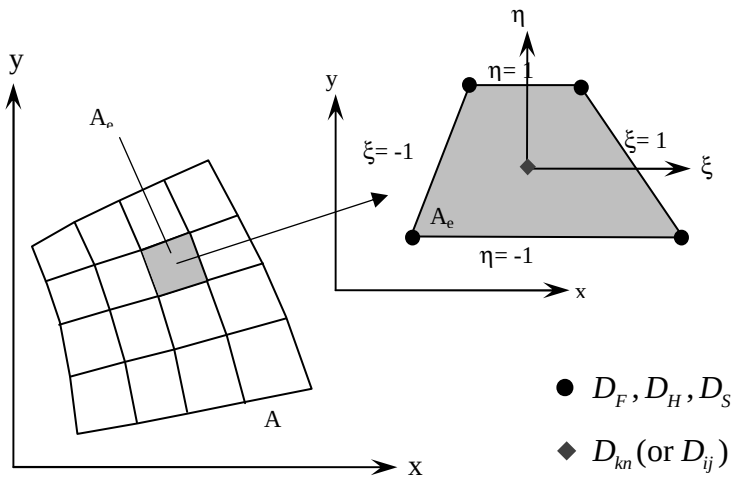

Fig. 3.3 Space discretization and variable approximation used for 3D BEM.

There are different approaches for time marching while completing temporal integration in equations (Eqs. 3.1 through 3.4). In this dissertation, a time marching procedure similar to Dargush and Banerjee (1989) is adopted, in which the problem is solved the end of a time step and solution history is saved. This allows for strengths of singular impulses to vary with time with incrementing them at each time step and including the influence of all previous increments. This technique eliminates the need for internal discretization of the spatial domain; however, disadvantage is that the coefficient matrix must be stored. The scheme is illustrated in **Fig. 3.4** (Curran and Carvalho 1987).

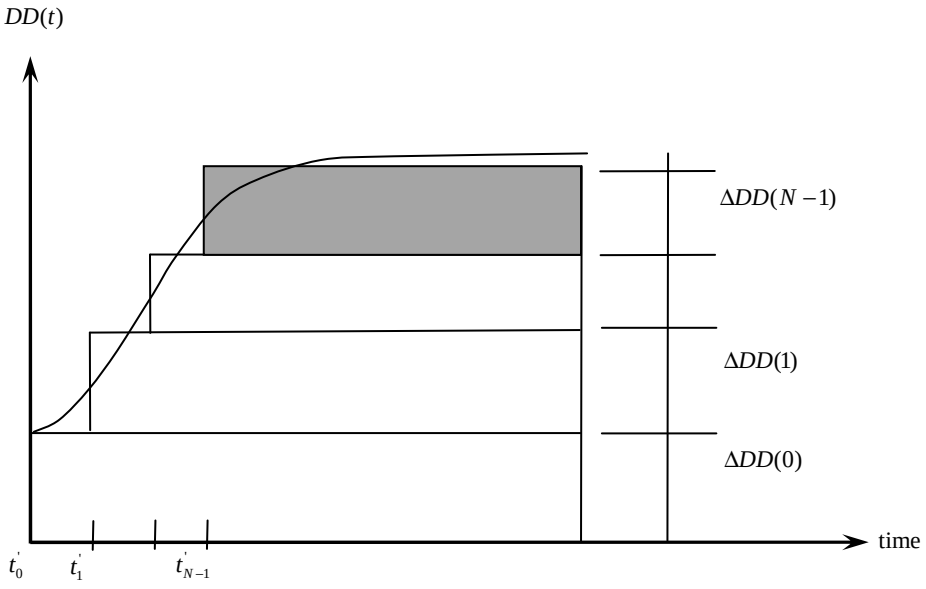

Fig. 3.4 Time marching procedure for a continuous source, after Curran and Carvalho (1987).

By implementing procedure described above with M total boundary elements and N total times steps, components of the integral equations (Eqs. 3.1 through 3.4) can be summarized as:

$$\int_0^t \int_A \sigma_{ijkn}^{iD}\left(\mathbf{x}-\mathbf{x}',t-t'\right) D_{kn}\left(\mathbf{x}',t'\right) dA(\mathbf{x}')dt'$$
$$\simeq \left[\sum_{m=1}^{M} \int_{A_e} \sigma_{ijkn}^{cD}\left(\mathbf{x}-\mathbf{x}',\Delta t\right) dA(\mathbf{x}')\right] \tilde{\mathbf{D}}_{kn}\left(N\Delta t\right) \qquad \text{.....(3.5)}$$
$$+\sum_{l=1}^{N-1}\left[\sum_{m=1}^{M} \int_{A_e} \sigma_{ijkn(N-l+1)}^{cD}\left(\mathbf{x}-\mathbf{x}',\Delta t\right) dA(\mathbf{x}')\right] \tilde{\mathbf{D}}_{kn}\left(l\Delta t\right)$$

$$\int_0^t \int_A \sigma_{ij}^{iF}\left(\mathbf{x}-\mathbf{x}',t-t'\right) D_{F}\left(\mathbf{x}',t'\right) dA(\mathbf{x}')dt'$$
$$\simeq \left[\sum_{m=1}^{M} \int_{A_e} \mathbf{N}^{(m)}\sigma_{ij}^{cF}\left(\mathbf{x}-\mathbf{x}',\Delta t\right) dA(\mathbf{x}')\right] \tilde{\mathbf{D}}_{F}\left(N\Delta t\right)+ \qquad \text{.....(3.6)}$$
$$\sum_{l=1}^{N-1}\left[\sum_{m=1}^{M} \int_{A_e} \mathbf{N}^{(m)}\sigma_{ij(N-l+1)}^{cF}\left(\mathbf{x}-\mathbf{x}',\Delta t\right) dA(\mathbf{x}')\right] \tilde{\mathbf{D}}_{F}\left(l\Delta t\right)$$

$$\int_0^t \int_A \sigma_{ij}^{ih}\left(\mathbf{x}-\mathbf{x}',t-t'\right) D_{H}\left(\mathbf{x}',t'\right) dA(\mathbf{x}')dt'$$
$$\simeq \left[\sum_{m=1}^{M} \int_{A_e} \mathbf{N}^{(m)}\sigma_{ij}^{cH}\left(\mathbf{x}-\mathbf{x}',\Delta t\right) dA(\mathbf{x}')\right] \tilde{\mathbf{D}}_{H}\left(N\Delta t\right) \qquad \text{.....(3.7)}$$
$$+\sum_{l=1}^{N-1}\left[\sum_{m=1}^{M} \int_{A_e} \mathbf{N}^{(m)}\sigma_{ij(N-l+1)}^{cH}\left(\mathbf{x}-\mathbf{x}',\Delta t\right) dA(\mathbf{x}')\right] \tilde{\mathbf{D}}_{H}\left(l\Delta t\right)$$

$$\int_0^t \int_A p_{ij}^{iD}\left(\mathbf{x}-\mathbf{x}',t-t'\right) D_{ij}\left(\mathbf{x}',t'\right) dA(\mathbf{x}')dt'$$
$$\simeq \left[\sum_{m=1}^{M} \int_{A_e} p_{ij}^{cD}\left(\mathbf{x}-\mathbf{x}',\Delta t\right) dA(\mathbf{x}')\right] \tilde{\mathbf{D}}_{ij}\left(N\Delta t\right) \qquad \text{.....(3.8)}$$
$$+\sum_{l=1}^{N-1}\left[\sum_{m=1}^{M} \int_{A_e} p_{ij(N-l+1)}^{cD}\left(\mathbf{x}-\mathbf{x}',\Delta t\right) dA(\mathbf{x}')\right] \tilde{\mathbf{D}}_{ij}\left(l\Delta t\right)$$

$$\int_0^t \int_A p^{iF}\left(\mathbf{x}-\mathbf{x}',t-t'\right) D_F\left(\mathbf{x}',t'\right) dA(\mathbf{x}')dt'$$
$$\simeq \left[\sum_{m=1}^{M} \int_{A_e} \mathbf{N}^{(m)} p^{cF}\left(\mathbf{x}-\mathbf{x}',\Delta t\right) dA(\mathbf{x}')\right] \tilde{\mathbf{D}}_F\left(N\Delta t\right) \quad \text{……..……(3.9)}$$
$$+\sum_{l=1}^{N-1}\left[\sum_{m=1}^{M} \int_{A_e} \mathbf{N}^{(m)} p^{cF}_{(N-l+1)}\left(\mathbf{x}-\mathbf{x}',\Delta t\right) dA(\mathbf{x}')\right] \tilde{\mathbf{D}}_F\left(l\Delta t\right)$$

$$\int_0^t \int_A T^{iH}\left(\mathbf{x}-\mathbf{x}',t-t'\right) D_H\left(\mathbf{x}',t'\right) dA(\mathbf{x}')dt'$$
$$\simeq \left[\sum_{m=1}^{M} \int_{A_e} \mathbf{N}^{(m)} T^{cH}\left(\mathbf{x}-\mathbf{x}',\Delta t\right) dA(\mathbf{x}')\right] \tilde{\mathbf{D}}_H\left(N\Delta t\right) \quad \text{……..……(3.10)}$$
$$+\sum_{l=1}^{N-1}\left[\sum_{m=1}^{M} \int_{A_e} \mathbf{N}^{(m)} T^{cH}_{(N-l+1)}\left(\mathbf{x}-\mathbf{x}',\Delta t\right) dA(\mathbf{x}')\right] \tilde{\mathbf{D}}_H\left(l\Delta t\right)$$

$$\int_0^t \int_A C^{iS}\left(\mathbf{x}-\mathbf{x}',t-t'\right) D_S\left(\mathbf{x}',t'\right) dA(\mathbf{x}')dt'$$
$$\simeq \left[\sum_{m=1}^{M} \int_{A_e} \mathbf{N}^{(m)} C^{cS}\left(\mathbf{x}-\mathbf{x}',\Delta t\right) dA(\mathbf{x}')\right] \tilde{\mathbf{D}}_S\left(N\Delta t\right) \quad \text{……..……(3.11)}$$
$$+\sum_{l=1}^{N-1}\left[\sum_{m=1}^{M} \int_{A_e} \mathbf{N}^{(m)} C^{cS}_{(N-l+1)}\left(\mathbf{x}-\mathbf{x}',\Delta t\right) dA(\mathbf{x}')\right] \tilde{\mathbf{D}}_S\left(l\Delta t\right)$$

where $D_{kn}\left(\text{or } D_{ij}\right), D_F, D_H$ and D_S are strengths continuous DD, fluid source, heat source and solute source, respectively, in time increment l . Similarly, $\tilde{\mathbf{D}}_{kn}\left(N\Delta t\right)\left(\text{or } \tilde{\mathbf{D}}_{ij}\left(N\Delta t\right)\right)$, $\tilde{\mathbf{D}}_F\left(N\Delta t\right)$, $\tilde{\mathbf{D}}_H\left(N\Delta t\right)$ and $\tilde{\mathbf{D}}_S\left(N\Delta t\right)$ are only unknown vectors and $\tilde{\mathbf{D}}_{kn}\left(l\Delta t\right)$, $\tilde{\mathbf{D}}_F\left(l\Delta t\right)$,$\tilde{\mathbf{D}}_H\left(l\Delta t\right)$ and $\tilde{\mathbf{D}}_S\left(l\Delta t\right)$ for $\left(l<N\right)$ are obtained in the previous time steps. The superscripts *"cD", "cF", "cH" and "cS"* denote the fundamental solutions due to the continuous unit DDs, fluid source intensity, heat source intensity and solute source intensity, respectively. Because of the "time translation" property of fundamental solutions–meaning only the difference between the loadings and receiving times affects the response rather than the absolute time of loading and

receiving time. The compact forms of kernels arising from discretized convolution integral of fundamental solutions in Eqs. 3.5 through 3.11 are known explicitly, e.g.,

$$\sigma_{ijkn(l)}^{cD}\left(\mathbf{x}-\mathbf{x}',\Delta t\right)=\begin{cases}\sigma_{ijkn}^{cD}\left(\mathbf{x}-\mathbf{x}',\Delta t\right) & ;\, l=1\\ \sigma_{ijkn}^{cD}\left(\mathbf{x}-\mathbf{x}',l\Delta t\right)-\sigma_{ijkn}^{cD}\left(\mathbf{x}-\mathbf{x}',\left(l-1\right)\Delta t\right); & l>1\end{cases} \quad \text{……..(3.12)}$$

Likewise, $\sigma_{ijkn(l)}^{cD}, \sigma_{ij(l)}^{cF}, \sigma_{ij(l)}^{cH}, p_{n(l)}^{cD}, p_{(l)}^{cF}, T_{(l)}^{cH}$ and $c_{(l)}^{cS}$ are expressed as in Eq. 3.12. Substituting the discretized equations (Eqs. 3.5 through 3.11) into integral equations (Eqs. 3.1 through 3.4) for (normal) stress, pore pressure, temperature and concentration, respectively, it yields:

$$\begin{aligned}\sigma_n\left(\mathbf{x},t\right)=&\left[\sum_{m=1}^{M}\int_{A_e}\sigma_{nn}^{cD}\left(\mathbf{x}-\mathbf{x}',\Delta t\right)dA(\mathbf{x}')\right]\tilde{\mathbf{D}}_n\left(N\Delta t\right)\\&+\left[\sum_{m=1}^{M}\int_{A_e}\mathbf{N}^{(m)}\sigma_n^{cF}\left(\mathbf{x}-\mathbf{x}',\Delta t\right)dA(\mathbf{x}')\right]\tilde{\mathbf{D}}_F\left(N\Delta t\right)\\&+\left[\sum_{m=1}^{M}\int_{A_e}\mathbf{N}^{(m)}\sigma_n^{cH}\left(\mathbf{x}-\mathbf{x}',\Delta t\right)dA(\mathbf{x}')\right]\tilde{\mathbf{D}}_H\left(N\Delta t\right)+\boldsymbol{\sigma}_{\mathbf{n1}}+\boldsymbol{\sigma}_{\mathbf{n0}}\end{aligned} \quad \text{……..…….....(3.13)}$$

$$\begin{aligned}p\left(\mathbf{x},t\right)=&\left[\sum_{m=1}^{M}\int_{A_e}p_n^{cD}\left(\mathbf{x}-\mathbf{x}',\Delta t\right)dA(\mathbf{x}')\right]\tilde{\mathbf{D}}_n\left(N\Delta t\right)\\&+\left[\sum_{m=1}^{M}\int_{A_e}\mathbf{N}^{(m)}p^{cF}\left(x-x',\Delta t\right)dA(x')\right]\tilde{\mathbf{D}}_F\left(N\Delta t\right)+\mathbf{p}_{\mathbf{1}}+\mathbf{p}_{\mathbf{0}}\end{aligned} \quad \text{……..(3.14)}$$

$$T\left(\mathbf{x},t\right)=\left[\sum_{m=1}^{M}\int_{A_e}\mathbf{N}^{(m)}T^{cH}\left(\mathbf{x}-\mathbf{x}',\Delta t\right)dA(\mathbf{x}')\right]\tilde{\mathbf{D}}_H\left(N\Delta t\right)+\mathbf{T}_{\mathbf{1}}+\mathbf{T}_{\mathbf{0}} \text{……...……...…..(3.15)}$$

$$c\left(\mathbf{x},t\right)=\left[\sum_{m=1}^{M}\int_{A_e}\mathbf{N}^{(m)}c^{cS}\left(\mathbf{x}-\mathbf{x}',\Delta t\right)dA(\mathbf{x}')\right]\tilde{\mathbf{D}}_S\left(N\Delta t\right)+\mathbf{c}_{\mathbf{1}}+\mathbf{c}_{\mathbf{0}} \text{…….……...……....(3.16)}$$

where $\boldsymbol{\sigma_{n1}}, \mathbf{p_1}, \mathbf{T_1}$ and $\mathbf{c_1}$ are the sum of several terms on the right hand sides of (Eqs. 3.5 through 3.11), denoting the contributions from all previous time steps and are evaluated directly.

$$\boldsymbol{\sigma_{n1}} = \begin{Bmatrix} \sigma_{n1}(x_1, y_1, 0) \\ \sigma_{n1}(x_2, y_2, 0) \\ \vdots \\ \sigma_{n1}(x_M, y_M, 0) \end{Bmatrix} \quad \text{.....(3.17)}$$

$$\boldsymbol{\sigma_{n0}} = \begin{Bmatrix} \sigma_{n0}(x_1, y_1, 0) \\ \sigma_{n0}(x_2, y_2, 0) \\ \vdots \\ \sigma_{n0}(x_M, y_M, 0) \end{Bmatrix} \quad \text{...(3.18)}$$

$$\mathbf{p_1} = \begin{Bmatrix} p_1(x_1, y_1, 0) \\ p_1(x_2, y_2, 0) \\ \vdots \\ p_1(x_{TN}, y_{TN}, 0) \end{Bmatrix} \quad \text{.....(3.19)}$$

$$\mathbf{p_0} = \begin{Bmatrix} p_0(x_1, y_1, 0) \\ p_0(x_2, y_2, 0) \\ \vdots \\ p_0(x_{TN}, y_{TN}, 0) \end{Bmatrix} \quad \text{.....(3.20)}$$

$$\mathbf{c_1} = \begin{Bmatrix} c_1(x_1, y_1, 0) \\ c_1(x_2, y_2, 0) \\ \vdots \\ c_1(x_{TN}, y_{TN}, 0) \end{Bmatrix} \quad \text{.....(3.21)}$$

$$\mathbf{c_0} = \begin{Bmatrix} c_0(x_1, y_1, 0) \\ c_0(x_2, y_2, 0) \\ \vdots \\ c_0(x_{TN}, y_{TN}, 0) \end{Bmatrix} \quad \text{.....(3.22)}$$

In Eqs. 3.19 through 3.22, TN represents the total number of nodes of boundary elements.

Eqs. 3.13 through 3.16 represent a set of linear algebraic equations and are solved by applying appropriate boundary conditions. In this numerical formulation, stresses, pore pressure, temperature and concentration are applied as the boundary conditions. For other types of boundary conditions, the procedure of numerical implementation remains the same and method described here can be adopted to study other diffusion-deformation boundary element models provided the fundamental solutions are available.

Importantly, in present formulation, the coupling between FEM and BEM becomes necessary because the “boundary conditions” needed to apply in BEM are not known explicitly rather these are solved simultaneously or iteratively from transport equations using the FEM.

3.2 Finite Element Method

As stated in Section **2**, the governing equations of transport processes in the fracture are (Eqs. 2.23, 2.29 and 2.32) for fluid flow, heat transport and solute transport respectively. In this section, we present the FEM formulation of these transport equations used to solve fluid pressure, temperature and concentration in the fracture.

In the finite element method, the space dimension is discretized into smaller regions (“subdomains”) of simple but arbitrary shape (“finite elements”) and the governing equations are approximated over these subdomains (e.g., **Fig. 3.5**) using “variational methods” (Zienkiewicz and Taylor 2000). The traditional variational methods are the Ritz, Galerkin, least-squares and collocation.

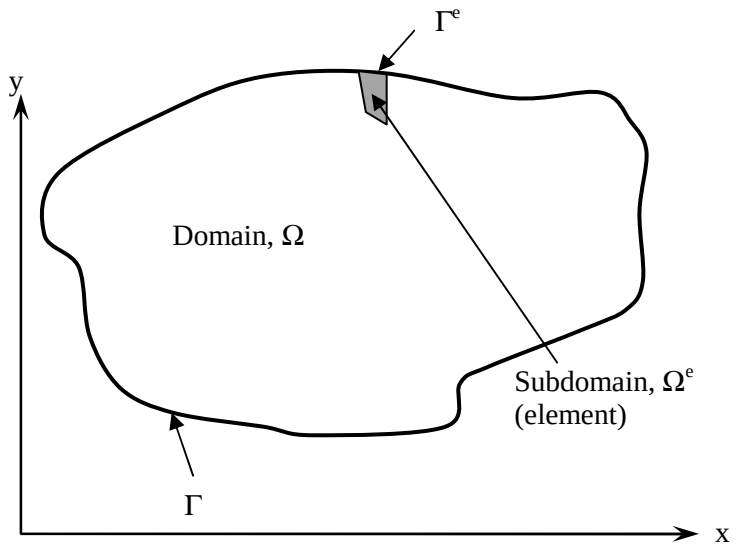

Fig. 3.5 General problem domain and its boundary in the finite element method.

By seeking approximate solutions on the sets of subdomains, it leads to easy representation of a complicated function by using simple polynomials (Reddy 2006), for example, as shown **Fig. 3.6.** In traditional variational methods the governing equation is placed into an equivalent weighted-integral form then the approximated solution over the

domain is assumed to be linear combination $\left(\sum_j c_j \phi_j\right)$ of known functions $\left(\phi_j\right)$ and undetermined coefficients.

Moreover, the coefficients $\left(c_j\right)$ are determined by satisfying the governing equations in a weighted-integral sense over each element. The known functions $\left(\phi_j\right)$ are often taken as polynomials and they are derived using concepts from interpolation theory and are called "interpolation functions or shape functions". Therefore, $u = u_h = \sum c_j \phi_j$ is the approximate solution over the domain, Ω representing the governing partial differential equation.

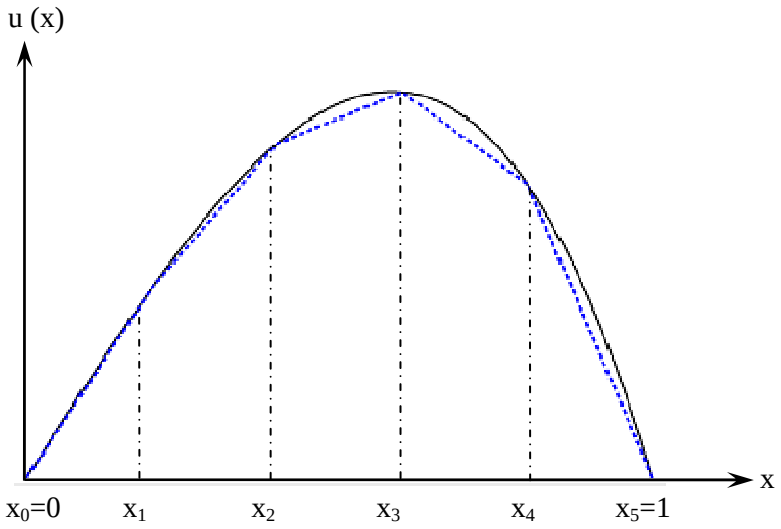

Fig. 3.6 Piecewise linear approximation of a function in the finite element method.

The technique of applying governing equation into elementwise sense in FEM can be explained from the following example. Let us consider a problem of solving differential equation in the following form:

$$L(u) = f \quad \text{.....(3.23)}$$

where L is a differential operator acting on dependent variable (u) and f is a known function of the independent variables. The solution for u can be approximated as:

$$u(x) \approx U_N(\mathbf{x}) = \sum_{j=1}^{N} c_j \phi_j(\mathbf{x}) + \phi_0(\mathbf{x}) \quad \text{.....(3.24)}$$

Substitution of the approximate solution $U_N(\mathbf{x})$ into the left hand side of the Eq. 3.23 gives a function $L(U_N)$, which in general is not equal to the specified function f. The difference $L(U_N) - f$, called residual of the approximation is non-zero:

$$R \equiv L(U_N) - f = L\left(\sum_{j=1}^{N} c_j \phi_j(\mathbf{x}) + \phi_0(\mathbf{x})\right) - f \neq 0 \quad \text{.....(3.25)}$$

The parameters (c_i) are computed by setting residual (R) to vanish in the weighted-integral sense, is known as weighted-residual method:

$$\int_\Omega \psi_i(\mathbf{x}) R(\mathbf{x}, c_j)\, d\Omega = 0 \quad (i = 1, 2, ...N) \quad \text{.....(3.26)}$$

where ψ_i are the weight functions, not necessarily be the same as approximation function (ϕ_i).

Now, from Eq. 3.26, the special cases of weighted-residual method can be summarized as:

Galerkin method: $\psi_i = \phi_i$

Petrov-Galerkin method: $\psi_i \neq \phi_i$

Least squares method: $\psi_i = \partial R / \partial c_i$ ……...……(3.27)

Collocation method: $\psi_i = \delta\left(\mathbf{x} - \mathbf{x}^i\right)$

Therefore, with Galerkin approach $\left(\psi_i = \phi_i\right)$, discretization of Eq. 3.23 yields:

$\mathbf{Kc = F}$ ……..……...(3.28)

where

$$K_{ij} = \int_\Omega \phi_i L\left(\phi_j\right) d\Omega$$
$$F_i = \int_\Omega \phi_i \left[f - L\left(\phi_0\right)\right] d\Omega \quad \text{...……(3.29)}$$

3.2.1 Discretization in Space

We use 4-node quadrilaterals for spatial discretization of two-dimensional domain, while 20-node brick element for three-dimensional domain. The local coordinate and shape functions of general quadrilateral elements in two dimensions are given in **Fig. 3.7** and Eq. 3.30 respectively. A complete list of shape function and nodal numbering for 2D and 3D elements are listed in Appendix F.

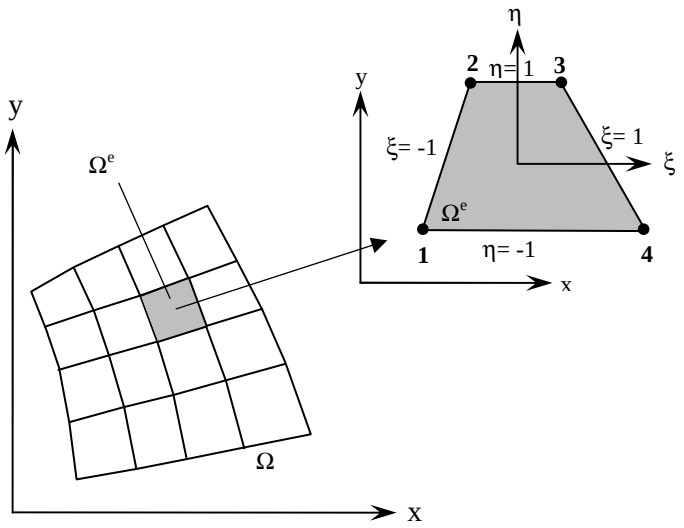

Fig. 3.7 Global and local coordinate system of quadrilateral elements.

$$N_1 = \frac{1}{4}(1-\xi)(1-\eta);\ N_2 = \frac{1}{4}(1-\xi)(1+\eta)$$
$$N_3 = \frac{1}{4}(1+\xi)(1+\eta);\ N_4 = \frac{1}{4}(1+\xi)(1-\eta) \quad \text{……...……..……(3.30)}$$

Similarly, derivatives can be converted from local to global coordinate system by using chain rule of partial differentiation. For example, the partial differentiation in global coordinates (x, y) is related to local coordinates (ξ, η) as:

$$\begin{Bmatrix} \frac{\partial}{\partial x} \\ \frac{\partial}{\partial y} \end{Bmatrix} = [\mathbf{J}]^{-1} \begin{Bmatrix} \frac{\partial}{\partial \xi} \\ \frac{\partial}{\partial \eta} \end{Bmatrix} \text{……...….(3.31)}$$

Here, $[\mathbf{J}]$ is the Jacobian matrix and can be found explicitly in terms of the local coordinate.

$$[\mathbf{J}]=\begin{bmatrix}\frac{\partial x}{\partial \xi} & \frac{\partial y}{\partial \xi}\\ \frac{\partial x}{\partial \eta} & \frac{\partial y}{\partial \eta}\end{bmatrix} \quad \text{.....(3.32)}$$

Similarly, in three dimensions:

$$\begin{Bmatrix}\frac{\partial}{\partial x}\\ \frac{\partial}{\partial y}\\ \frac{\partial}{\partial z}\end{Bmatrix}=[\mathbf{J}]^{-1}\begin{Bmatrix}\frac{\partial}{\partial \xi}\\ \frac{\partial}{\partial \eta}\\ \frac{\partial}{\partial \zeta}\end{Bmatrix} \quad \text{.....(3.33)}$$

The Jacobian matrix $[\mathbf{J}]$ is given as:

$$[\mathbf{J}]=\begin{bmatrix}\frac{\partial x}{\partial \xi} & \frac{\partial y}{\partial \xi} & \frac{\partial z}{\partial \xi}\\ \frac{\partial x}{\partial \eta} & \frac{\partial y}{\partial \eta} & \frac{\partial z}{\partial \eta}\\ \frac{\partial x}{\partial \zeta} & \frac{\partial y}{\partial \zeta} & \frac{\partial z}{\partial \zeta}\end{bmatrix} \quad \text{.....(3.34)}$$

Numerical integrations in the FEM are carried out using Gauss-Legendre quadrature over the element; in which the evaluation of integrand is combined to obtain an approximation to the integral. Furthermore, the integrand is computed at some points called “integration or sampling points” and weighted sum of these values forms the approximate integral, known as the “quadrature rule”. For example, the integration of a function in two dimensions can be computed as (Smith and Griffiths 1998):

$$\iint dxdy = \int_{-1}^{1}\int_{-1}^{1} \det|\mathbf{J}| d\xi d\eta$$
$$\int_{-1}^{1}\int_{-1}^{1} f(\xi,\eta)\det|\mathbf{J}| d\xi d\eta \approx \sum_{i=1}^{n}\sum_{j=1}^{n} \det|\mathbf{J}| w_i w_j f(\xi_i,\eta_i) \quad \text{……..(3.35)}$$

and in three dimensions:

$$\iiint dxdydz = \int_{-1}^{1}\int_{-1}^{1}\int_{-1}^{1} \det|\mathbf{J}| d\xi d\eta d\zeta$$
$$\int_{-1}^{1}\int_{-1}^{1}\int_{-1}^{1} f(\xi,\eta,\zeta)\det|\mathbf{J}| d\xi d\eta d\zeta \approx \sum_{i=1}^{n}\sum_{j=1}^{n}\sum_{j=1}^{n} \det|\mathbf{J}| w_i w_j w_k f(\xi_i,\eta_i,\zeta_i) \quad \text{…..…..……(3.36)}$$

in which $\det|\mathbf{J}|$ is the determinant of Jacobian matrix, it describes the amount of "expansion" that coordinate transformation imposes. Similarly, w_i, w_j, w_k and ξ_i, η_i, ζ_i are the weighting coefficients and the sampling points, respectively, within the element and values of these coefficients can be found in Stroud and Secrest (1966).

3.2.2 Discretization in Time

There are various ways to discretize time steps in FEM formulation of time dependent problems (Zienkiewicz and Taylor 1991); in many engineering applications, the methods involving “linear interpolation” and fixed time step (Δt) are popular (Smith and Griffiths 1998). For example, a typical FEM discretization of transient partial differential equation in matrix form is:

$$[\mathbf{K}]\{\mathbf{U}\} + [\mathbf{M}]\left\{\frac{d\mathbf{U}}{dt}\right\} = \{\mathbf{Q}\} \quad \text{……(3.37)}$$

where **U** and **Q** are the vectors of dependent variable and sources/sinks respectively; **K** and **M** represent the stiffness and mass matrix. Eq. 3.37 can be written for two consecutive time steps "0" and "1" as follows:

$$[\mathbf{K}]\{\mathbf{U}\}_0 + [\mathbf{M}]\left\{\frac{d\mathbf{U}}{dt}\right\}_0 = \{\mathbf{Q}\}_0 \quad \text{.....(3.38)}$$

$$[\mathbf{K}]\{\mathbf{U}\}_1 + [\mathbf{M}]\left\{\frac{d\mathbf{U}}{dt}\right\}_1 = \{\mathbf{Q}\}_1 \quad \text{.....(3.39)}$$

The gradients of **U** is approximated by a linear interpolation between its values at the two time steps:

$$\frac{\{\mathbf{U}\}_1 - \{\mathbf{U}\}_0}{\Delta t} \approx (1-\theta)\left\{\frac{d\mathbf{U}}{dt}\right\}_0 + \theta\left\{\frac{d\mathbf{U}}{dt}\right\}_1 \quad \text{.....(3.40)}$$

Therefore,

$$\{\mathbf{U}\}_1 = \{\mathbf{U}\}_0 + \Delta t\left((1-\theta)\left\{\frac{d\mathbf{U}}{dt}\right\}_0 + \theta\left\{\frac{d\mathbf{U}}{dt}\right\}_1\right) \quad \text{.....(3.41)}$$

where θ lies between 0 and 1.

Substituting the values of $\left\{\frac{d\mathbf{U}}{dt}\right\}_0$ and $\left\{\frac{d\mathbf{U}}{dt}\right\}_1$ from those in Eqs. 3.38 and 3.39 into Eq. 3.41, we get following reoccurrence equation between "0" and "1" time steps:

$$\begin{aligned}\left([\mathbf{M}] + \theta\Delta t[\mathbf{K}]\right)\{\mathbf{U}\}_1 = {} & \left([\mathbf{M}] - (1-\theta)\Delta t[\mathbf{K}]\right)\{\mathbf{U}\}_0 \\ & + \theta\Delta t\{\mathbf{Q}\}_1 + (1-\theta)\Delta t\{\mathbf{Q}\}_0\end{aligned} \quad \text{.....(3.42)}$$

where $\theta = 0$ (explicit), $\theta = 1$ (implicit) and $\theta = 1/2$ (Crank-Nicolson).

3.2.3 Streamline Upwind Petrov-Galerkin (SUPG) Method

The standard Galerkin finite element approaches often fail while solving advection-dominated problems, such as Eqs. 2.29 and 2.32. Generally, “stabilized techniques” (such as streamline upwinding or least squares) are adopted to overcome the drawbacks of Galerkin methods in which the bilinear form associated with the problem is artificially modified so that numerical stability is achieved without compromising consistency. One of the stabilized techniques within the category of weighted residual methods is Streamline upwind Petrov-Galerkin (SUPG) method (Brooks and Hughes 1982).

In SUPG, the standard Galerkin weighting functions the weighting functions are modified in an unsymmetrical way in the upwind direction, with the additional function proportional to the gradient of the weighting function. By applying the modified weighting function to all terms in the governing equation, it results a consistent weighted residual formulation (Brooks and Hughes 1982). For example, let us consider a 1D advection-diffusion equation to formulate FEM:

$$\begin{aligned} &\Phi_{,t} + u\Phi_{,x} - D\Phi_{,xx} = 0 \\ &\Phi(0,t) = 1, \Phi(x,0) = 0 \end{aligned} \quad \text{.....(3.43)}$$

where Φ is the variable of interest (temperature, concentration, etc.); u is the velocity and D is the diffusivity for the process.

The SUPG weighted residual formulation for the initial boundary value problem (Eq. 3.43) is :

$$\int_\Omega \left(w\Phi_{,t} + wu\Phi_{,x} + w_{,i} D\Phi_{,x} \right) d\Omega + \sum_e \int_{\Omega^e} \omega \left(\Phi_{,t} + u\Phi_{,x} - D\Phi_{,xx} \right) d\Omega = 0 \quad \text{.....(3.44)}$$

In Eq. 3.44, the first term represents the Galerkin component and the second term is the SUPG stabilization contribution, in which w is Galerkin weighting function and ω is the SUPG weighting function. Therefore, the modified weighting function for convective term can be written in following form:

$$\bar{w} = w + \omega \quad \text{……(3.45)}$$

and

$$\omega = \frac{\bar{k} u_j w_{,j}}{\|u\|};$$
$$\bar{k} = \left(\frac{uh}{2}\right)\bar{\xi},$$
$$\bar{\xi} = \coth(\mathrm{Pe}) - \frac{1}{\mathrm{Pe}} \quad \text{……..……..(3.46)}$$
$$\mathrm{Pe} = \frac{uh}{2D}$$

where h is average element length, $\bar{k}$ is the stabilization parameter and Pe is the element Peclet number.

This method has been widely used in solving steady sate advection-diffusion problems in order to eliminate numerical oscillation, however, when it comes to transient problems, additional difficulties may arise associated with occurrence of local oscillations normally associated with sharp transient loads (Wood and Lewis 1975).

3.2.4 Finite Element Method for Fluid, Heat and Solute Flow in the Fracture

For a conventional Galerkin approach to the finite element modeling of 2D reactive flow and transport in the fracture, the following interpolating functions for an element (m) are considered.

$$\begin{aligned} p^{(m)} &= \mathbf{N}^{(m)}\tilde{\mathbf{p}}, D_f^{(m)} = \mathbf{N}^{(m)}\tilde{\mathbf{D}}_{\mathbf{F}} \\ T^{(m)} &= \mathbf{N}^{(m)}\tilde{\mathbf{T}}, D_h^{(m)} = \mathbf{N}^{(m)}\tilde{\mathbf{D}}_{\mathbf{H}} \\ c^{(m)} &= \mathbf{N}^{(m)}\tilde{\mathbf{c}}, D_s^{(m)} = \mathbf{N}^{(m)}\tilde{\mathbf{D}}_{\mathbf{S}} \end{aligned} \quad \text{……...……(3.47)}$$

where $\mathrm{N}^{(m)}$ are interpolative functions. Similarly, $\tilde{\mathbf{p}}$, $\tilde{\mathbf{D}}_{\mathbf{F}}$, $\tilde{\mathbf{T}}$, $\tilde{\mathbf{D}}_{\mathbf{H}}$, $\tilde{\mathbf{c}}$ and $\tilde{\mathbf{D}}_{\mathbf{S}}$ are the vectors of fluid pressure, source intensity (fluid); temperature, source intensity (heat), concentration and source intensity (solute), respectively, at the element nodes.

Discretization of the governing equations for pressure, temperature, and concentration in the fracture (Eqs. 2.23, 2.29 and 2.32) to form the "stiffness matrix" yields the following system of equations:

$$\mathbf{A_1}\tilde{\mathbf{p}}(\mathbf{t}) + \mathbf{A_2}\tilde{\mathbf{D}}_{\mathbf{F}}(\mathbf{t}) = \mathbf{B_1}(\mathbf{t}) \text{ ……...…..…(3.48)}$$

$$\mathbf{A_3}\tilde{\mathbf{T}}(\mathbf{t}) + \mathbf{A_4}\tilde{\mathbf{D}}_{\mathbf{H}}(\mathbf{t}) = \mathbf{0} \text{ ……...…....(3.49)}$$

$$\mathbf{A_5}\tilde{\mathbf{c}}(\mathbf{t}) + \mathbf{A_6}\tilde{\mathbf{D}}_{\mathbf{S}}(\mathbf{t}) = \mathbf{B_2}(\mathbf{t}) \text{ ……..……...…(3.50)}$$

where

$$\mathbf{A_1} = \sum_{m=1}^{M} \int_{A_e} \frac{w^3}{12\mu} \nabla^T \mathbf{N}^{(m)} \nabla \mathbf{N}^{(m)} dA \text{ ……....(3.51)}$$

$$\mathbf{A_2} = \sum_{m=1}^{M} \int_{A_e} \mathbf{N}^{(m)T} \mathbf{N}^{(m)} dA \text{ ……..(3.52)}$$

$$\mathbf{B_1} = -\sum_{m=1}^{M}\int_{A_e}\frac{\partial w}{\partial t}\mathbf{N}^{(m)T}dA + \sum \mathbf{N}^{(i)T}\Big|_{(x_i,y_i)} Q_i(t) - \sum \mathbf{N}^{(e)T}\Big|_{(x_e,y_e)} Q_e(t) \quad \text{.....(3.53)}$$

$$\mathbf{A_3} = \rho_f c_f \sum_{m=1}^{M}\int_{A_e}\left(\mathbf{N}^{(m)} + \bar{\mathbf{N}}^{(m)}\right)\mathbf{q}(x,y)\nabla\mathbf{N}^{(m)}dA \quad \text{.....(3.54)}$$

$$\mathbf{A_4} = \sum_{m=1}^{M}\int_{A_e}\mathbf{N}^{(m)T}\mathbf{N}^{(m)}dA \quad \text{.....(3.55)}$$

$$\mathbf{A_5} = \sum_{m=1}^{M}\int_{A_e}\left(\mathbf{N}^{(m)} + \bar{\mathbf{N}}^{(m)}\right)\mathbf{q}(x,y)\nabla\mathbf{N}^{(m)}dA + 2\sum_{m=1}^{M}\int_{A_e}\mathbf{K}\ \mathbf{N}^{(m)T}\mathbf{N}^{(m)}dA \quad \text{.....(3.56)}$$

$$\mathbf{A_6} = \sum_{m=1}^{M}\int_{A_e}\mathbf{N}^{(m)T}\mathbf{N}^{(m)}dA \quad \text{.....(3.57)}$$

$$\mathbf{B_2} = 2\sum_{m=1}^{M}\int_{A_e}\mathbf{K}\mathbf{c}_{eq}\ \mathbf{N}^{(m)T}dA \quad \text{.....(3.58)}$$

$$\bar{\mathbf{N}}^{(m)} = \frac{\bar{k}q_j\mathbf{N}^{(m)}_{,j}}{q_i q_i}, \quad i = x, y;\ j = x, y \quad \text{.....(3.59)}$$

in which M is the total number of elements on the fracture plane, $\mathbf{N}^{(i)T}\Big|_{x_i,y_i}$ denotes the shape functions at the injection well which is located at (x_i, y_i) within element i and $\mathbf{N}^{(e)T}\Big|_{(x_e,y_e)}$ denotes the shape functions at the extraction well located at (x_e, y_e) within element e.

We adopt the SUPG technique (Brooks and Hughes 1982) in the FEM to solve convection dominated heat transport due to numerical oscillations in conventional Galerkin finite element. The “upwind” parameter $\bar{k}$ is computed from Eq. 3.46.

3.3 Hybrid BEFEM Model

It is well known that the FEM is suitable for solving non-linear problems and problems involving heterogeneous domain whereas the BEM has advantage of reducing the problem dimension by “one” as only boundaries required to discretize. The ideal methodology would be to combine both the techniques to form a hybrid model. Therefore, in the proposed hybrid BEFEM model, the BEM computes linear solution and handles the infinite zone whereas FEM solves reservoir region with capability of nonlinearity and heterogeneity consideration.

The hybrid BEFEM model is constructed via two classes of coupling of BEM and FEM, for example, in problem involving:

i. fracture-matrix system, using “direct substitution”.
ii. reservoir layer-surrounding strata, using “iterative procedure”.

The details of the integration technique are described in the following subsections.

3.3.1 Thermo-Poroelastic-Chemo Module for Fracture-Matrix System

Recalling that to solve governing equations for stresses, pressure, temperature and concentration in the reservoir matrix, we need the boundary conditions in the BEM and these are not known but can be obtained from FEM; which forms the basis of coupling BEM with FEM. For example, the normal stresses at the fracture surface and fluid pressure in the fracture are interrelated; fracture widths are computed from the displacement discontinuity (DD) and sources intensity (e.g., of fluid, heat or solute) are

continuous at the fracture and rock-matrix interface. The procedure of the coupling BEM and FEM is described next.

In this formulation, the integration of finite element and boundary element method is achieved by discretizing the respective governing equations and integral equations at the interface of problem domain (in this case fracture surface, using the same mesh in both methods) and solving a system of algebraic equations formed after combining these discretized equations. The finite element method considers the two-dimensional fracture flow as described in Section **3.2.4**, while boundary element method represents the thermo-poroelastic response of the rock-matrix described in Section **3.1.1.**

Using the discretization and variable approximations described previously for 3D BEM (cf. Fig. 3.3) and FEM formulation (cf. Section **3.2**), stress, pore pressure, temperature and concentration and their respective source intensities are approximated as:

$$\begin{aligned}
&\sigma_n^{(m)} = 1\ \tilde{\sigma}_n \\
&p^{(m)} = \mathbf{N}^{(m)}\tilde{\mathbf{p}}, D_f^{(m)} = \mathbf{N}^{(m)}\tilde{\mathbf{D}}_F \\
&T^{(m)} = \mathbf{N}^{(m)}\tilde{\mathbf{T}}, D_h^{(m)} = \mathbf{N}^{(m)}\tilde{\mathbf{D}}_H \\
&c^{(m)} = \mathbf{N}^{(m)}\tilde{\mathbf{c}}, D_s^{(m)} = \mathbf{N}^{(m)}\tilde{\mathbf{D}}_S
\end{aligned} \quad \text{.....(3.60)}$$

The FEM formulations representing the governing fracture flow, heat and solute transport can be summarized from Section **3.2.4** as:

$$\mathbf{A_1}\tilde{\mathbf{p}}(\mathbf{t}) + \mathbf{A_2}\tilde{\mathbf{D}}_{\mathbf{F}}(\mathbf{t}) = \mathbf{B_1}(\mathbf{t}) \quad \text{.....(3.61)}$$

$$\mathbf{A_3}\tilde{\mathbf{T}}(\mathbf{t}) + \mathbf{A_4}\tilde{\mathbf{D}}_{\mathbf{H}}(\mathbf{t}) = \mathbf{0} \quad \text{.....(3.62)}$$

$$\mathbf{A_5}\tilde{\mathbf{c}}(\mathbf{t}) + \mathbf{A_6}\tilde{\mathbf{D}}_{\mathbf{S}}(\mathbf{t}) = \mathbf{B_2}(\mathbf{t}) \quad \text{.....(3.63)}$$

where the "stiffness matrices" $(\mathbf{A_1}, \mathbf{A_2}, \mathbf{A}_3, \mathbf{A}_4, \mathbf{A}_5$ and $\mathbf{A}_6)$ and "load vectors" $(\mathbf{B_1}$ and $\mathbf{B}_2)$ are defined previously (cf. Section **3.2.4**).

To form "stiffness matrix" of integral equations and thus system of algebraic equations, we apply the discretized equations for stress (Eq. 3.13) on element centers while the equations for pore pressure (Eq. 3.14), temperature (Eq. 3.15) and concentration (Eq. 3.16) are collocated on all element nodes at the same mesh in FEM: These algebraic equations can be written in vector form:

$$\boldsymbol{\sigma}_\mathbf{n} = \mathbf{A_7}\tilde{\mathbf{D}}_n(\mathbf{t}) + \mathbf{A_8}\tilde{\mathbf{D}}_F(\mathbf{t}) + \mathbf{A_9}\tilde{\mathbf{D}}_H(\mathbf{t}) + \boldsymbol{\sigma}_{\mathbf{n1}} + \boldsymbol{\sigma}_{\mathbf{n0}} \quad \text{.....(3.64)}$$

$$\tilde{\mathbf{p}} = \mathbf{A_{10}}\tilde{\mathbf{D}}_n(\mathbf{t}) + \mathbf{A}_{11}\tilde{\mathbf{D}}_F(\mathbf{t}) + \mathbf{p_1} + \mathbf{p_0} \quad \text{.....(3.65)}$$

$$\tilde{\mathbf{T}} = \mathbf{A_{12}}\tilde{\mathbf{D}}_H(\mathbf{t}) + \mathbf{T_1} + \mathbf{T_0} \quad \text{.....(3.66)}$$

$$\tilde{\mathbf{c}} = \mathbf{A_{13}}\tilde{\mathbf{D}}_S(\mathbf{t}) + \mathbf{c_1} + \mathbf{c_0} \quad \text{.....(3.67)}$$

where the vectors $\boldsymbol{\sigma}_{\mathbf{n0}}$, $\boldsymbol{\sigma}_{\mathbf{n1}}$, $\mathbf{p_0}$, $\mathbf{p_1}$, $\mathbf{T_0}$, $\mathbf{T_1}$, $\mathbf{c_0}$ and $\mathbf{c_1}$ are as defined previously and the coefficient matrices are:

$$\mathbf{A_7} = \begin{bmatrix} \sum_{m=1}^{M} \int_{A_e} \sigma_{nn}^{cD}(x_1 - x', y_1 - y', 0, \Delta t)\, dx'dy' \\ \sum_{m=1}^{M} \int_{A_e} \sigma_{nn}^{cD}(x_2 - x', y_2 - y', 0, \Delta t)\, dx'dy' \\ \vdots \\ \sum_{m=1}^{M} \int_{A_e} \sigma_{nn}^{cD}(x_M - x', y_M - y', 0, \Delta t)\, dx'dy' \end{bmatrix} \quad \text{.....(3.68)}$$

$$\mathbf{A_8} = \begin{bmatrix} \sum_{m=1}^{M} \int_{A_e} \mathbf{N}^{(m)} \sigma_n^{cF}\left(x_1 - x', y_1 - y', 0, \Delta t\right) dx'dy' \\ \sum_{m=1}^{M} \int_{A_e} \mathbf{N}^{(m)} \sigma_n^{cF}\left(x_2 - x', y_2 - y', 0, \Delta t\right) dx'dy' \\ \vdots \\ \sum_{m=1}^{M} \int_{A_e} \mathbf{N}^{(m)} \sigma_n^{cF}\left(x_M - x', y_M - y', 0, \Delta t\right) dx'dy' \end{bmatrix} \quad \text{.....(3.69)}$$

$$\mathbf{A_9} = \begin{bmatrix} \sum_{m=1}^{M} \int_{A_e} \mathbf{N}^{(m)} \sigma_n^{cH}\left(x_1 - x', y_1 - y', 0, \Delta t\right) dx'dy' \\ \sum_{m=1}^{M} \int_{A_e} \mathbf{N}^{(m)} \sigma_n^{cH}\left(x_2 - x', y_2 - y', 0, \Delta t\right) dx'dy' \\ \vdots \\ \sum_{m=1}^{M} \int_{A_e} \mathbf{N}^{(m)} \sigma_n^{cH}\left(x_M - x', y_M - y', 0, \Delta t\right) dx'dy' \end{bmatrix} \quad \text{.....(3.70)}$$

$$\mathbf{A_{10}} = \begin{bmatrix} \sum_{m=1}^{M} \int_{A_e} p_n^{cD}\left(x_1 - x', y_1 - y', 0, \Delta t\right) dx'dy' \\ \sum_{m=1}^{M} \int_{A_e} p_n^{cD}\left(x_2 - x', y_2 - y', 0, \Delta t\right) dx'dy' \\ \vdots \\ \sum_{m=1}^{M} \int_{A_e} p_n^{cD}\left(x_{TN} - x', y_{TN} - y', 0, \Delta t\right) dx'dy' \end{bmatrix} \quad \text{.....(3.71)}$$

$$\mathbf{A_{11}} = \begin{bmatrix} \sum_{m=1}^{M} \int_{A_e} \mathbf{N}^{(m)} p^{cF}\left(x_1 - x', y_1 - y', 0, \Delta t\right) dx'dy' \\ \sum_{m=1}^{M} \int_{A_e} \mathbf{N}^{(m)} p^{cF}\left(x_2 - x', y_2 - y', 0, \Delta t\right) dx'dy' \\ \vdots \\ \sum_{m=1}^{M} \int_{A_e} \mathbf{N}^{(m)} p^{cF}\left(x_{TN} - x', y_{TN} - y', 0, \Delta t\right) dx'dy' \end{bmatrix} \quad \text{.....(3.72)}$$

$$\mathbf{A_{12}} = \begin{bmatrix} \sum_{m=1}^{M} \int_{A_e} \mathbf{N}^{(m)} T^{cH}\left(x_1 - x', y_1 - y', 0, \Delta t\right) dx' dy' \\ \sum_{m=1}^{M} \int_{A_e} \mathbf{N}^{(m)} T^{cH}\left(x_2 - x', y_2 - y', 0, \Delta t\right) dx' dy' \\ \vdots \\ \sum_{m=1}^{M} \int_{A_e} \mathbf{N}^{(m)} T^{cH}\left(x_{TN} - x', y_{TN} - y', 0, \Delta t\right) dx' dy' \end{bmatrix} \quad \text{.....(3.73)}$$

$$\mathbf{A_{13}} = \begin{bmatrix} \sum_{m=1}^{M} \int_{A_e} \mathbf{N}^{(m)} C^{cs}\left(x_1 - x', y_1 - y', 0\right) dx' dy' \\ \sum_{m=1}^{M} \int_{A_e} \mathbf{N}^{(m)} C^{cs}\left(x_2 - x', y_2 - y', 0\right) dx' dy' \\ \vdots \\ \sum_{m=1}^{M} \int_{A_e} \mathbf{N}^{(m)} C^{cs}\left(x_{TN} - x', y_{TN} - y', 0\right) dx' dy' \end{bmatrix} \quad \text{.....(3.74)}$$

All the matrices and vectors (Eqs. 3.68 through 3.74) can be evaluated directly. The system of Eqs. 3.61 through 3.67 has total $\left(6NT + 2M\right)$ unknowns $\left(\boldsymbol{\sigma}_{\mathbf{n}}, \tilde{\mathbf{p}}, \tilde{\mathbf{T}}, \tilde{\mathbf{c}}, \tilde{\mathbf{D}}_n, \tilde{\mathbf{D}}_F, \tilde{\mathbf{D}}_H, \tilde{\mathbf{D}}_S\right)$ and $\left(6TN + M\right)$ equations. One more $\left(M\right)$ set of equations is provided by using "joint model" (Crouch and Starfield 1983)–describing the relationship between the stress increment and displacement discontinuity (cf. Section **2.3.3**). For example, if element $\left(m\right)$ is closed, the increment of the normal effective stress for element $\left(m\right)$ can be calculated by:

$$\Delta \overset{m}{\sigma}'_n = -\overset{m}{K}_n \overset{m}{D}_n \quad \text{.....(3.75)}$$

If element $\left(m\right)$ is open, we have $\overset{m}{\sigma}'_n = 0$. The following separation criterion is adopted to judge whether the element $\left(m\right)$ is closed or open:

$$\overset{m}{\sigma_n'} = -\overset{m}{c_j}\,\text{cotan}\,\overset{\text{m}}{\phi_{eff}} \quad \text{.....(3.76)}$$

3.3.1.1 Solution Procedure

The current transient problem is solved by marching in the time domain. The current numerical scheme leads to non-linear equation system because of the dependence of fracture aperture on fluid pressure, thermo- and poroelastic stresses in the reservoir. To avoid this numerical difficulty, successive iterations are performed within the each time step till the convergence achieved, for example:

$$\left\|\mathbf{w}_l^k - \mathbf{w}_l^{k-1}\right\| \Big/ \left\|\mathbf{w}_l^{k-1}\right\| < \varepsilon_{\text{conv}} \quad \text{.....(3.77)}$$

where $\mathbf{w}_l^k$ is the fracture aperture vector at k^{th} iteration in l^{th} time. For the example presented in this dissertation, we set $\varepsilon_{\text{conv}} = 0.5\%$.

Given initial fracture aperture distribution, we solve Eqs. 3.61 through 3.67 in following steps, “iteratively” (see **Fig. 3.8**).

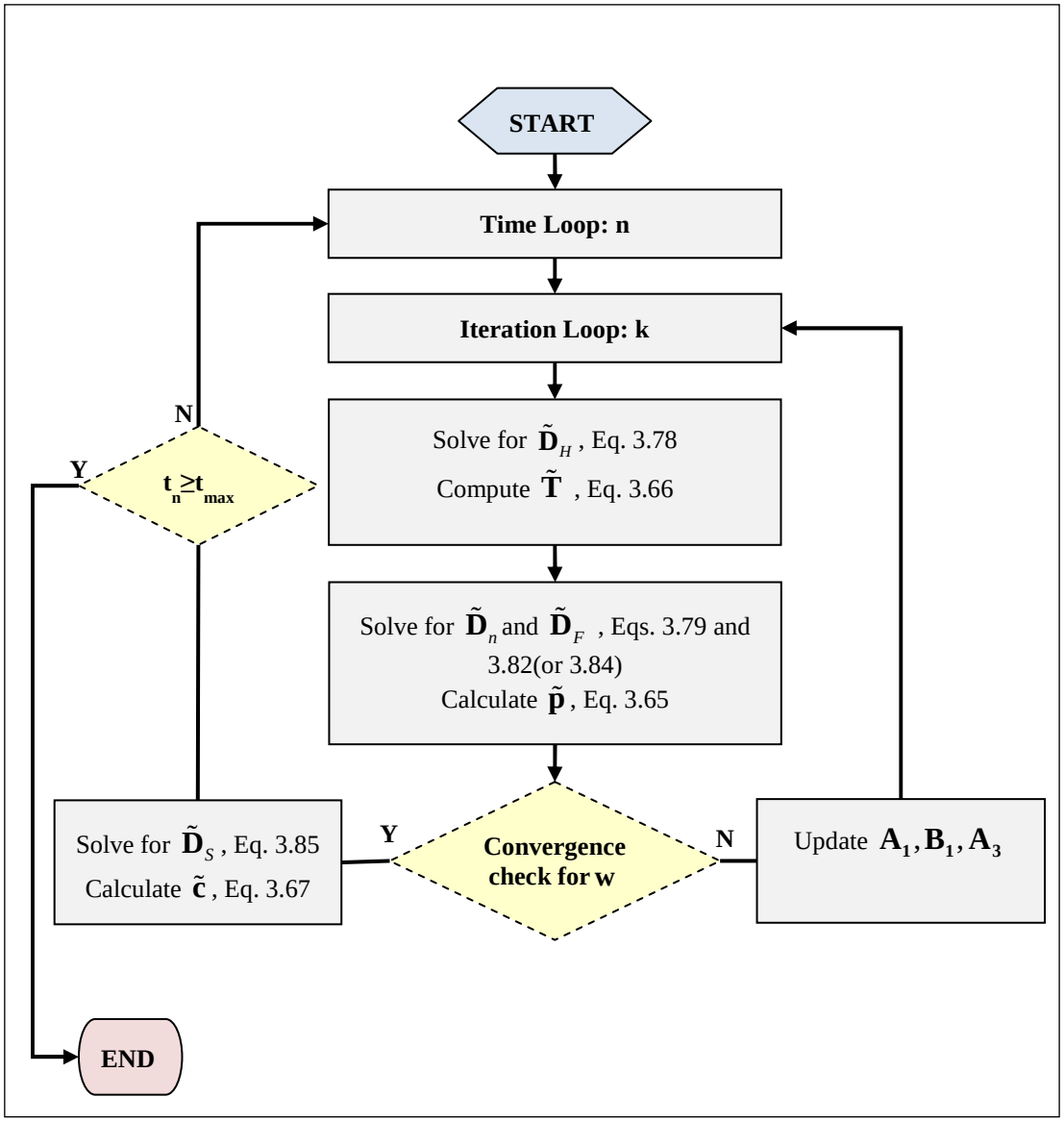

Fig. 3.8 Flowchart of the integration approach for fracture-matrix system: The iteration loop is to account the non-linearity present between fluid pressure and fracture width.

Steps used to solve for the temperature are:

1. As the rock temperature is independent on the stress state, the heat source intensity $\left(\tilde{\mathbf{D}}_H\right)$ can be computed directly. For example, by inserting expression of temperature $\left(\tilde{\mathbf{T}}\right)$ from Eq. 3.66 into Eq. 3.62, the heat source intensity $\left(\tilde{\mathbf{D}}_H\right)$ is solved from:

$$\left(\mathbf{A_3A_{12}} + \mathbf{A_4}\right)\tilde{\mathbf{D}}_H\left(\mathbf{t}\right) = \mathbf{-A_3}\left(\mathbf{T_1} + \mathbf{T_0}\right) \quad \text{.....(3.78)}$$

2. Calculate temperature $\left(\tilde{\mathbf{T}}\right)$ from using Eq. 3.66 with known $\tilde{\mathbf{D}}_H$ from Eq. 3.78.

Steps used to solve for the pressure are:

3. The fluid pressure, fluid source intensity and displacement discontinuity are solved simultaneously using system of equations (Eqs. 3.61, 3.64 and 3.65). First, substitute expression for fluid pressure $\left(\tilde{\mathbf{p}}\right)$ from Eq. 3.65 into Eq. 3.61, to get expression for unknowns $\tilde{\mathbf{D}}_n\left(t\right)$ and $\tilde{\mathbf{D}}_F\left(t\right)$ as:

$$\mathbf{A_1A_{10}}\tilde{\mathbf{D}}_n\left(t\right) + \left(\mathbf{A_1A_{11}} + \mathbf{A_2}\right)\tilde{\mathbf{D}}_F\left(t\right) = \mathbf{B_1}\left(\mathbf{t}\right) - \mathbf{A_1}\left(\mathbf{p_1} + \mathbf{p_0}\right) \quad \text{.....(3.79)}$$

Similarly, the second expression for unknowns $\tilde{\mathbf{D}}_n\left(t\right)$ and $\tilde{\mathbf{D}}_F\left(t\right)$ is obtained by rearranging terms in Eq 3.64 as:

$$\mathbf{A_7}\tilde{\mathbf{D}}_n\left(\mathbf{t}\right) + \mathbf{A_8}\tilde{\mathbf{D}}_F\left(\mathbf{t}\right) = \boldsymbol{\sigma}_\mathbf{n} - \boldsymbol{\sigma}_\mathbf{n0} - \boldsymbol{\sigma}_\mathbf{n1} - \mathbf{A_9}\tilde{\mathbf{D}}_H\left(\mathbf{t}\right) \quad \text{.....(3.80)}$$

Furthermore, the unknown induced stresses $\left(\boldsymbol{\sigma}_\mathbf{n} - \boldsymbol{\sigma}_\mathbf{n0}\right)$ Eq. 3.80 are found using the "joint model" (cf. Section **2.3.3**). The induced stresses $\left(\boldsymbol{\sigma}_\mathbf{n} - \boldsymbol{\sigma}_\mathbf{n0}\right)$ for any

element are evaluated differently (depending upon whether the element is closed or open). For example, if element (m) is closed, the induced stress becomes:

$$\begin{aligned}\overset{m}{\sigma}_n - \overset{m}{\sigma}_{n0} &= \left(\overset{m}{\sigma'}_n + \overset{m}{p}\right) - \left(\overset{m}{\sigma'}_{n0} + \overset{m}{p}_0\right) = \left(\overset{m}{p} - \overset{m}{p}_0\right) + \left(\overset{m}{\sigma'}_n - \overset{m}{\sigma'}_{n0}\right) \\ &= \left(\overset{m}{p} - \overset{m}{p}_0\right) - \overset{m}{K}_n \overset{m}{\tilde{D}}_n\end{aligned} \quad \text{.....(3.81)}$$

Therefore, after substituting $(\boldsymbol{\sigma}_\mathbf{n} - \boldsymbol{\sigma}_\mathbf{n0})$ from Eq. 3.81 into Eq. 3.80, it yields:

$$\left(\mathbf{A_7} - \mathbf{A_{10}} + \mathbf{K}_n\right)\tilde{\mathbf{D}}_n(\mathbf{t}) + \left(\mathbf{A_8} - \mathbf{A}_{11}\right)\tilde{\mathbf{D}}_F(\mathbf{t}) = \mathbf{p_1} - \boldsymbol{\sigma}_\mathbf{n1} - \mathbf{A_9}\tilde{\mathbf{D}}_H(\mathbf{t}) \text{.....(3.82)}$$

while for any element (m) that is open, it leads to:

$$\overset{m}{\sigma}_n - \overset{m}{\sigma}_{n0} = \overset{m}{p} - \overset{m}{\sigma}_{n0} \text{.....(3.83)}$$

and after substituting $(\boldsymbol{\sigma}_\mathbf{n} - \boldsymbol{\sigma}_\mathbf{n0})$ from Eq.3.83 into Eq. 3.80, one can get:

$$\left(\mathbf{A_7} + \mathbf{A_{10}}\right)\tilde{\mathbf{D}}_n(\mathbf{t}) + \left(\mathbf{A_8} + \mathbf{A}_{11}\right)\tilde{\mathbf{D}}_F(\mathbf{t}) = \mathbf{p_1} + \mathbf{p_0} - \boldsymbol{\sigma}_\mathbf{n0} - \boldsymbol{\sigma}_\mathbf{n1} - \mathbf{A_9}\tilde{\mathbf{D}}_H(\mathbf{t}) \text{.....(3.84)}$$

Therefore, solve for $\tilde{\mathbf{D}}_n$ and $\tilde{\mathbf{D}}_F$ using system of equations (Eqs. 3.79 and 3.82 or 3.84)

4. Calculate fluid pressure $(\tilde{\mathbf{p}})$ by inserting known $\tilde{\mathbf{D}}_n$ and $\tilde{\mathbf{D}}_F$ into Eq. 3.65.

Steps used to solve for the concentration are:

5. Substitute expression of concentration $(\tilde{\mathbf{c}})$ from Eq. 3.67 into Eq. 3.63, the solute source intensity is solved from:

$$\left(\mathbf{A_5}\mathbf{A_{13}} + \mathbf{A_6}\right)\tilde{\mathbf{D}}_S(\mathbf{t}) = \mathbf{B}_2(\mathbf{t}) - \mathbf{A_5}\left(\mathbf{c_1} + \mathbf{c_0}\right) \text{.....(3.85)}$$

6. Concentration $(\tilde{\mathbf{c}})$ is computed by inserting known $\tilde{\mathbf{D}}_S$ into Eq. 3.67. It is important to note that mineral dissolution is not fully coupled with temperature and pressure, meaning that mineral dissolution and precipitation is computed once the all pressure, temperature and fracture aperture calculations are completed without further iteration.

Once $\tilde{\mathbf{D}}_H$, $\tilde{\mathbf{D}}_n$, $\tilde{\mathbf{D}}_F$ and $\tilde{\mathbf{D}}_S$ are solved, stress, pore pressure, temperature and concentration in any location in the reservoir are calculated using their expressions from Eqs. 3.64 through 3.67, respectively.

3.3.2 Poroelastic Module for Hydraulic Fracturing

In this module, considering quasi-static and mobile equilibrium approach (cf. 2.5), we formulate a numerical solution to simulate hydraulic fracturing. Hydraulic fracturing by water injection is extensively used to stimulate unconventional petroleum and geothermal reservoirs. The water is pumped at a high pressure into a selected section of the wellbore to create and extend a fracture(s) into the formation. The applied pressure in the fracture(s) re-distributes the pore pressure and stresses around the main fracture causing rock deformation and failure by fracture initiation and/or activation of discontinuities such as joints and bedding planes. The net result is often enhancement of the formation permeability. The rock failure process is often accompanied by micro-seismicity that can provide useful information regarding the stimulated volume.

The problem consists of flow in the fracture and coupled diffusion/deformation in the reservoir matrix. As water is the most commonly used fluid in stimulation of unconventional petroleum and geothermal reservoirs, it is assumed the fluid in the fracture is incompressible and Newtonian. Also, the rock matrix is assumed to be poroelastic with constant properties. We use a combination of the BEM and FEM to solve the coupled rock deformation and fracture flow problem. The 3D BEM representing poroelastic deformation and 2D FEM representing fracture flow are formulated according to the approach presented in Sections **3.1.1** and **3.2.4**, respectively. Once the stresses and pore pressures at field points around the main fracture are calculated, the results are used in a failure criterion to assess the potential for rock failure. The systems of equations for fluid pressure in the fracture, stress and pore pressure in the reservoir matrix and the solution procedure are described next.

Considering a fracture plane of arbitrary shape discretized using four-node quadrilateral elements with fluid pressure and leak-off velocity interpolation in an element (m) as $p^{(m)} = \mathbf{N}^{(m)}\tilde{\mathbf{p}}$ and $D_f{}^{(m)} = \mathbf{N}^{(m)}\tilde{\mathbf{D}}_f$, the finite element formula for governing fracture fluid flow equation (cf. Section **3.2.4**) can be written as:

$$\mathbf{A}_1\tilde{\mathbf{p}}(t) + \mathbf{A}_2\tilde{\mathbf{D}}_{\mathbf{F}}(t) = \mathbf{B}_1(t) \quad \text{.....(3.86)}$$

While solving for fluid pressure $(\tilde{\mathbf{p}})$, Eq. 3.86 behaves like Neumann equation since the prescription of the boundary conditions (Eqs. 2.26 and 2.27) is the second-type (Neumann). It means that the solution of Eq. 3.86 plus any arbitrary constant also satisfies Eq. 3.86. Therefore, to solve Eq. 3.86, we let the pressure $(\tilde{\mathbf{p}})$ on an arbitrary

nodal point is set equal to zero [see, for example, Becker et al. (1981) and Yew (1997)]. Then, the true fluid pressure is obtained by adding a constant pressure (P) to this solution $(\tilde{\mathbf{p}})$, i.e., $(\tilde{\mathbf{p}} + P)$. Global mass balance is required to ensure a unique solution to the problem [see, for example, Yew (1997)]; the discretized form of global mass balance equation (cf. Section **2.2.1**) is:

$$\Delta t \mathbf{A}_e \mathbf{T}_R \tilde{\mathbf{D}}_F + \mathbf{A}_e \tilde{\mathbf{D}}_n = Q_{inj} \Delta t + \mathbf{A}_e \tilde{\mathbf{D}}_n (N-1) \quad \text{.....(3.87)}$$

Here, $\mathbf{A}_e = [A_{e1} \quad A_{e2} \quad \cdots \quad A_{eM}]$, in which A_{em} is the area of m^{th} element, $m = 1, 2, ...M$ and $Q_{inj} = \int_{\partial A_p} Q ds$. Similarly, $\tilde{\mathbf{D}}_n (N-1)$ are the DDs obtained in the last time step or the initial fracture aperture for the first time step and $\mathbf{T}_R$ is the transformation matrix (of order $M \times TN$) applied to obtain values on element centers from element nodal values through interpolation. M is the total number of elements and TN is the total number of nodes used in discretization of fracture.

Similarly, the integral equations (in BEM) for stress and pore pressure in the reservoir rock can be formulated as in Section **3.1.1**. By applying the discretized equations for stress (Eq. 3.13) on element centers and equation for pore pressure (Eq. 3.14) collocated on all element nodes (at the same mesh in FEM), it yields following set of algebraic equations:

$$\boldsymbol{\sigma}_\mathbf{n} = \mathbf{A}_7 \tilde{\mathbf{D}}_n (\mathbf{t}) + \mathbf{A}_8 \tilde{\mathbf{D}}_F (\mathbf{t}) + \boldsymbol{\sigma}_{\mathbf{n1}} + \boldsymbol{\sigma}_{\mathbf{n0}} \quad \text{.....(3.88)}$$

$$\tilde{\mathbf{p}} = \mathbf{A}_{10} \tilde{\mathbf{D}}_n (\mathbf{t}) + \mathbf{A}_{11} \tilde{\mathbf{D}}_F (\mathbf{t}) + \mathbf{p}_1 + \mathbf{p}_0 \quad \text{.....(3.89)}$$

The matrices $(\mathbf{A}_7, \mathbf{A}_8, \mathbf{A}_{10}$ and $\mathbf{A}_{11})$ have been defined previously.

Equations representing coupled rock deformation and fracture flow (Eqs. 3.86 through 3.89) form solution system of the problem and are written in matrix form as:

$$\begin{bmatrix} \mathbf{A_1} & \mathbf{0} & \mathbf{A_2} & \mathbf{I}_0 \\ \mathbf{T}_R & -\mathbf{A_7} & -\mathbf{A_8} & \mathbf{T}_R\mathbf{I}_0 \\ \mathbf{I} & -\mathbf{A_{10}} & -\mathbf{A_{11}} & \mathbf{I}_0 \\ \mathbf{0} & \mathbf{A}_e & \Delta t\mathbf{A}_e\mathbf{T}_R & 0 \end{bmatrix} \begin{Bmatrix} \tilde{\mathbf{p}} \\ \tilde{\mathbf{D}}_n \\ \tilde{\mathbf{D}}_F \\ P \end{Bmatrix} = \begin{Bmatrix} \mathbf{B_1} \\ \boldsymbol{\sigma}_{\mathbf{n1}} + \boldsymbol{\sigma}_{\mathbf{n0}} \\ \mathbf{p_1} + \mathbf{p_0} \\ Q_{inj}\Delta t + \mathbf{A}_e\tilde{\mathbf{D}}_n\left(N-1\right) \end{Bmatrix} \quad \text{.....(3.90)}$$

Here, the fracture is "open" (allowing fluid flow) and this condition is written mathematically as: $\overset{m}{\sigma}_n - \overset{m}{\sigma}_{n0} = \overset{m}{p} - \overset{m}{\sigma}_{n0}$ $(m = 1, 2..., M)$ for each element (m) in the fracture plane. Similarly, $\mathbf{I}_0 = \begin{bmatrix} 1 & 1 & \cdots & 1 \end{bmatrix}^{\mathrm{T}}$ and $\mathbf{I}$ is a unit matrix (of order $TN \times TN$). The unknowns are fracture aperture ($\mathbf{w} = \tilde{\mathbf{D}}_n + \mathbf{w}_0$), fluid pressure $\left(\tilde{\mathbf{p}} + P\right)$ and leak-off velocity $\left(\tilde{\mathbf{D}}_F\right)$. These are solved at each time steps using "iterative" procedure, presented next.

3.3.2.1 Solution Procedure

The fluid pressure $\left(\tilde{\mathbf{p}}\right)$, fluid source intensity $\left(\tilde{\mathbf{D}}_F\right)$, displacement discontinuity $\left(\tilde{\mathbf{D}}_n\right)$ and global mass balance component of pressure $\left(P\right)$ are solved with simultaneously from solution system (Eq. 3.90). The fracture propagation is implemented using quasi-static technique. This is done by considering small fracture length at each time steps of total injection time subjected to injection pressure; satisfying global mass balance and advancing in time by using a fracture propagation criterion ($K_I = K_{IC}$). Once fracture equilibrium achieved at each time step, the fracture length is increased with small

amount and this procedure is repeated until total time exceeds pump time. Therefore, two levels of iteration are required in simulating hydraulic fracturing; inner iteration–for fluid pressure and fracture aperture and outer iteration– for tip pressure and time steps. Following steps are executed:

1. Start the simulation with trial values of fracture width, fracture geometry (length or radius) and time step.
2. Calculate coefficient matrices and vectors in Eq. 3.90 using trial values.
3. Solve for fluid pressure $\left(\tilde{\mathbf{p}}\right)$, fluid source intensity $\left(\tilde{\mathbf{D}}_F\right)$, and displacement discontinuity $\left(\tilde{\mathbf{D}}_n\right)$. Calculate fracture width $\mathbf{w} = \tilde{\mathbf{D}}_n + \mathbf{w}_0$.
4. Update matrix $\mathbf{A_1}$ and RHS of Eq. 3.90 (function of fracture width $\left(\mathbf{w}\right)$).
5. Iterate until convergence in $\mathbf{w}$ is achieved during $\tilde{\mathbf{p}}$ and $\mathbf{w}$ iteration loop.
6. Update time step with balancing tip pressure, using $K_I = K_{IC}$ criterion.
7. Iterate until convergence in time step $\left(\Delta t\right)$ is achieved in time loop.
8. Start from step 2 to advance in time; trial values are now replaced by latest values and fracture length is increased by small amount. Repeat the procedure until the total time exceeds pump time.

Furthermore, details on each of balancing tip pressure and time steps are presented later in this section.

3.3.2.2 Multiple Fracture Simulation

The solution technique for multiple fracture simulation is similar to that for single fracture case; however, the influence coefficients (for stress and pore pressure) of each fractures and their influence to other fractures in BEM have to be collected systematically to form global “stiffness matrix”. Similarly, the fluid flow equation has to be written for all fractures and fluid mass balance should be satisfied for each fracture.

For example, to distinguish the simulation of multiple fractures from the single fracture case, let us consider two planar fractures separated at a certain distance and are subjected to fluid injection. The solution systems representing unknown fluid pressure, fracture aperture, leak-off velocity with global mass balance for two fractures can be written in matrix form as:

$$\begin{bmatrix} \mathbf{A_1} & \mathbf{0} & \mathbf{A_2} & \mathbf{I}_0 & \mathbf{0} & \mathbf{0} & \mathbf{0} & \mathbf{0} \\ \mathbf{T} & -\mathbf{A_7} & -\mathbf{A_8} & \mathbf{TI}_0 & \mathbf{0} & \mathbf{A_7} & -\mathbf{A_8} & \mathbf{0} \\ \mathbf{I} & -\mathbf{A_{10}} & -\mathbf{A_{11}} & \mathbf{I}_0 & \mathbf{0} & -\mathbf{A_{10}} & \mathbf{A_{11}} & \mathbf{0} \\ \mathbf{0} & \mathbf{A}_e & \Delta t\mathbf{A}_e\mathbf{T} & 0 & \mathbf{0} & \mathbf{0} & \mathbf{0} & \mathbf{0} \\ \mathbf{0} & \mathbf{0} & \mathbf{0} & \mathbf{0} & \mathbf{A}_1 & \mathbf{0} & \mathbf{A}_2 & \mathbf{I}_0 \\ \mathbf{0} & -\mathbf{A_7} & -\mathbf{A_8} & \mathbf{TI}_0 & \mathbf{T} & -\mathbf{A_7} & -\mathbf{A_8} & \mathbf{TI}_0 \\ \mathbf{0} & -\mathbf{A_{10}} & -\mathbf{A_{11}} & \mathbf{I}_0 & \mathbf{I} & -\mathbf{A_{10}} & -\mathbf{A_{11}} & \mathbf{I}_0 \\ \mathbf{0} & \mathbf{0} & \mathbf{0} & \mathbf{0} & \mathbf{0} & \mathbf{A}_e & \Delta t\mathbf{A}_e\mathbf{T} & \mathbf{0} \end{bmatrix} \begin{Bmatrix} \tilde{\mathbf{p}} \\ \tilde{\mathbf{D}}_n \\ \tilde{\mathbf{D}}_F \\ P \\ \tilde{\mathbf{p}} \\ \tilde{\mathbf{D}}_n \\ \tilde{\mathbf{D}}_F \\ P \end{Bmatrix} = \begin{Bmatrix} \mathbf{B_1} \\ \boldsymbol{\sigma}_{\mathbf{n1}} + \boldsymbol{\sigma}_{\mathbf{n0}} \\ \mathbf{p_1} + \mathbf{p_0} \\ Q_{inj}\Delta t + \mathbf{A}_e\tilde{\mathbf{D}}_n\left(N-1\right) \\ \mathbf{B_1} \\ \boldsymbol{\sigma}_{\mathbf{n1}} + \boldsymbol{\sigma}_{\mathbf{n0}} \\ \mathbf{p_1} + \mathbf{p_0} \\ Q_{inj}\Delta t + \mathbf{A}_e\tilde{\mathbf{D}}_n\left(N-1\right) \end{Bmatrix} \quad ..(3.91)$$

On the left-hand side of Eq. 3.91, four sets of 4×4 block matrix can be observed because each fractures yield two such sets– representing the contribution of the fracture and its influence to other fracture when moving along row direction respectively. Therefore, a generalized form of global solution system to simulate multiple fractures can be summarized as:

$$\begin{bmatrix} \mathbf{T}^{(1)}(1) & \mathbf{T}^{(1)}(2) & ... & \mathbf{T}^{(1)}(N) \\ \mathbf{T}^{(2)}(1) & \mathbf{T}^{(2)}(2) & .... & \mathbf{T}^{(2)}(N) \\ .... & ... & ... & ... \\ \mathbf{T}^{(N)}(1) & \mathbf{T}^{(N)}(2) & ... & \mathbf{T}^{(N)}(N) \end{bmatrix} \begin{Bmatrix} \mathbf{X}(1) \\ \mathbf{X}(2) \\ ... \\ \mathbf{X}(N) \end{Bmatrix} = \begin{Bmatrix} \mathbf{RHS}^{(1)} \\ \mathbf{RHS}^{(2)} \\ .... \\ \mathbf{RHS}^{(N)} \end{Bmatrix} \text{.....(3.92)}$$

where,

$\mathbf{T}^{(i)}(j) =$ "Influence coefficient matrix" for fracture i due to the sources in fracture j or FEM "stiffness matrix" for fracture i

Similarly, components of FEM "stiffness matrix" and global mass balance in

$\mathbf{T}^{(i)}(j) = 0,\ for\ (i \neq j)$

$\mathbf{X}(\mathbf{i}) =$ Unknown vector = $\begin{Bmatrix} \tilde{\mathbf{p}} \\ \tilde{\mathbf{D}}_n \\ \tilde{\mathbf{D}}_F \\ P \end{Bmatrix}$ for fracture i

$\mathbf{RHS}^{(i)} =$ Load vector = $\begin{Bmatrix} \mathbf{B_1} \\ \boldsymbol{\sigma}_{\mathbf{n1}} + \boldsymbol{\sigma}_{\mathbf{n0}} \\ \mathbf{p_1} + \mathbf{p_0} \\ Q_{inj}\Delta t + \mathbf{A}_e \tilde{\mathbf{D}}_n (N-1) \end{Bmatrix}$ for fracture i

$N =$ Number of fractures

3.3.2.3 Implementation of Fracture Propagation

Stress intensity factor can be computed using the fracture aperture distribution including at the fracture tip using the linear fracture mechanics theory. For a penny shaped fracture, K_I is calculated as (Yew 1997):

$$K_I = \frac{G}{4(1-\nu)}\sqrt{\frac{2\pi}{r}}w(r) \quad \text{.....(3.93)}$$

in which w is fracture width and r is the inward normal distance from the fracture tip.

Following steps are carried out to balance the tip pressure.

1. Calculate K_{I1} using $P_1 = P_{tip}$ from the previous time step.
2. Calculate K_{I2} using $P_1 = \chi P_{tip}$ where $\chi < 1$ is a positive number (0.8 taken here, suggesting K_I is nearly linear function of P_{tip} for the problems solved in this dissertation).
3. Calculate $P_m = (P_2 - P_1)(K_{IC} - K_{I2}) / (K_{I2} - K_{I1})$.
4. Calculate K_{Im} using P_m and compare to tolerance.
5. If necessary, let $P_1 = P_2, P_2 = P_m$ and repeat 3 and 4.

Similarly, following steps are carried out to implement fracture propagation.

1. Iteratively find P_{tip} such that $K_I = K_{Ic}$ within the tolerance.
2. Revise Δt during each iteration for P_{tip} using Eq. 3.87 (see **Fig. 3.9**).

$$\Delta t = \frac{\mathbf{A}_e\tilde{\mathbf{D}}_n - \mathbf{A}_e\tilde{\mathbf{D}}_n(N-1)}{Q_{inj} - \mathbf{A}_e\mathbf{T}\tilde{\mathbf{D}}_F} \quad \text{.....(3.94)}$$

3. Check that Δt has changed between successive iterations by less than tolerance.
4. Use the iterative procedure in step 1 to calculate two more values of P_{tip}, K_I and Δt.
5. Check that K_I and Δt criteria as in steps 1 and 3 are satisfied. Return to step 4 as needed.

The above procedure requires 5-10 calculations of K_I for most problems. The schematic of iteration algorithm is shown in Fig. 3.9**.**

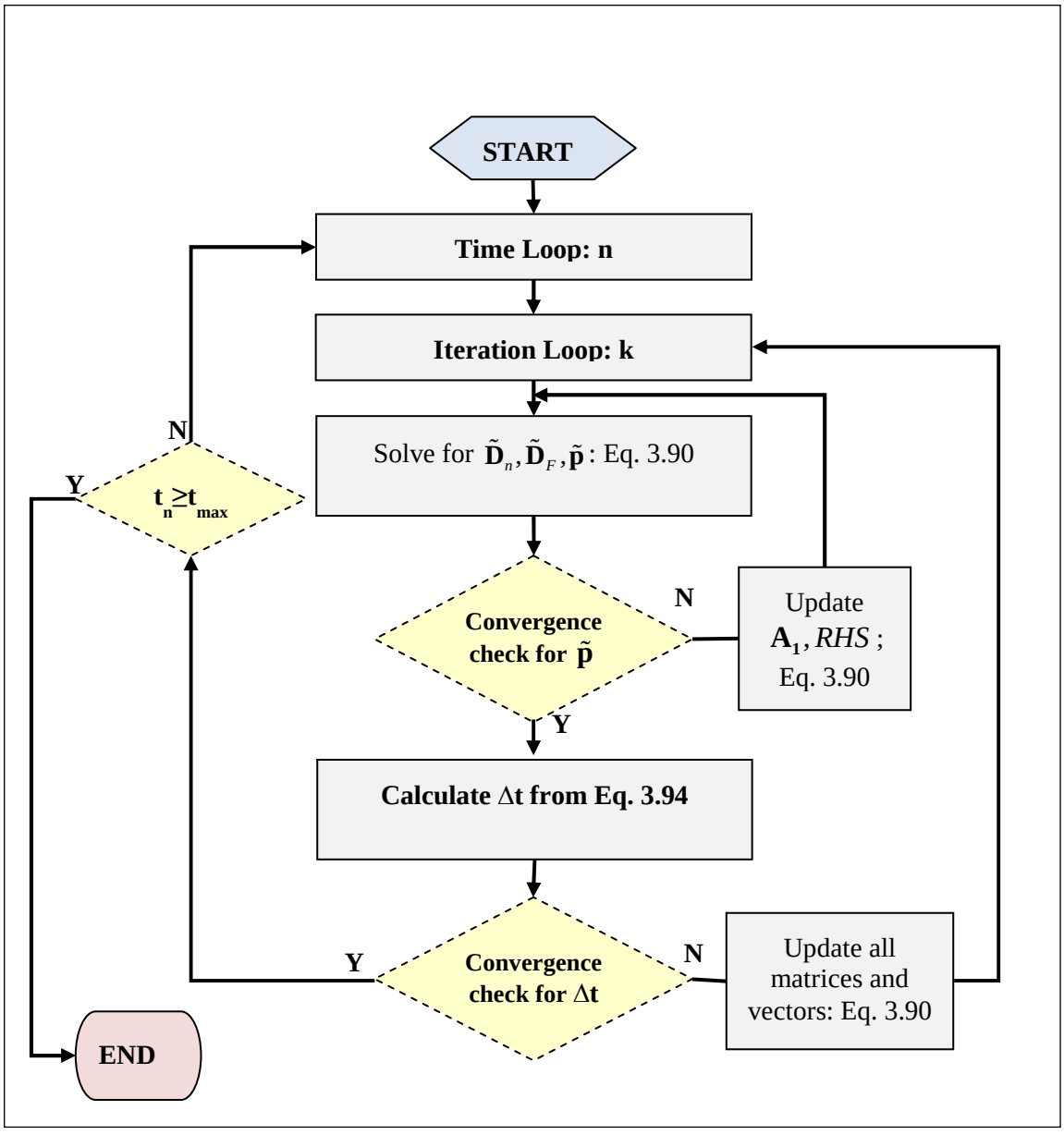

Fig. 3.9 Schematic of iteration algorithm for coupled fluid pressure and fracture aperture and fracture propagation.

3.3.3 Poroelastic Module for Reservoir Layer Deformation

In this approach, the Biot's poroelasticity model is applied in the reservoir using three-dimensional FEM. Early works of Sandhu and Wilson (1969) and later by others (Gambolati and Freeze 1973; Lewis et al. 1986; Lewis et al. 1991; Li and Zienkiewicz 1992; Sukirman and Lewis 1993; Lewis and Schrefler 1998; Zienkiewicz and Taylor 2000; Pao et al. 2001; Pao and Lewis 2002) are the foundation works in applications of finite element techniques in poroelasticity. As an extension, in this work, we consider the effect of stress redistributions in the overburden on the reservoir flow model, computed by using poroelastic Displacement Discontinuity Method (DDM). The benefits of this approach are: the direct savings in computational cost in large scale reservoir problems, otherwise whole domain would require spatial discretization scheme and secondly, realistic representation of the geomechanical reaction of the reservoir surroundings in the model.

The conventional Galerkin finite element method is considered to approximate governing poroelastic equations (Eqs. 2.14 and 2.15). The following approximations are used for the displacement and pore pressure fields:

$$\mathbf{u} = \mathbf{N}_u \tilde{\mathbf{u}}, \quad p = \mathbf{N}_p \tilde{\mathbf{p}} \qquad \text{.....(3.95)}$$

where $\mathbf{N}_u$ and $\mathbf{N}_p$ are the shape functions for the solid displacement and pore pressure, respectively. Similarly, $\tilde{\mathbf{u}}$ and $\tilde{\mathbf{p}}$ are the vectors of the nodal displacements and nodal pore pressure, respectively.

Substituting Eq. 3.95 into Eqs. 2.14 and 2.15, the discretized equations of poroelasticity in terms of pore pressure and displacement are obtained, which form the following solution system:

$$\mathbf{K}\tilde{\mathbf{u}} + \mathbf{C}\tilde{p} = \mathbf{f}^{u} \quad \text{……..……..(3.96)}$$

$$\mathbf{C}^{T}\dot{\tilde{\mathbf{u}}} + \mathbf{S}\dot{\tilde{\mathbf{p}}} + \mathbf{H}_{H}\tilde{\mathbf{p}} = \mathbf{f}^{p} \quad \text{……..……..(3.97)}$$

where dot $(\cdot)$ represents the time derivative; $\mathbf{f}^{u}$ and $\mathbf{f}^{p}$ are the vectors of nodal forces and fluid sources, respectively. Similarly, $\mathbf{K}, \mathbf{H}, \mathbf{S}$ and $\mathbf{C}$ are the elastic stiffness, flow stiffness, flow capacity and coupling matrices, respectively. These are computed explicitly from matrix/vector operation of solid and fluid properties.

$$\mathbf{K} = \int_{V} \mathbf{B}^{T}\mathbf{D}\mathbf{B}\, dV, \mathbf{C} = \int_{V} \mathbf{B}^{T}\alpha\mathbf{m}\mathbf{N}_{p}\, dV \quad \text{……..……..…….(3.98)}$$

$$\mathbf{S} = \int_{V} \mathbf{N}_{p}^{T}\beta\mathbf{N}_{p}\, dV, \mathbf{H} = \int_{V} \left(\nabla\mathbf{N}_{p}\right)^{T}\left(k/\mu\right)\left(\nabla\mathbf{N}_{p}\right) dV \quad \text{……..(3.99)}$$

To integrate Eq. 3.97 with respect to time, the generalized θ-method (Section **3.2**) is adopted. After applying it, the solution system takes the following form:

$$\begin{bmatrix} \mathbf{K} & \mathbf{C} \\ \mathbf{C}^{T} & -\left(\mathbf{S} + \theta\Delta t\mathbf{H}\right) \end{bmatrix} \begin{Bmatrix} \Delta\tilde{\mathbf{u}} \\ \Delta\tilde{\mathbf{p}} \end{Bmatrix} = \begin{Bmatrix} \Delta\mathbf{f}^{u} \\ \Delta t\mathbf{H}\tilde{\mathbf{p}}\left(t_{n-1}\right) + \Delta\mathbf{f}^{p} \end{Bmatrix} \quad \text{……...…...(3.100)}$$

where t_{n-1} and t_{n} denote the last step time and current time such that, $\Delta t = t_{n} - t_{n-1}$ and displacement and pore pressure varies linearly between the time steps. Therefore, the following expressions are utilized to compute the absolute values of displacement and pore pressure from their incremental form in Eq. 3.100:

$$\begin{Bmatrix} \tilde{\mathbf{u}} \\ \tilde{\mathbf{p}} \end{Bmatrix}_{t} = \begin{Bmatrix} \tilde{\mathbf{u}} \\ \tilde{\mathbf{p}} \end{Bmatrix}_{t_{n-1}} + \begin{Bmatrix} \Delta\tilde{\mathbf{u}} \\ \Delta\tilde{\mathbf{p}} \end{Bmatrix} \quad \text{……(3.101)}$$

3.3.3.1 Integration Scheme for Reservoir Layer-Surrounding Strata

In this procedure, information between the reservoir (FE model) and the surroundings (BE model) are exchanged “iteratively” and the continuity of reservoir displacement, fluid source and stress are provided. The finite element method considers the three-dimensional reservoir flow whereas the boundary element method represents the poroelastic response of the reservoir surroundings as described in Section **3.1.1.**

The information that the FEM provides are the deformation of the reservoir and fluid velocity which are then converted into a displacement discontinuity and fluid source intensity, respectively and are input to the BEM. The BEM provides stress state of the reservoir surroundings, which is then converted into overburden loads provided to the FEM model. The process of coupling between the reservoir model and the surrounding BEM model is repeated until convergence is achieved **(Fig. 3.10).** The iteration steps are summarized next.

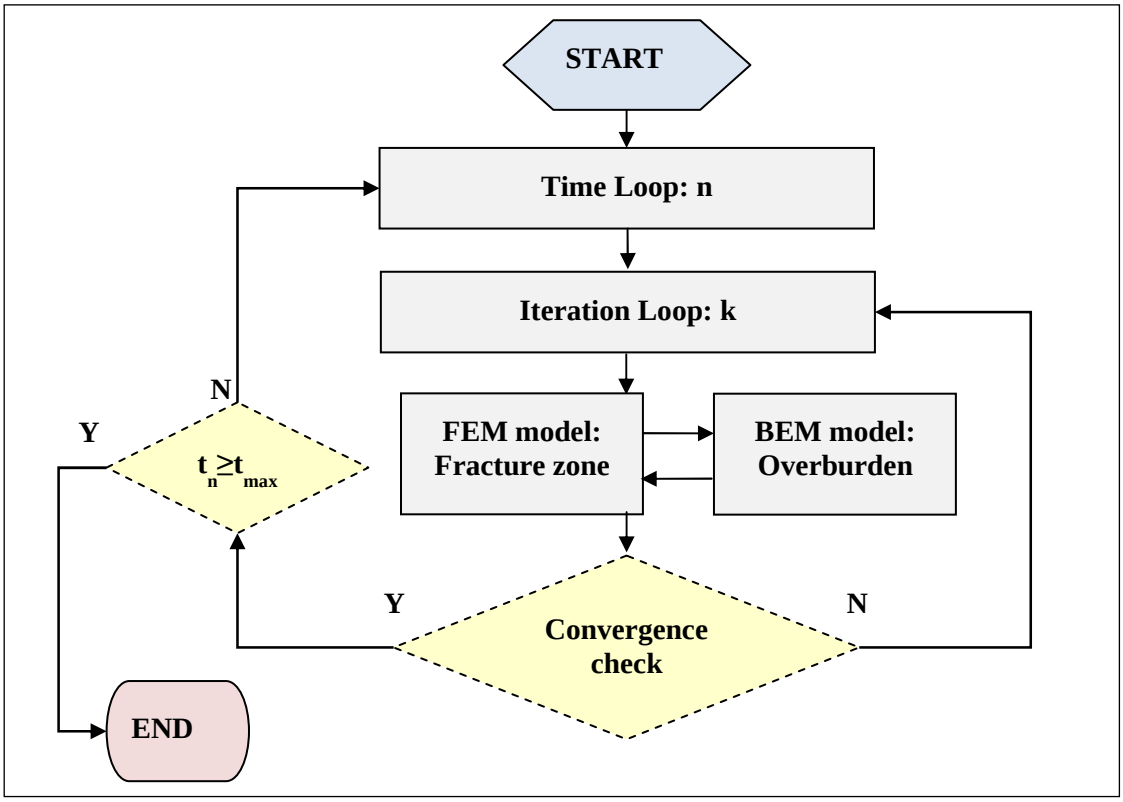

Fig. 3.10 Flowchart of the integration approach for reservoir layer-surrounding strata.

1. Run reservoir FEM model to compute displacement and pore pressure under prescribed external loads and boundary conditions within a specified time period. Calculate fluid velocity with known pore pressure in the reservoir.
2. Convert displacements and fluid velocity obtained from the FEM model to the displacement discontinuity and fluid source intensity, respectively, which are needed to apply to the BEM elements defining overburden.
3. Run the BEM model; compute local stress state of the overburden.

4. Apply the induced stresses calculated from the BEM model, along with the difference between the stresses in FEM and BEM, into the external loadings to be applied to the FEM model in the next iteration. This will retain the stresses continuity.

$$f^{k+1} = f^{k} + \chi\left(\sigma_{33}^{k} - \sigma_{z}^{k}\right) \text{……..…….(3.102)}$$

χ is the stress multiplier used to accelerate the convergence, given as:

$$\chi = \frac{E_{res}}{E_{res} + E_{overburden}} \text{ ……....(3.103)}$$

where E_{res} and $E_{overburden}$ represent the elastic modulus of the reservoir and overburden, respectively.

4. MODEL VERIFICATION

In this section, the numerical methods (BEM and FEM) incorporated to formulate hybrid BEFEM model as described in the previous chapter will be verified. A uniformly pressurized fracture is simulated using BEM to verify the numerical results with the known analytical solutions, while classical 1D consolidation and Mandel's experiments simulated to test FEM results against the closed-form solutions.

4.1 Pressurized Penny Shaped Fracture

We solve a penny shaped crack problem to verify the accuracy of the boundary element method used in our hybrid model. The analytical solutions for the fracture aperture and the normal stresses perpendicular to the fracture plane subjected to uniform normal tractions are known (Sneddon 1946; Edwards and Chicago 1951) and can be written as:

$$w(r)=\frac{4(1-v)\,pa}{\pi G}\sqrt{1-(r/a)^2} \qquad r/a<1 \qquad \text{(4.1)}$$

$$\sigma_{zz}(r)=\begin{cases} p & r/a<1 \\ -\dfrac{2p}{\pi}\left(\sin^{-1}\dfrac{a}{r}-\dfrac{a}{\sqrt{r^2-a^2}}\right) & r/a>1 \end{cases} \qquad \text{(4.2)}$$

where a is the radius of the fracture, r is the distance from the computational point to the fracture center, G is the shear modulus, v is the Poisson's ratio and p is the uniform normal pressure acting on the fracture surface.

Fig. 4.1 and **Fig. 4.2** show the comparisons between numerical and analytical results for the fracture opening and vertical normal stress, respectively. The numerical results agree well with the analytical results. The error of the numerical results near the fracture tips increase due to the use of constant elements instead of “tip elements”.

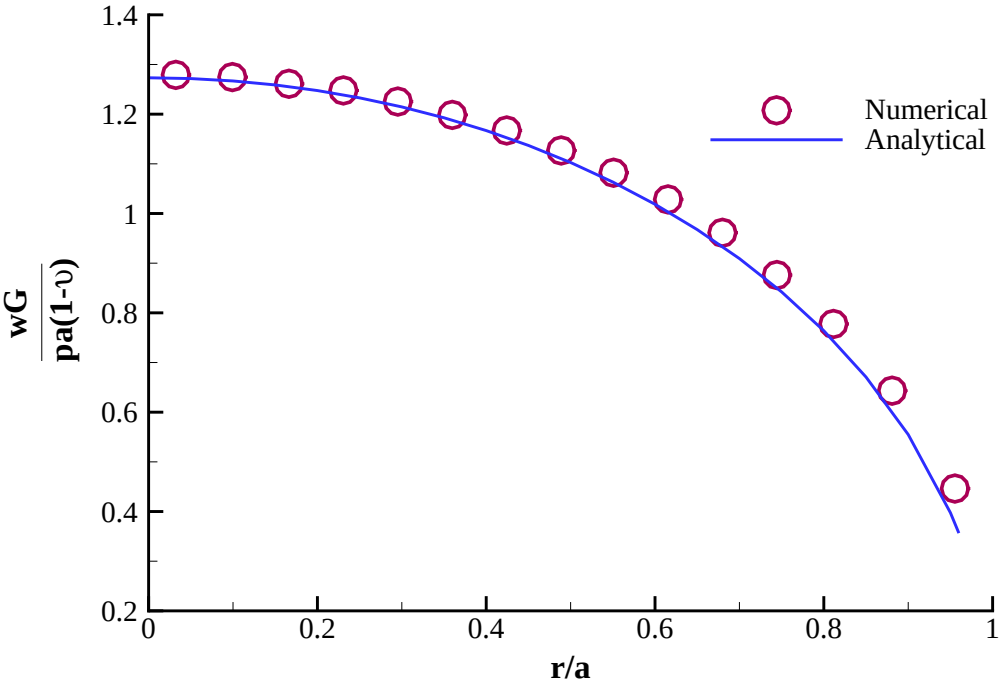

Fig. 4.1 Normalized fracture width.

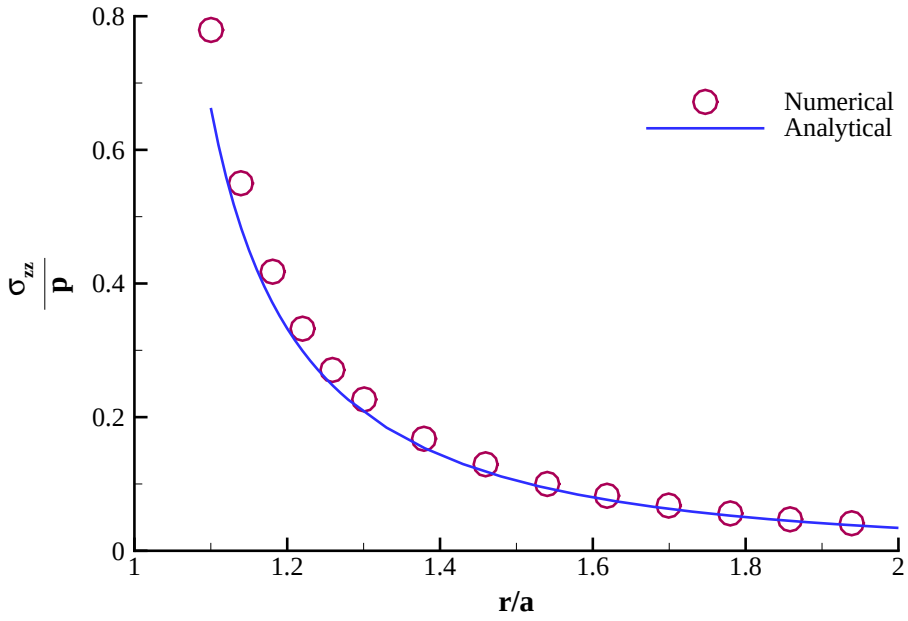

Fig. 4.2 Normalized stress.

4.2 One-Dimensional Consolidation

This section describes the verification of FEM results with Terzaghi's classical consolidation test (Terzaghi 1923; Biot 1941). In this experiment, a constant load is applied suddenly on the top surface of a fluid-saturated sample. The piston applying the load is permeable such that top boundary surface is drained. After an initial displacement, the sample gradually consolidates as fluid flows out of the top drain. The simulation results from our model will be compared to analytical solutions given by Biot (Biot 1941).

To consider a one-dimensional consolidation problem **(Fig. 4.3),** the domain is discretized using 20-node isoparametric brick elements with 16 elements and 141 nodes.

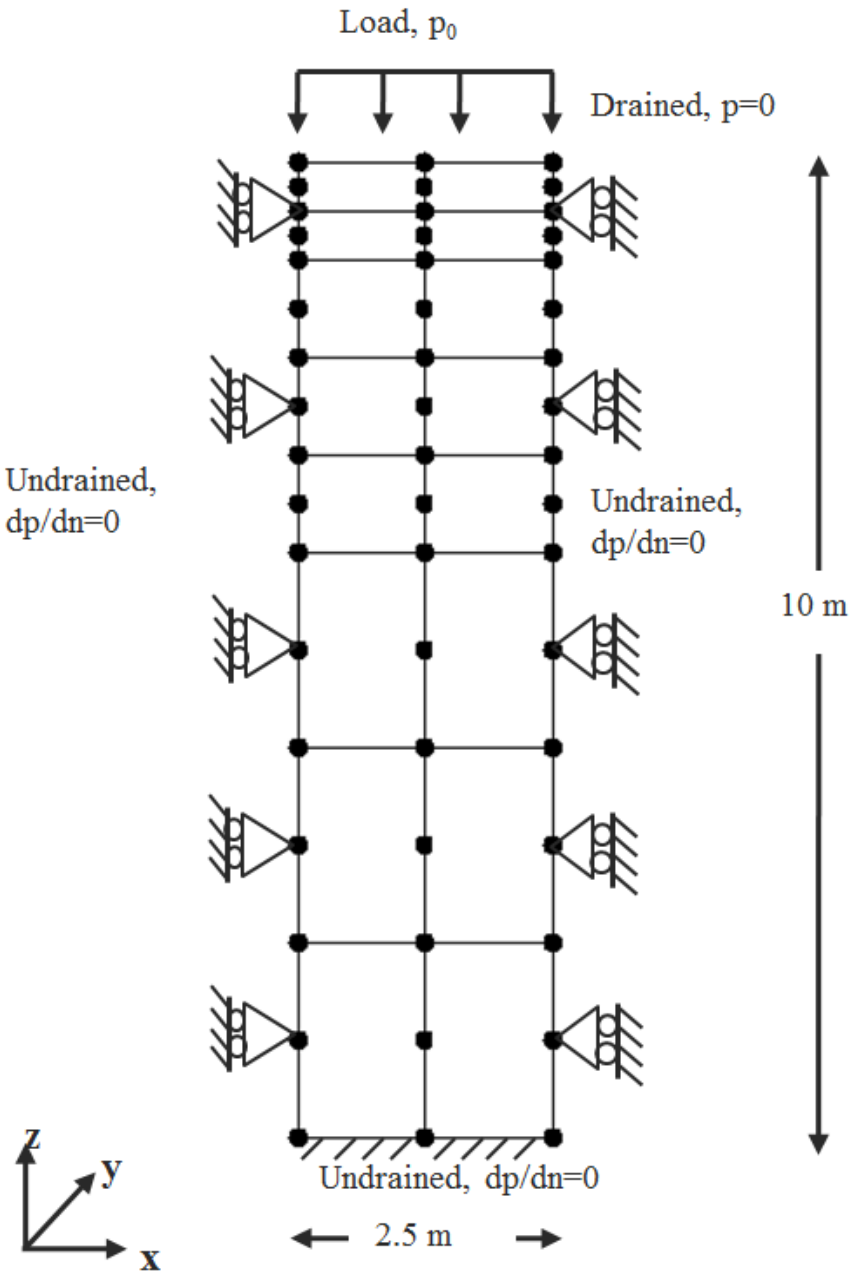

Fig. 4.3 One-dimensional consolidation problem.

The material properties used in this example are given in **Table 4.1.**

Table 4.1 Input data considered for one-dimensional consolidation

Parameter	Value	Units
Young's modulus, E	1.0×10^{6}	Pa
Poisson's ratio, υ	0.2	-
Biot's modulus, M	1.0×10^{9}	Pa
Biot's coefficient, α	1.0	-
Permeability, k	100.0	md
Load, p_0	1.0×10^{6}	Pa

Boundary and initial conditions used to numerically simulate the consolidation experiment are as follows: an external surface load of $p_0 = 1.0$ MPa was applied at the top surface of the model where the fluid is allowed to drain and no-lateral-strain is imposed on horizontal displacements.

FEM results (in symbols) for pore pressure and closed-form poroelastic solutions (Biot 1941) (in solid lines) are compared in **Fig. 4.4.** It depicts the evolution of pore pressure in the fluid-saturated sample due to compaction of pore space and the attenuation in pore pressure profiles with time as the fluid escapes from the top of sample subjected to constant load.

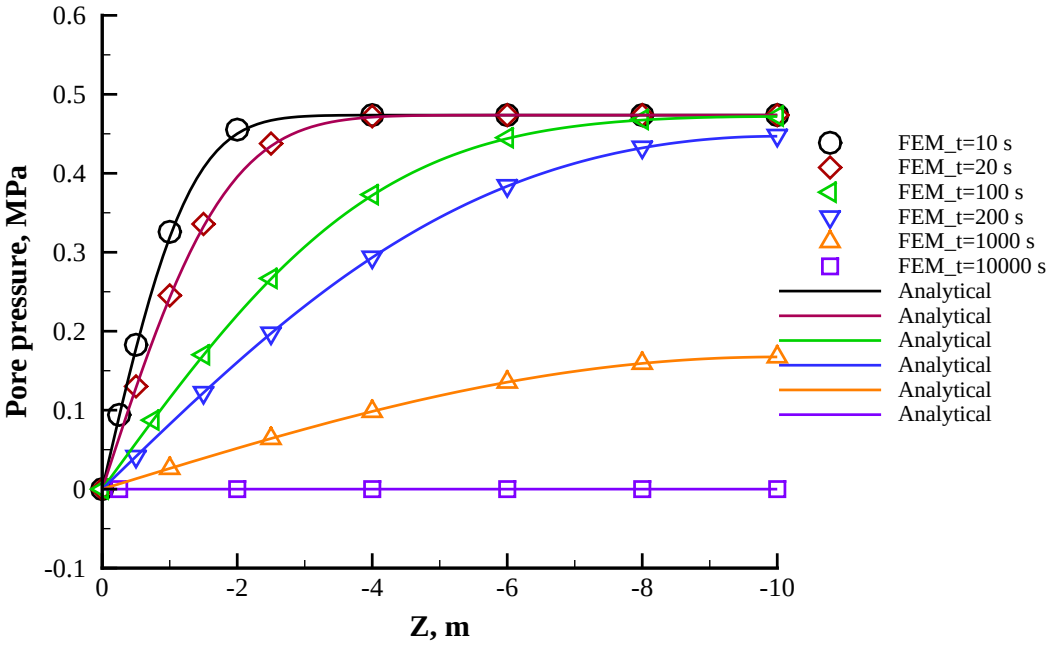

Fig. 4.4 Pore pressure profiles at different times.

Similarly, simulation results from FEM (in symbols) for displacement and closed-form poroelastic solutions (Biot 1941) (in solid lines) are compared in **Fig. 4.5.** The displacement profiles show the prolonged subsidence at the top of sample due to simultaneous fluid drainage and constant mechanical loading. In both the comparisons, our model results match excellent with the analytical solutions.

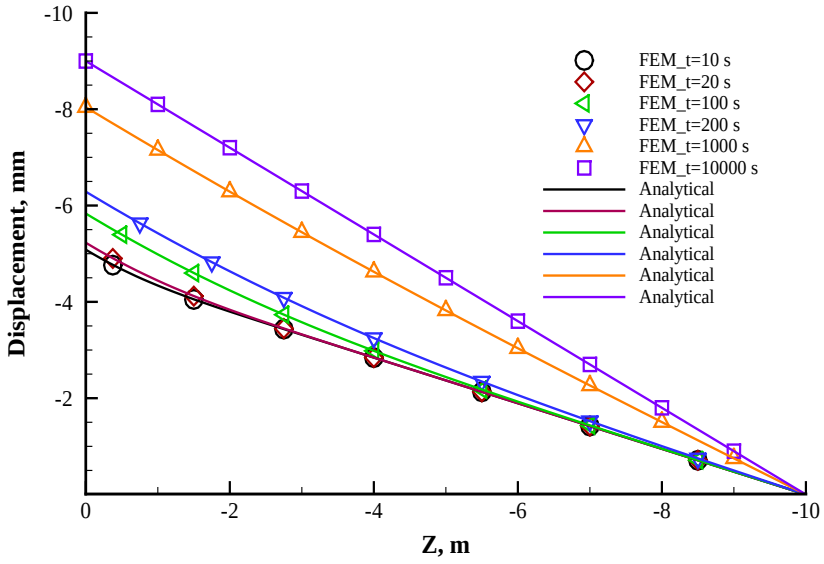

Fig. 4.5 Displacement profile at different times.

4.3 Mandel's Problem

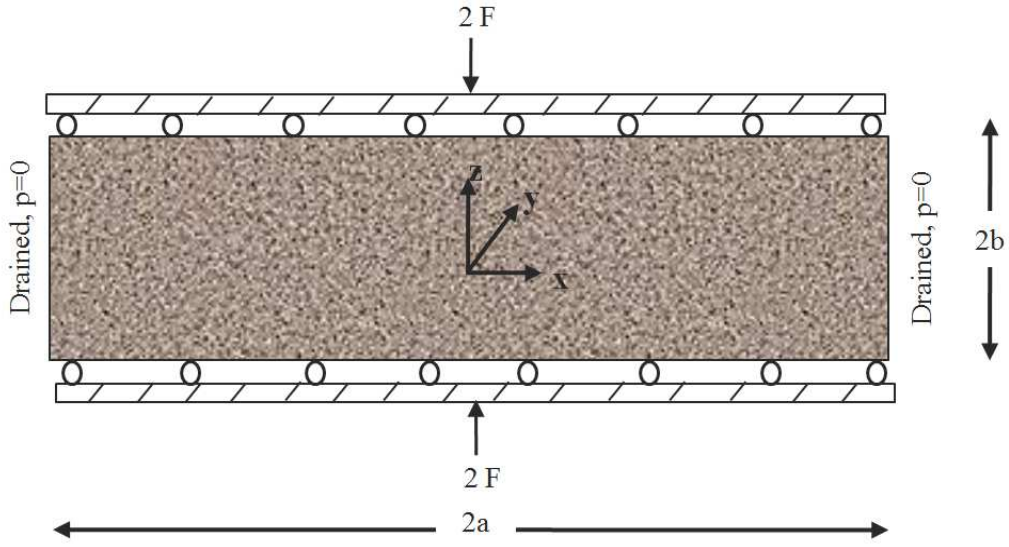

Fig. 4.6 Mandel's problem geometry.

In this section, a popular benchmark problem for testing the validity of numerical codes in poroelasticity–Mandel's problem (Mandel 1953) is solved to confirm the results from our FEM model. Mandel's problem involves an infinitely long rectangular specimen sandwiched at the top and the bottom by two rigid frictionless and impermeable plates. The lateral sides are free from normal and shear stress, and pore pressure (See **Fig. 4.6**).

To solve the Mandel's problem, we set the dimension of the specimen and the material properties as given in **Table 4.2.**

Table 4.2 Input data considered for Mandel's problem

Parameter	Value	Units
Young's modulus, E	1.0×10^{8}	Pa
Drained Poisson's ratio, v	0.2	-
Undrained Poisson's ratio, v_u	0.5	-
Fluid viscosity, μ	1.0×10^{-3}	Pa-s
Biot's coefficient, α	1.0	-
Reservoir permeability, k	100.0	md
Force, F	1.0×10^{8}	N/m
a	100.0	m
b	10.0	m

In this experiment, at $t = 0^+$, a force of $2F$ per unit thickness of the fluid-saturated specimen is applied at the top and bottom. A uniform pressure rise will be generated inside the specimen as predicted by the Skempton effect (Skempton 1954). However, with time, pore pressure near the side boundaries will dissipate due to the drainage and later, the pressure depletion region will propagate into the center of the specimen. Finally, the fluid drainage will ceased after the initial pressure rise totally vanishes over the entire specimen. The analytical solutions for the pore pressure and displacements can be found in (Mandel 1953; Cheng and Detournay 1988; Abousleiman et al. 1996):

$$p = \frac{2FB(1+\nu_u)}{3a}\sum_{i=1}^{\infty}\frac{\sin\beta_i}{\beta_i - \sin\beta_i\cos\beta_i}\left(\cos\frac{\beta_i}{a} - \cos\beta_i\right)\exp\left(-\frac{\beta_i^2 c_t}{a^2}\right) \quad \text{.....(4.3)}$$

$$u_x = \left[\frac{F\nu}{2Ga} - \frac{F\nu_u}{Ga}\sum_{i=1}^{\infty}\frac{\sin\beta_i\cos\beta_i}{\beta_i - \sin\beta_i\cos\beta_i}\exp\left(-\frac{\beta_i^2 c_t}{a^2}\right)\right]x + \frac{F}{G}\sum_{i=1}^{\infty}\frac{\cos\beta_i}{\beta_i - \sin\beta_i\cos\beta_i}\sin\frac{\beta_i x}{a}\exp\left(-\frac{\beta_i^2 c_t}{a^2}\right) \quad \text{.....(4.4)}$$

where β_i satisfies

$$\tan\beta_i = \frac{1-\nu}{\nu_u - \nu}\beta_i \quad \text{.....(4.5)}$$

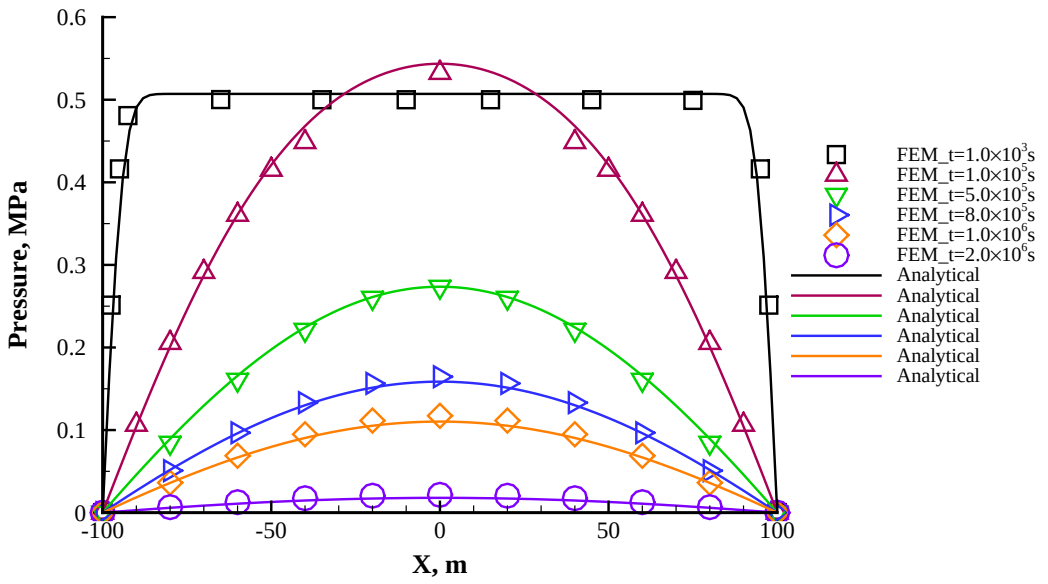

Fig. 4.7 Pore pressure profile at different times; comparison of the FEM and the analytical results.

The profiles of pore pressure across specimen computed from FEM model and analytical solutions are compared in **Fig. 4.7.** A non-monotonic (first rising, then falling) pore pressure reaction known as the Mandel-Cryer effect (Cryer 1963) can be observed at the center of the strip. It is because apparent compressive stiffness of the specimen is increased due to the initial presence of the pore pressure and the specimen become more compliant at the lateral sides with reduction pore pressure. By the compatibility requirement, a load transfer of compressive total stress towards the effectively stiffer (as-yet undrained) center region exist, which generates the pore pressure such that the pressure in the center region continues to rise after its initial creation (Abousleiman et al.

1996). As stated, this is a strain and stiffness effect, and can only be addressed by methods that afford correct coupling of displacements and pressures. Also a good agreement between FEM and analytical results can be observed for the horizontal displacements across the specimen, shown in **Fig. 4.8.** The faithful replication by our FEM model is the purpose of this demonstration.

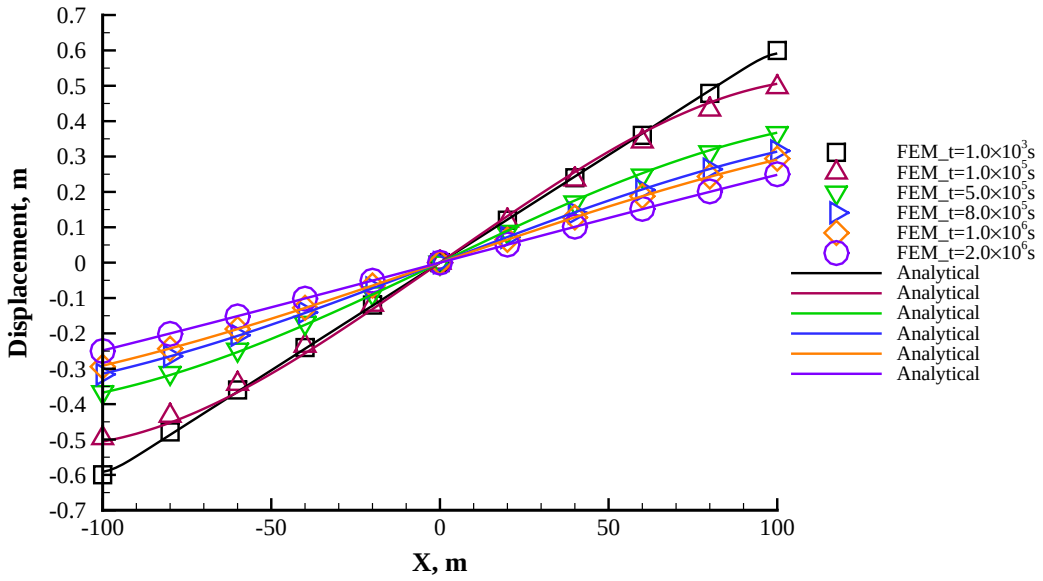

Fig. 4.8 Horizontal displacement at different times; comparison of the FEM and the analytical results.

5. NUMERICAL EXPERIMENTS

In this section, we demonstrate the application of hybrid BEFEM model to the example problems involving coupled thermo-poro-mechanical and chemical processes. The problems analyzed here are fluid injection and extraction into natural fracture in geothermal reservoir, hydraulic fracturing including multiple fractures in horizontal well and reservoir deformation due to fluid injection and production.

5.1 Cold Water Injection into a Fracture in Geothermal Reservoir

In this numerical experiment, fluid injection and extraction procedure in geothermal reservoir is simulated using the hybrid BEFEM model. The thermo-poroelastic-chemo module is applied to investigate the evolution of temperature, pressure, stress, fracture aperture and mineral dissolution associated with cold water injection for heat extraction in a natural fracture and their combined effects on heat energy production.

We consider a circular fracture of radius = 100 m at a depth of 2330 m contained in an enhanced geothermal reservoir with in-situ stresses of $\sigma_v = 60.13$ MPa , $\sigma_{H\min} = 34.81$ MPa , $\sigma_{H\max} = 50.88$ MPa and pore pressure of $p = 17.4$ MPa . The fracture is assumed to be horizontal so there is no fracture surface shear slip during the fluid injection and extraction process. An injection well is located at (-50, 0) and extraction well is at (50, 0) with respect to Cartesian coordinate system. Geothermal fluid is injected at temperature of 300 K and with a flow rate of 0.005 m^3/s while hot

water is produced at a constant bottomhole pressure of 17.4 MPa (same as the in-situ pore pressure) and this procedure is continued for 1 year.

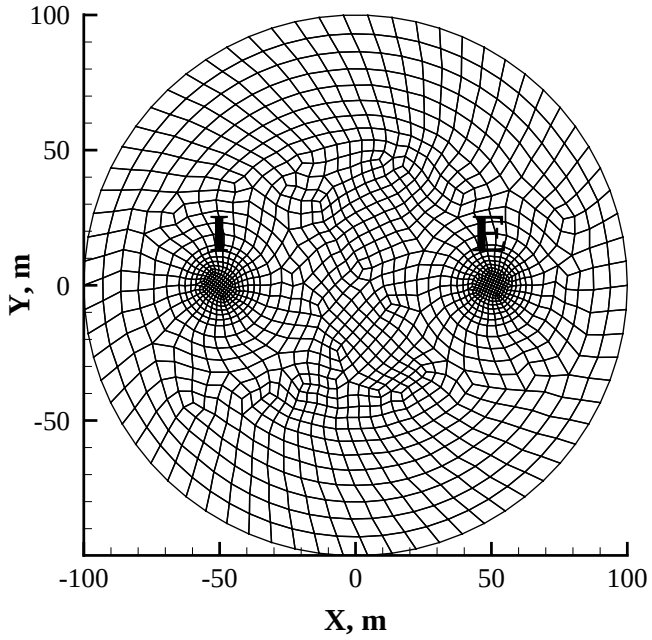

Fig. 5.1 Fracture surface discretization: the injection well is at "I" (-50, 0) and the extraction well is at "E" (50, 0).

To solve the problem, the fracture zone is divided into 1544 four-node quadrilateral elements; the fracture mesh is shown in **Fig. 5.1.** The input parameters are given in **Table 5.1**. First, we consider injection of undersaturated and cold water which is then extracted upon heating and analyze the impact of silica dissolution/precipitation and thermo-poroelasticity on fracture aperture evolution.

Table 5.1 Input data considered for injection and extraction case

Parameter	Value	Units
Fluid injection rate, Q	0.005	m^3/s
Initial average fracture aperture, w_o	50×10^{-6}	m
Shear modulus, G	7.0	GPa
Porosity,ϕ	0.2	-
Rock permeability, k	1.0	md
Poisson's ratio, υ	0.20	-
Fluid viscosity, μ	0.001	Pa-s
Fluid diffusivity, C^F	10^{-4}	m^2/s
Biot's Coefficient, α	0.74	-
Fluid density, ρ_F	1000	Kg/ m^3
Rock density, ρ_R	2300	Kg/ m^3
Fluid heat capacity, c_F	4200	J/Kg.K
Rock heat capacity, c_R	1000	J/Kg.K
Rock thermal conductivity, K_R	2.4	W/m·K
Rock linear thermal expansion coefficient, α_T	1.15×10^{-6}	1/K
Injection fluid temperature, T_i	300	K
Initial rock temperature, T_o	500	K
Joint normal stiffness, K_n	3×10^{11}	Pa/m
Solute diffusivity, c^S	5.0×10^{-7}	m^2/s
Mineral fraction in the reservoir, f_Q	0.3	-
Density of the mineral, ρ_Q	2650	Kg/ m^3

5.1.1 Silica Dissolution and Precipitation

Silica dissolution or precipitation occurs when the injectate is either under- or super-saturated, respectively. The amount of mass transfer is governed by the kinetics of the reaction. In this example, the undersaturated water has a silica concentration of 50 ppm while the reservoir matrix is at an initial equilibrium state with ~335 ppm. **Fig. 5.2** shows the distribution of the silica concentration in the fracture for injection times of 5 days and 1 year, respectively.

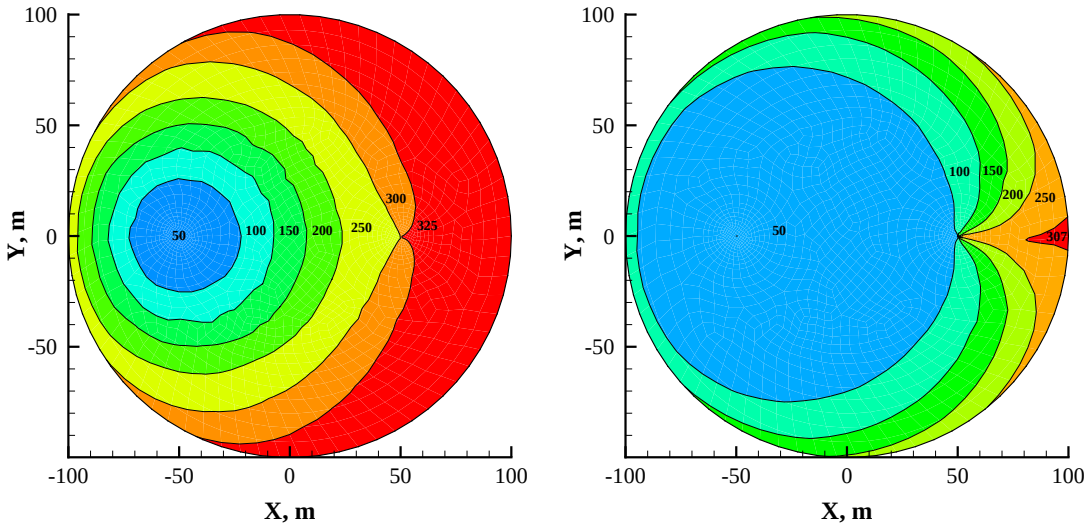

Fig. 5.2 Silica concentration (ppm) in the fracture at (a) 5 days and (b) 1 year: undersaturated case.

It is observed that silica concentration increases in the fracture as the fluid moves away from the injection well and silica is removed from then the reservoir matrix. As

time increases, the low concentration region originating from injection well extended towards extraction well; this is because the silica reactivity (function of temperature) with the fluid is reduced as the rock is cooled. Accordingly, the silica concentration in the extraction well follows a declining trend.

As the undersaturated injectate interacts with the rock, two factors control the mineral dissolution from the rock, the concentration gradient between the fluid and the matrix and the temperature dependent reaction rate. Therefore, for a given concentration gradient, the fracture aperture increase is higher in areas of higher temperature as shown in **Figs. 5.3a and 5.3b.**

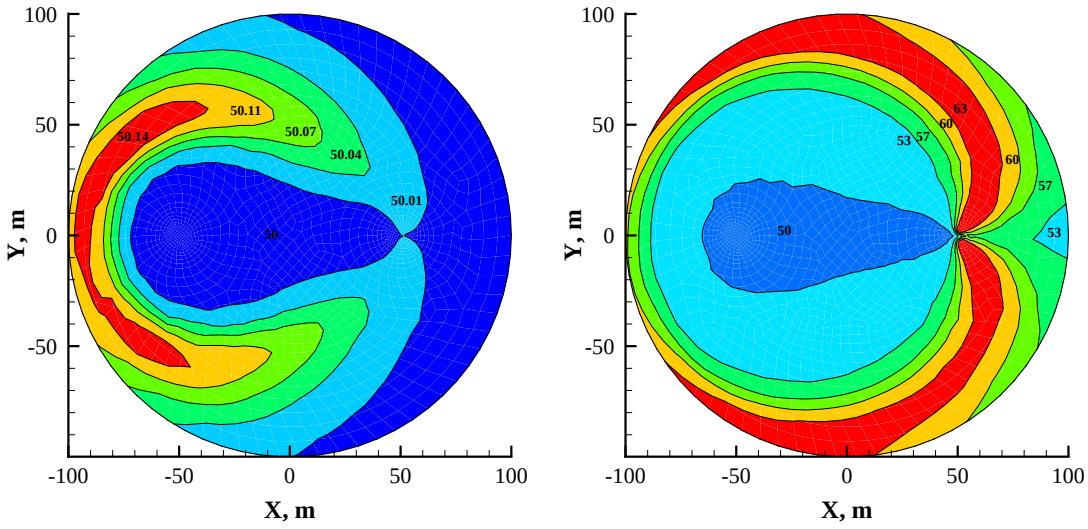

Fig. 5.3 Fracture aperture (μm) due to silica dissolution at (a) 5 days and (b) 1 year: undersaturated case.

As a result, the aperture change is non-uniform with bands of higher fracture aperture behind the injection well. The central cool zone does not show much reaction-induced aperture increase. With continues injection, the zone of maximum aperture moves away to a band extending from near the extraction well to the exterior parts of the fracture and behind the injection well. For one year of injection, the maximum increment in fracture aperture is 13 μm (Fig. 5.3b).

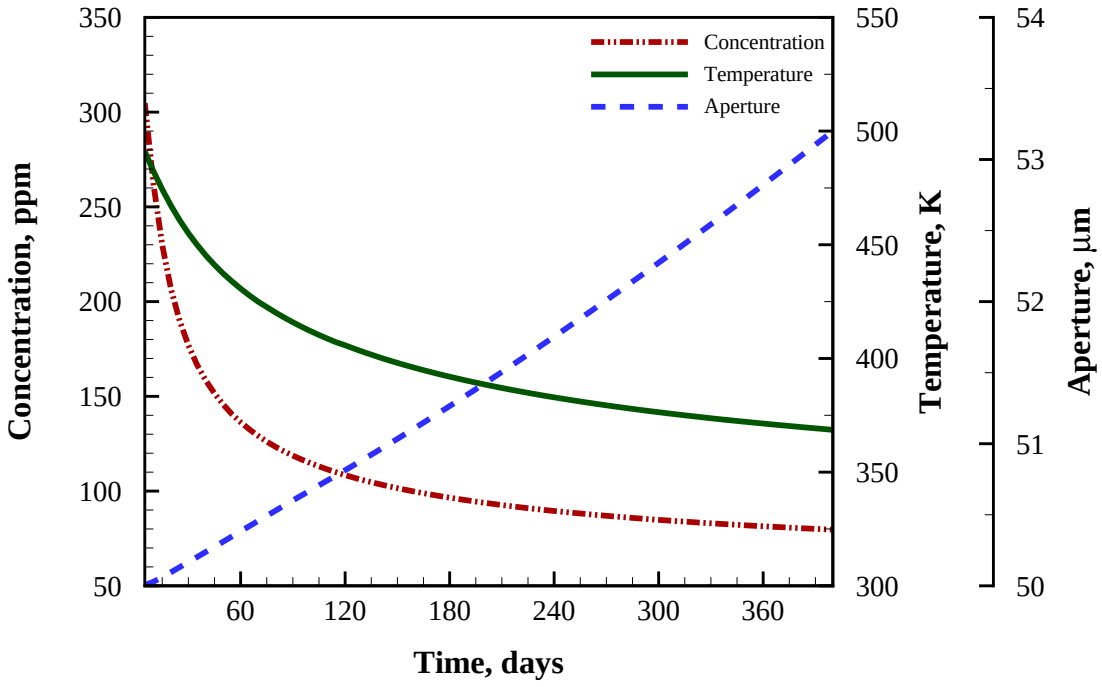

Fig. 5.4 Silica concentration (left axis), fluid temperature (inside right axis) and fracture aperture due to only silica dissolution (outside right axis) at the extraction well.

The silica concentration at the extraction well decreases as the undersaturated water injection continues and the injectate reacts with the hot silica-rich rock. This leads to an increment of fracture aperture change (although at a smaller magnitude). The profiles of fracture aperture due to silica dissolution, fluid concentration and temperature near at the extraction well are depicted in **Fig. 5.4**. The rate of silica dissolution with respect to time is constant at late times when the perturbations in temperature and concentration have also stabilized to a constant value.

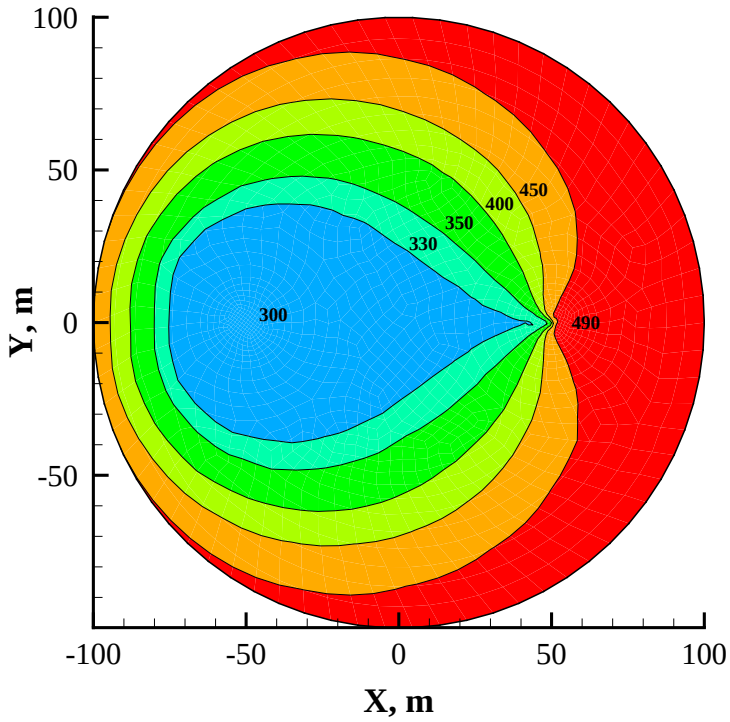

Fig. 5.5 Distributions of temperature (K) in the fracture after 1 year of operation.

The distribution of temperature in the fracture for 1 year of injection time is presented in **Fig. 5.5.** The cooled region exists between the injection and extraction well. As fluid injection into the fracture continues, this cooler region expands further and moves toward the extraction well, thus the extraction well temperature has a decreasing trend, as depicted in typical decline curve (see Fig. 5.4). The relatively small fracture and the close proximity of the wells (for the given injection rate) is responsible for a rather fast temperature decline at the outlet.

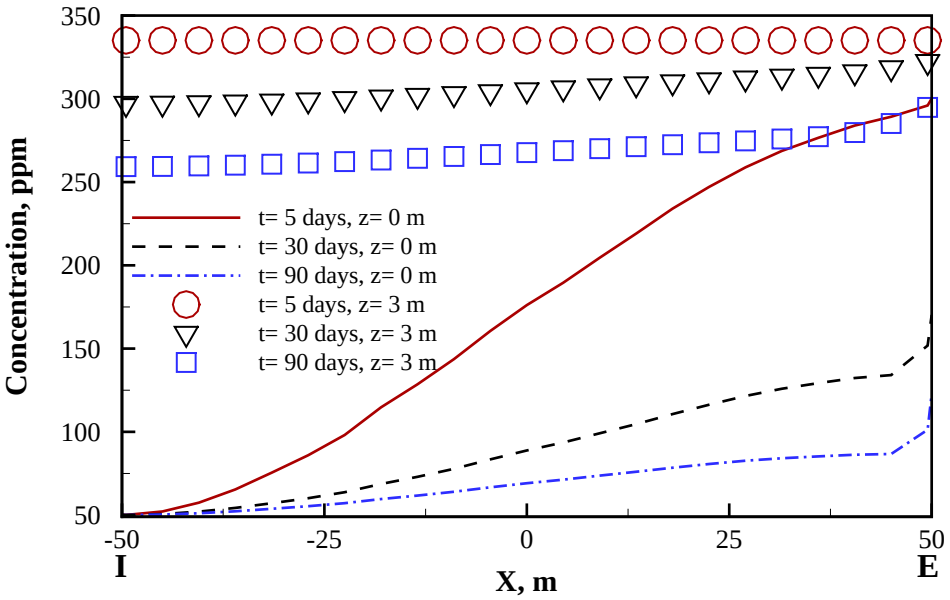

Fig. 5.6 Concentration in the fracture (z = 0) and in the rock-matrix (at z = 3m) along I-E after injection times of 5, 30 and 90 days. As expected, the concentration in the rock matrix decreases with mass transfer into the fracture.

The concentration profiles after 5, 30 and 90 days along two horizontal lines $(z = 0 \text{ m and } z = 3 \text{ m})$ parallel to the line I-E joining the two wells are shown in **Fig. 5.6**. At early times, the fluid has a higher silica concentration at the extraction well as the cool water has not reached it yet. At a distance of 3 m into the rock matrix, the silica concentration is at equilibrium value (335 ppm) at an early time of 5 days. The region of lowered concentration has extended just 3 m in the rock-matrix due to the fairly lower rate of solute diffusion coefficient (10^{-7} m^2/s).

Next, we consider the injection of supersaturated (silica concentration of 1000 ppm) cold water in the fracture in a reservoir matrix with an initial equilibrium state of ~335 ppm silica. The results are presented in **Fig. 5.7 and Fig. 5.8**. As time increases, higher concentration in the fracture extends towards the extraction well and silica precipitates from the saturated fluid as injection of supersaturated silica-rich water continues. The precipitation of silica in the fracture decreases the fracture aperture; it is more pronounced in areas of higher temperature (and thus reaction rate constant) and concentration gradient (Fig. 5.7) between rock and fluid. Therefore, the aperture change is non-uniform with bands of lower aperture behind the extraction well; the central cool zone has less silica precipitation because of slower silica reactivity at lower temperature. However, a significant amount (70%) of fracture width reduction due to silica precipitation is observed after 1 year of injection; the fracture aperture behind the extraction well is reduced to 16 μm (Fig. 5.8b).

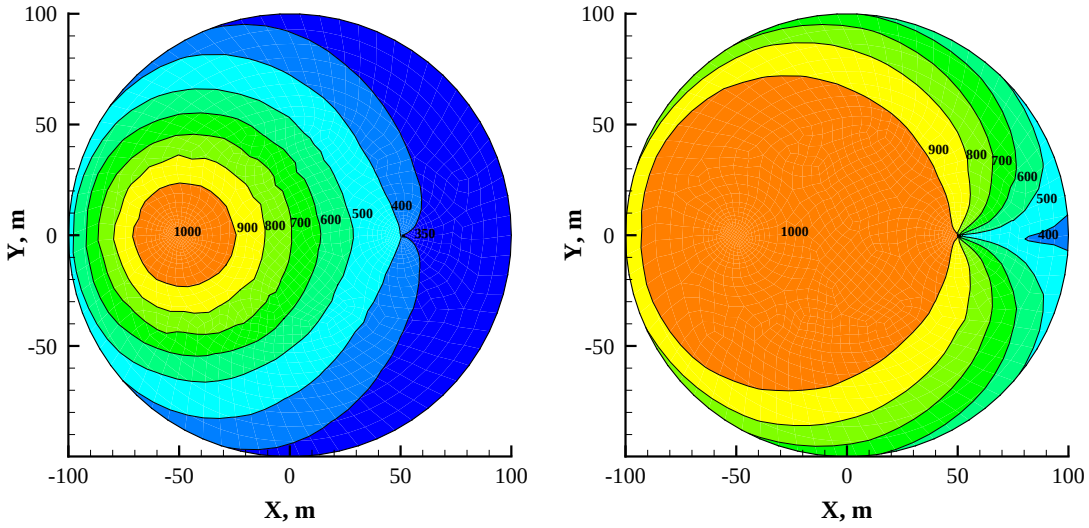

Fig. 5.7 Silica concentration (ppm) in the fracture at (a) 5 days and (b) 1 year: supersaturated case.

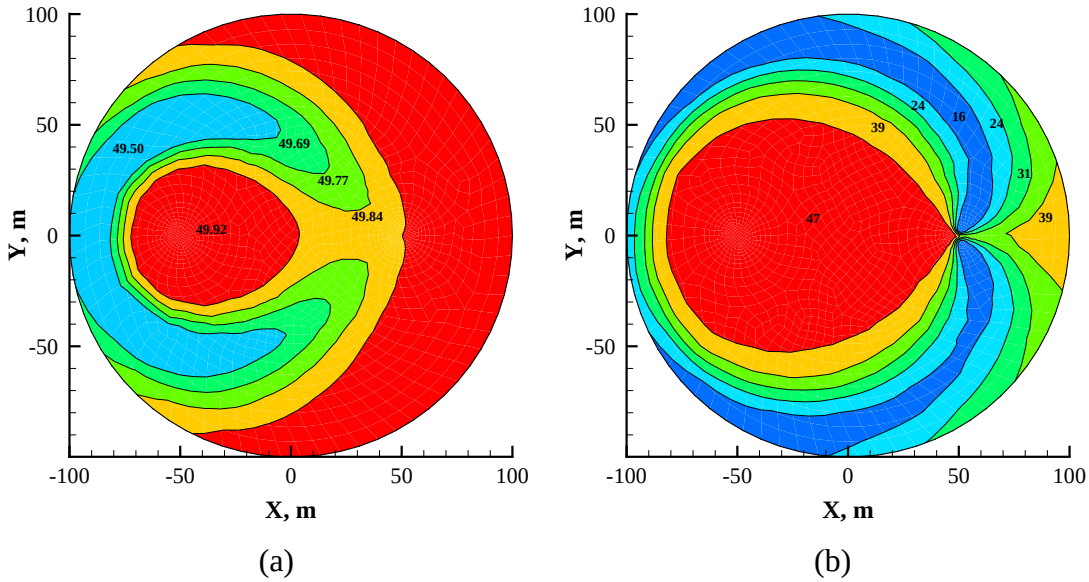

Fig. 5.8 Fracture aperture (μm) due to silica precipitation at (a) 5 days and (b) 1 year: supersaturated case.

5.1.2 Effect of Fluid Pressure and Stress Change on the Fracture Aperture

Fluid injection increases the pore pressure in the reservoir, in this example, the fluid pressure at the injection well is 20 MPa higher than at its value at the extraction well after 1 year as shown in **Fig. 5.9a**. The fact that some fluid is removed from the rock at the extraction well, the nearby pore pressure is about 35 MPa.

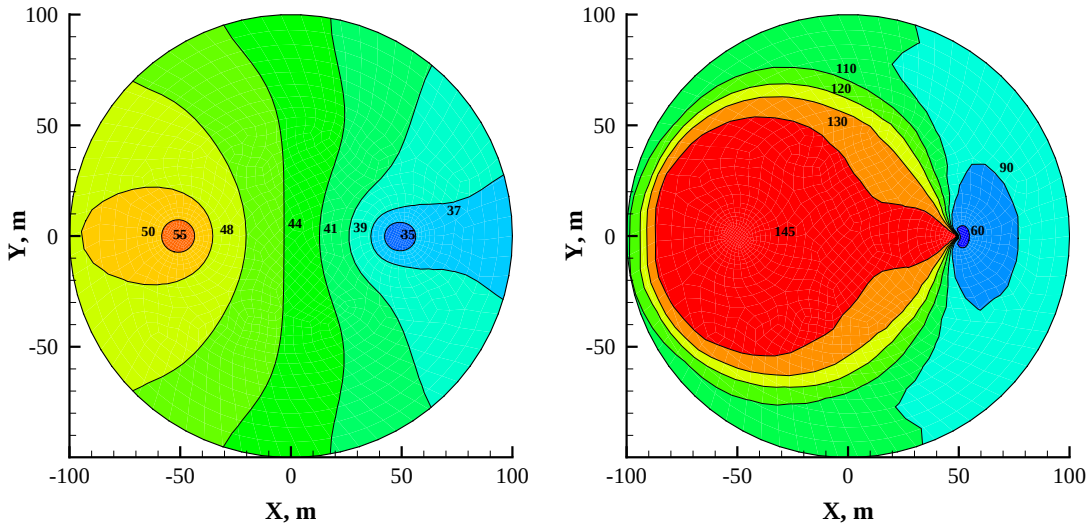

(a) (b)

Fig. 5.9 Distributions of (a) pressure (MPa) in the fracture and (b) fracture aperture (μm) due to combined thermo-poroelastic effects: after 1 year of fluid injection.

Fig. 5.9b shows the distribution of fracture aperture at 1 year. The increased fracture aperture shown in this figure is due to the combined influence of stresses related to fluid leak-off and cooling at fracture (excludes chemistry). It is observed that the

fracture aperture near the injection well is larger than elsewhere (almost three times of the initial 50 μm). This is because of the dominance of fluid pressure and thermal stress, both of which increase the fracture aperture. Around the extraction well, the fracture aperture change is minimal.

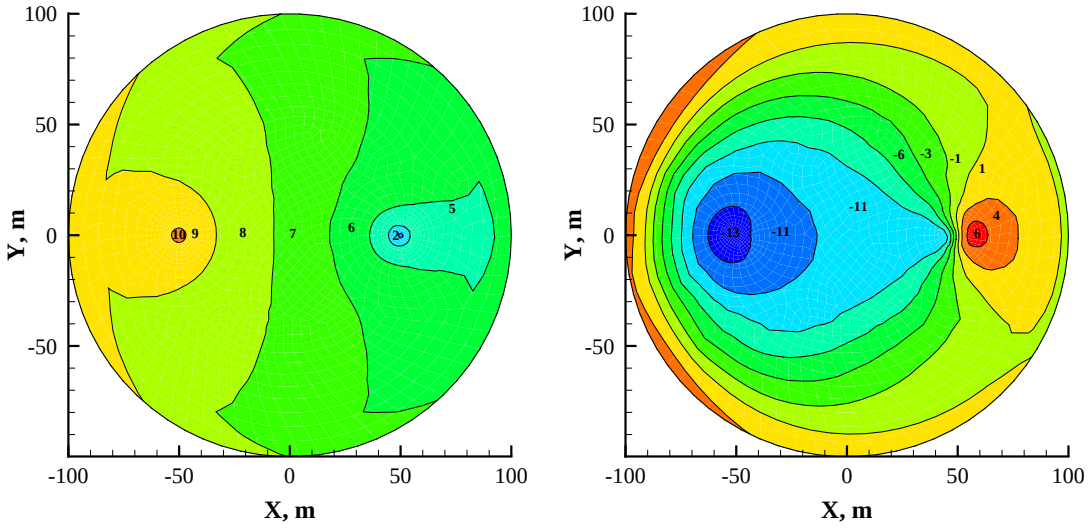

(a) (b)

Fig. 5.10 Distributions of (a) poroelastic and (b) thermoelastic stress component, σ_{zz} (MPa) on the fracture plane after 1 year of fluid injection.

Figs. 5.10a and 5.10b show the poroelastic and thermoelastic stress components perpendicular to the fracture, σ_{zz} (compression positive). The poroelastic stress is related to fluid leak-off into the formation while the thermoelastic stress is caused by the heat exchange between the injected fluid and the reservoir matrix. The total stress is sum of the contributions of thermo-and poroelastic stresses as well as the stress caused by the

fracture opening (displacement discontinuity). Note that as expected, the poroelastic stress (Fig. 5.10a) is compressive (due to increase in fluid content in the pores) except in a small region near the extraction well where fluid is extracted from the matrix.

On the other hand, the induced thermal stresses (Fig. 5.10b) are tensile where the fracture surface is cooled due to lower temperature fluid. The maximum normal tensile stress is induced at the injection well where the most cooling has occurred. It is important to note that the magnitudes of σ_{zz} thermal stress are slightly higher than those caused by pore pressure. However, the values of induced tangential components, σ_{xx} and σ_{yy} would be an order of magnitude higher (Ghassemi et al. 2007) .

5.1.3 Pressure, Temperature and Stress Change in the Reservoir Matrix

Figs. 5.11a and 5.11b show the distributions of the pore pressure and temperature in the reservoir matrix in the plane corresponding to the cross-section I-E shown in Fig. 5.1 at fluid injection time of 1 year. It is observed that the pore pressure in the matrix has increased (e.g., by 20 MPa at 5 m in the reservoir) over a large region around the injection well and it is decaying to in-situ pore pressure condition at a distance of 180 m (Fig. 5.11a).

However, the thermal front moves at a slower rate than the one for its fluid counterpart due to lower thermal diffusion rate (two-order of magnitude lower than fluid diffusion) as depicted in Fig. 5.11b. In this example, the cooled zone of reservoir matrix (by ~ 100 K) is about 5 m from the fracture surface near the injection well.

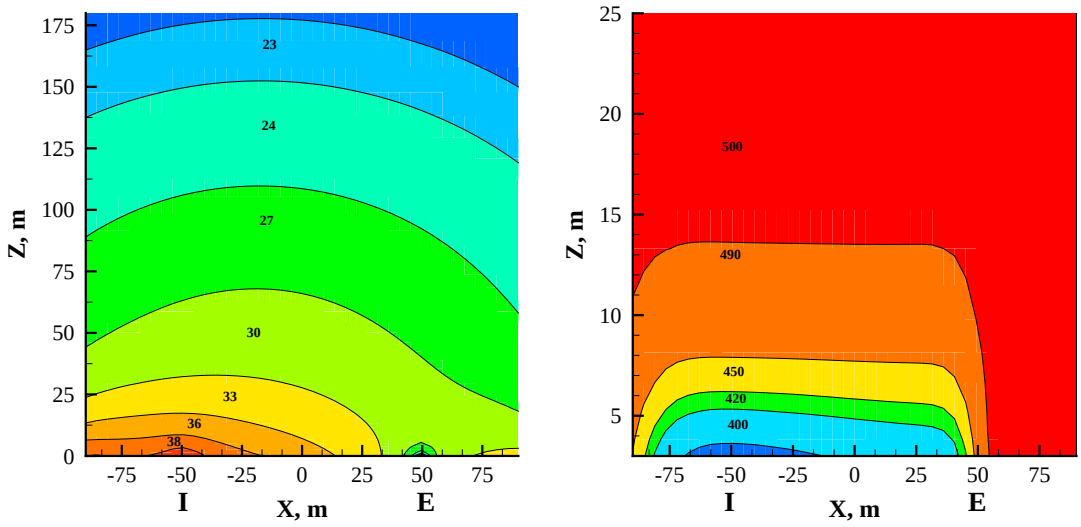

(a) (b)

Fig. 5.11 Distributions of (a) pressure (MPa) and (b) temperature (K) in the reservoir (at cross-section I-E) after 1 year of fluid injection.

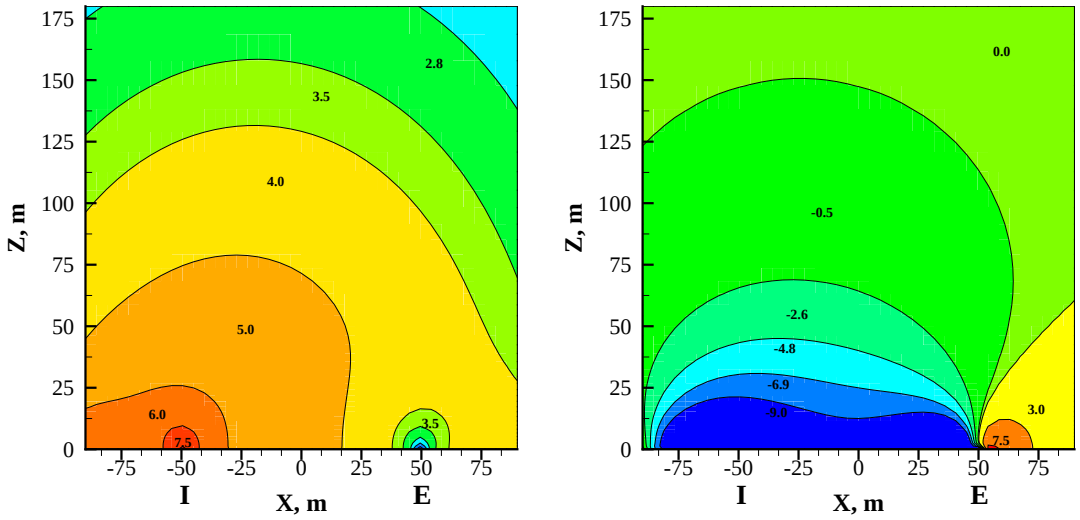

(a) (b)

Fig. 5.12 Distributions of (a) poroelastic and (b) thermoelastic stress component, σ_{zz} (MPa), in the reservoir (at cross-section I-E) after 1 year of fluid injection.

The induced poroelastic and thermoelastic stresses in the reservoir matrix in the plane corresponding to the cross-section I-E (Fig. 5.1) after 1 year are plotted in **Figs. 5.12a and 5.12b.** The contributions of thermoelastic stress and poroelastic stresses to the total stresses are in opposite nature. However, stresses acting on the fracture surface are greater than those in the reservoir matrix in both the cases, as expected. Stress induced due to poroelastic effects are of compressive and dominant near the injection well. In this example, the maximum value of poroelastic stress is of ~8 MPa in this region (Fig. 5.12a). However, a tensile stress zone is developed near the injection well depicting the significance of rock-cooling on induced total stress, maximum tensile stress of (~9 MPa; at 5 m in the reservoir) (Fig. 5.12b).

5.1.4 An Example Considering Heterogeneity of Joint Normal Stiffness

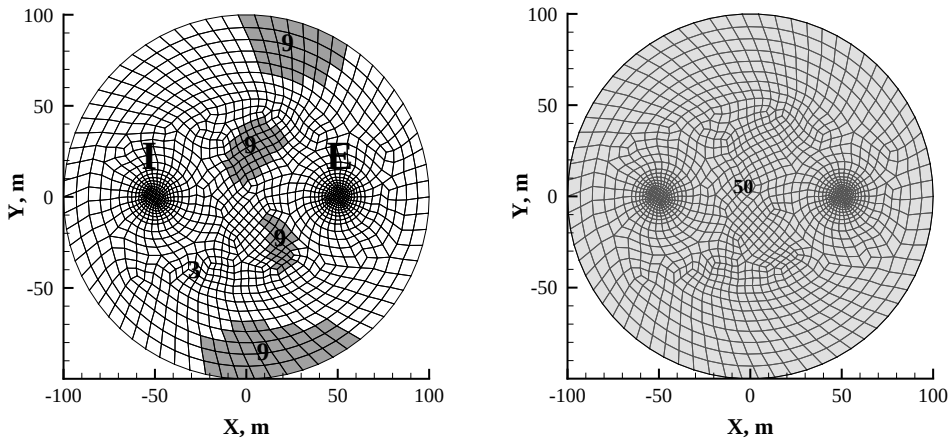

(a) (b)

Fig. 5.13 Distribution of (a) joint stiffness (Pa/m)– 9×10^{11} (shaded zones), 3×10^{11} (white zones) and (b) initial fracture aperture (μm).

Simulation results for fracture aperture, temperature and silica dissolution in the fracture plane considering heterogeneous joint normal stiffness (**Fig. 5.13a**) are presented next. In this case, joint normal stiffness (9×10^{11} Pa/m) in certain areas is three times larger than elsewhere in the fracture (see Fig. 5.13a), while all other input parameters are same as in Table 5.1. The initial fracture aperture distribution is shown in Fig. 5.13b.

The higher joint stiffness means that the joint provides more resistance to closure under in-situ stress and opening under the combined action of fluid pressure and thermo-poroelastic stresses, resulting in heterogeneous aperture distribution and channelized flow. The fracture apertures caused by the combined thermo-poroelastic effects are in the range of 60-90 μm compared to 90-145 μm for the homogeneous joint case (see **Fig. 5.14a** and Fig. 5.9b). Since fracture aperture is coupled with pore pressure, stress and heat and solute transfer in the fracture plane, the latter two are also affected by the heterogeneous joint stiffness. The influence of the zones of higher joint stiffness on distribution of temperature is shown in Fig. 5.14b. The increased joint stiffness influences fracture temperature distribution by reducing the reservoir rock cooling zone. In this example, cooling down to 350 K is restricted over higher joint stiffness zones (compare Fig. 5.14b and Fig. 5.5).

However, temperature at the extraction well is minimally affected in this example, increasing just by 1 K at 1 year. A fully-coupled flow and deformation analysis may show a larger effect resulting from flow channeling.

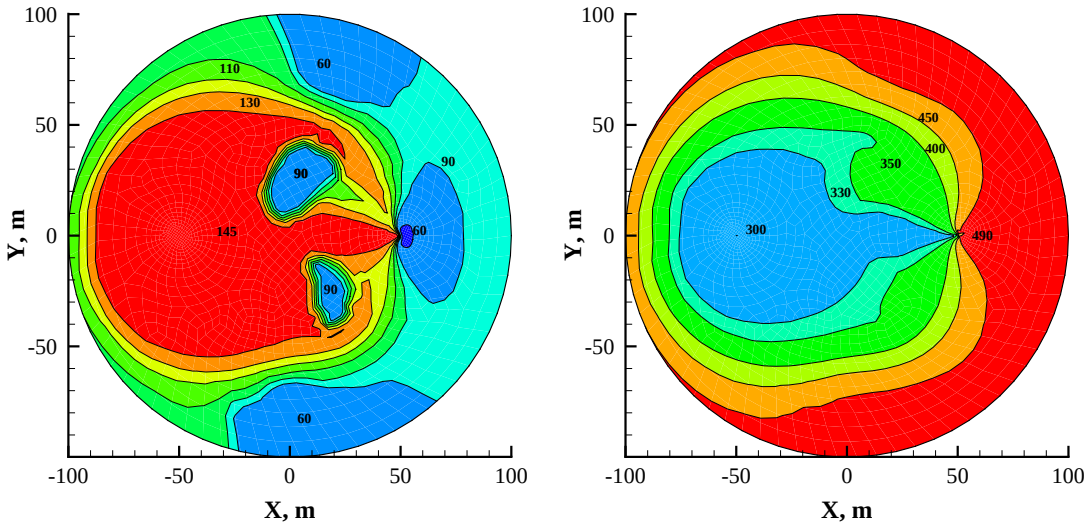

(a) (b)

Fig. 5.14 Distributions of (a) fracture aperture (μm) due to combined thermo-poroelastic effects and (b) temperature (K) in the fracture: after 1 year of injection.

Since the temperature distribution and flow path are changed by heterogeneous joint stiffness, silica concentration is also get affected; in undersaturated fluid injection case, the spreading of lower concentration towards the extraction well is restricted in the higher joint stiffness region (compare **Fig. 5.15** with Fig. 5.2). Moreover, the silica dissolution area is extended near higher joint stiffness zone because of increased silica reactivity at higher temperature (rock matrix is less cooled in higher joint stiffness region, see Fig. 5.14b). This effect is more apparent at longer injection time (1 year), suggesting time dependency of silica reactivity. For example, after 1 year of undersaturated fluid injection, the maximum fracture aperture (63 μm) due to silica dissolution is extended over a larger area (compare Fig. 5.15c with Fig. 5.3b) compared to previous example (homogeneous joint stiffness).

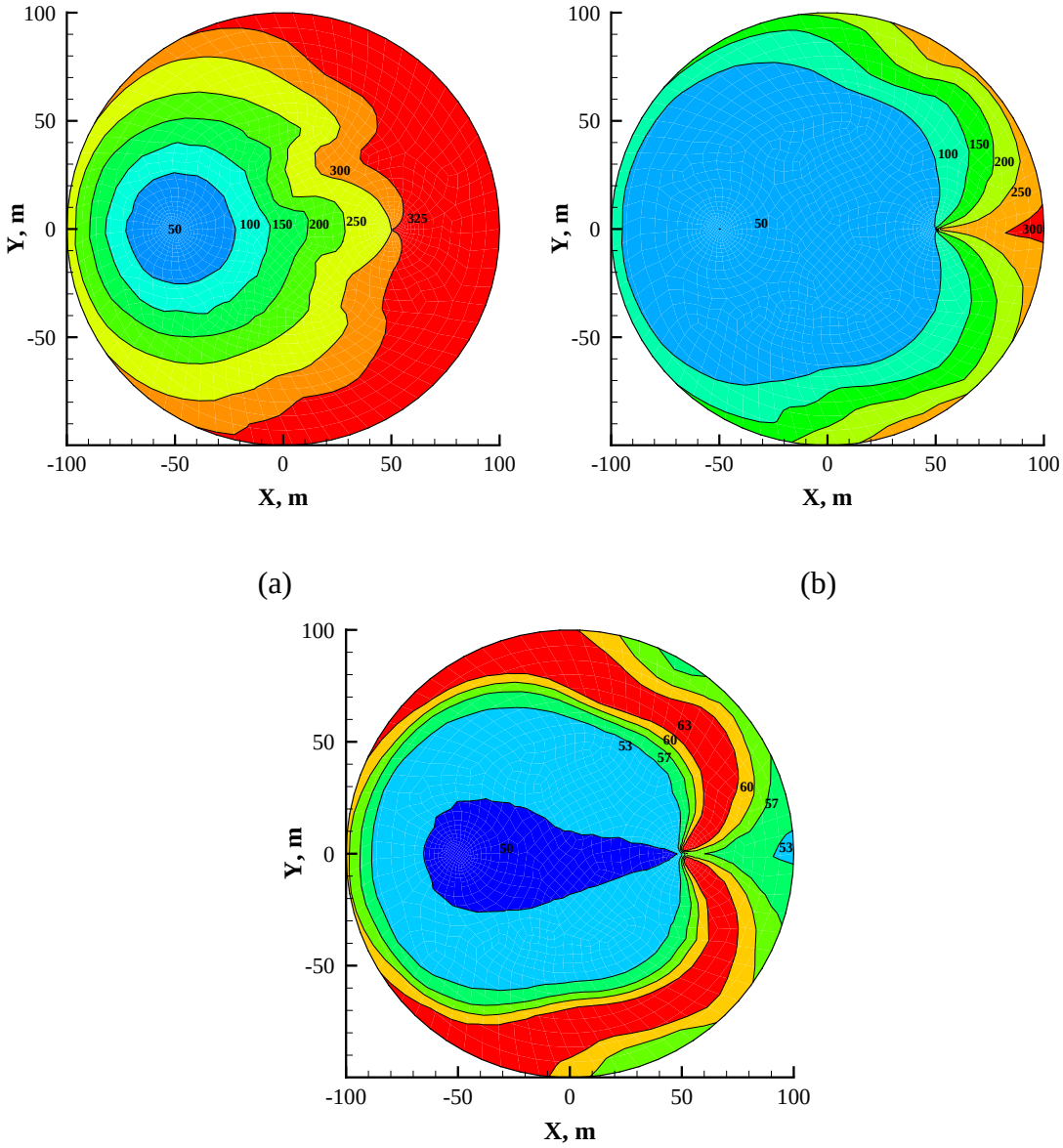

Fig. 5.15 Silica concentration (ppm) in the fracture at (a) 5 days and (b) 1 year; (c) fracture aperture (μm) due to silica dissolution at 1 year.

5.1.5 Summary of Results

We analyzed reactive flow in a fracture while considering thermo-poroelastic effects associated with cold water injection for heat extraction in a natural fracture using the thermo-poroelastic-chemo module of hybrid BEFEM model. Results show that injecting undersaturated cold geothermal fluid causes large silica mass dissolution in the fracture in a zone that extended towards the extraction well over time, increasing the fracture aperture in this zone. Fluid pressure near the injection well initially increases with injection and aperture reduction in response to leak-off, however, pressure decreases as cooling proceeds. Thermo- and poroelastic stresses alter the stress state in the reservoir matrix. The maximum normal tensile stress is induced at the injection well where the most cooling has occurred. However, it has observed that not only tensile stress develop due to cooling but also compressive stresses are induced outside of the cooled zone. Moreover, the thermoelastic effects have large impacts on fracture aperture than those compared to poroelastic effects. Higher joint normal stiffness reduces fracture aperture due to thermo- poroelasticity, while it expands the silica dissolution zone.

5.2 Poroelastic Analysis of Hydraulic Fracturing

5.2.1 Penny Shaped Fracture

In this example, the distribution of pore pressure and three-dimensional stress and fracture geometry are numerically computed in simulating hydraulic fracturing. In addition, the induced stress and pore pressure in the reservoir are used to evaluate the

potential for rock failure. The purpose of this simulation is to show the capability of hybrid model to simulate hydraulic fracturing and evaluate the potential rock failure in the reservoir. Furthermore, understanding of induced pore pressure, critically stressed zone and stimulated reservoir volume is useful in reservoir development and management works.

A quasi-static technique is adopted here to simulate a hydraulic fracture simulation in poroelastic reservoir rock (cf. Section **3.3.2**). Once the facture geometry and fluid pressure in the fracture calculated, stress and pore pressure in the formation are computed and rock failure potential is evaluated using the Mohr-Coulomb failure criterion (cf. Section **2.3**).

For simplicity, we assume that the rock matrix permeability is constant during pumping, though usually it will increase due to the rock failure around the central fracture. The rock mass permeability is estimated using a weighted average of matrix and fracture permeability. The in-situ stress field of the reservoir are considered to be of $\sigma_{zz} = 78.0$ MPa , $\sigma_{yy} = 38.0$ MPa , $\sigma_{xx} = 50.0$ MPa and pore pressure of $p = 25$ MPa . It is assumed that the intact rock has a friction angle of 35^{o} , a uniaxial compressive strength of 115 MPa and a tensile strength of 15 MPa . The fracture surface is divided into 1056 four-node quadrilateral elements with 1125 nodes. Other input parameters considered in this example are given in **Table 5.2.**

Table 5.2 Input data considered for hydraulic fracture simulation

Parameter	Value	Units
Injection Rate, Q	0.08	m^3/s
time	30	min
Porosity, ϕ	0.01	-
Permeability, k	1.0	md
Poisson's ratio, υ	0.25	-
Undrained Poisson's ratio, υ_u	0.47	-
Fluid viscosity, μ	0.001	Pa-s
Young's Modulus, E	37.5	GPa
In-situ pore pressure, p_0	25.4	MPa
Fracture toughness, K_{IC}	6	$MPa\sqrt{m}$

After 30 minutes of fluid injection, the propagated fracture radius is of 100 m and its opening at the wellbore is of 5 mm, as shown in **Fig. 5.16.** Due to low viscous fluid injection, the increment in fracture width at wellbore is minimal. However, fracture radius increases considerably with pumping time. This can lead to a high pressure zone extended in the formation and possible larger failure zone.

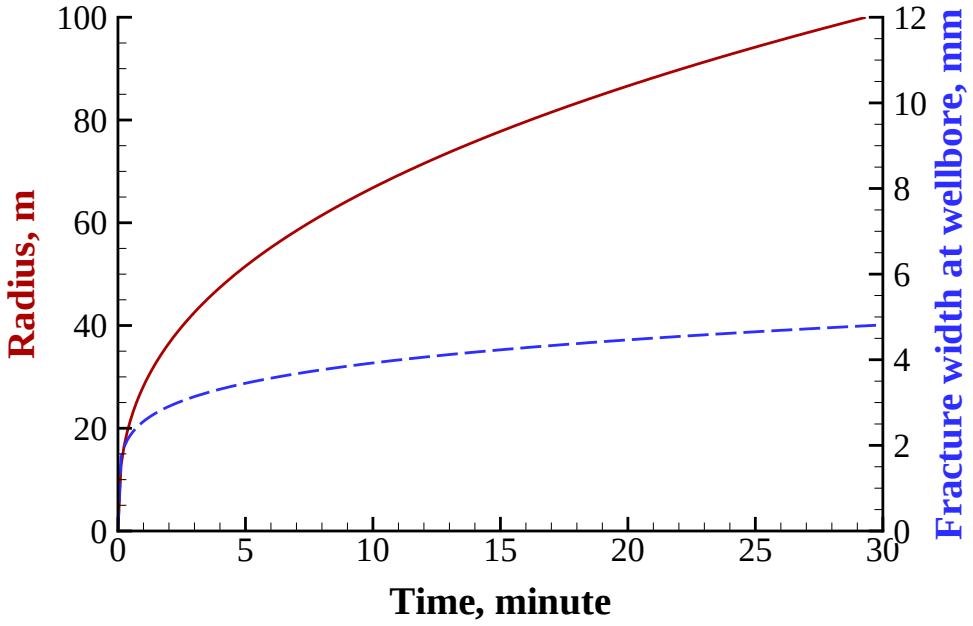

Fig. 5.16 Evolution of fracture radius and fracture opening at the wellbore during 30 minutes of fluid injection.

The snapshots of fluid pressure and fracture aperture at 4.5 minutes of fluid injection are shown in **Fig. 5.17** and **Fig. 5.18,** respectively. At this time, the fracture radius is 50 m and fracture pressure at the wellbore is of 39.4 MPa with net pressure of 1.94 MPa. The large net pressure enables to create a thick fracture (3 mm at the wellbore). This large aperture is caused by the relatively small rock permeability. Due to uniform pressure distribution and Darcy-type fluid leak-off into the formation, the fracture aperture also distributed uniformly in radial direction and vanished at the fracture tip.

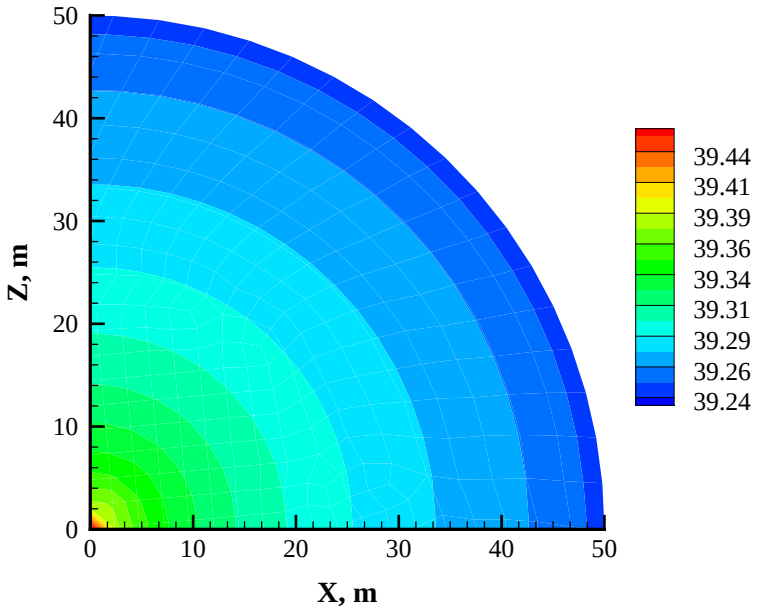

Fig. 5.17 Distribution of fluid pressure (MPa) at 4.5 minutes.

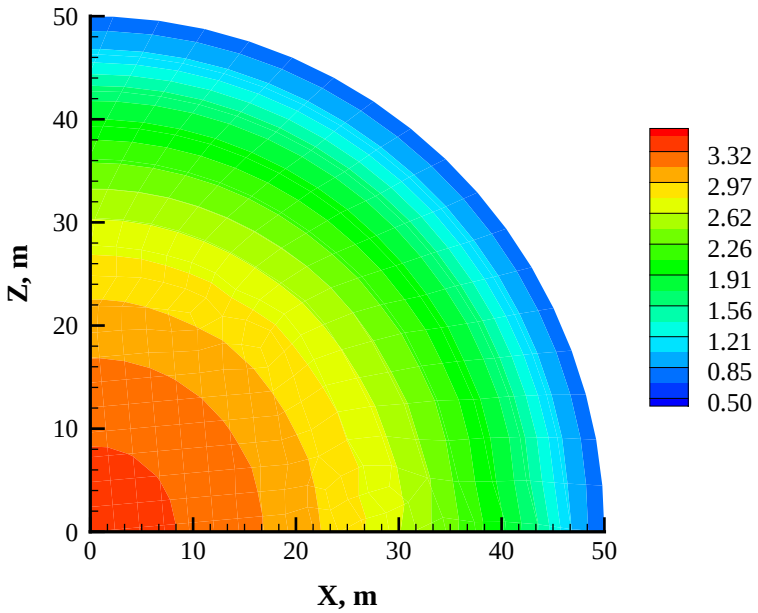

Fig. 5.18 Distribution of fracture width (mm) at 4.5 minutes.

Fig. 5.19 shows a comparison of fracture radius and its opening at the wellbore for two different values of fracture toughness– 6 MPa$\sqrt{m}$ and 10 MPa$\sqrt{m}$. As expected, it is observed that in the tougher formation, fracture propagation tends to be shorter; however, fracture width is increased due to the increased net pressure when it is compared to the less tough formation. For example, after the same amount of fluid pumping, the fracture radius is 20 m smaller and average fracture width at the wellbore is 4 mm larger in higher fracture toughness than they are in the rock with lower toughness.

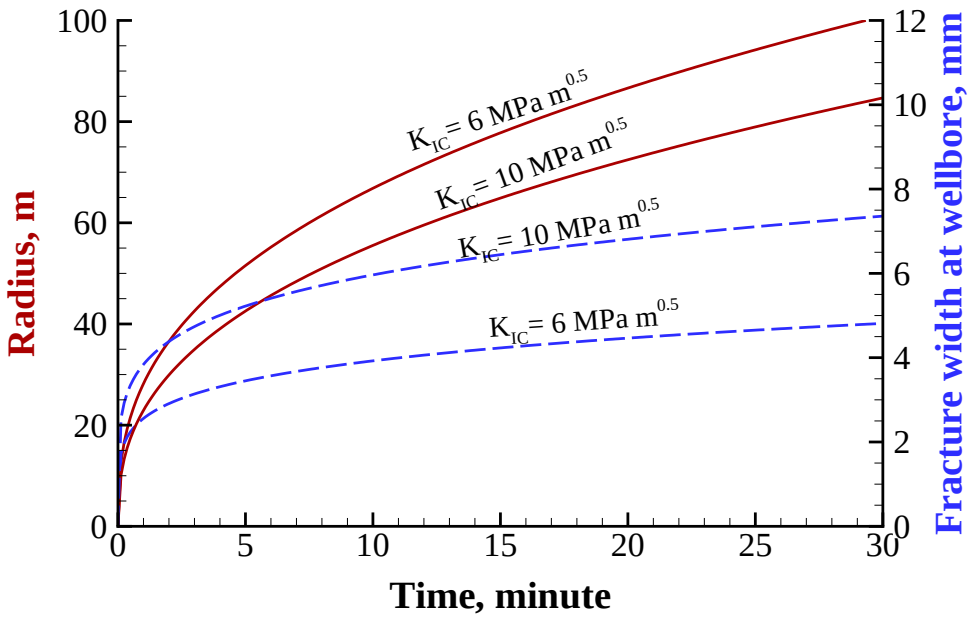

Fig. 5.19 Comparison of fracture radius and fracture width history for different fracture toughness.

Similarly, fluid pressures for the same two cases are shown in **Fig. 5.20;** in which the net increment in the fluid pressure at the wellbore is approximately 0.7 MPa in tougher formation case. From this sensitivity analysis, it is observed that the higher the fracture toughness, the higher pressure is required to extend the fracture.

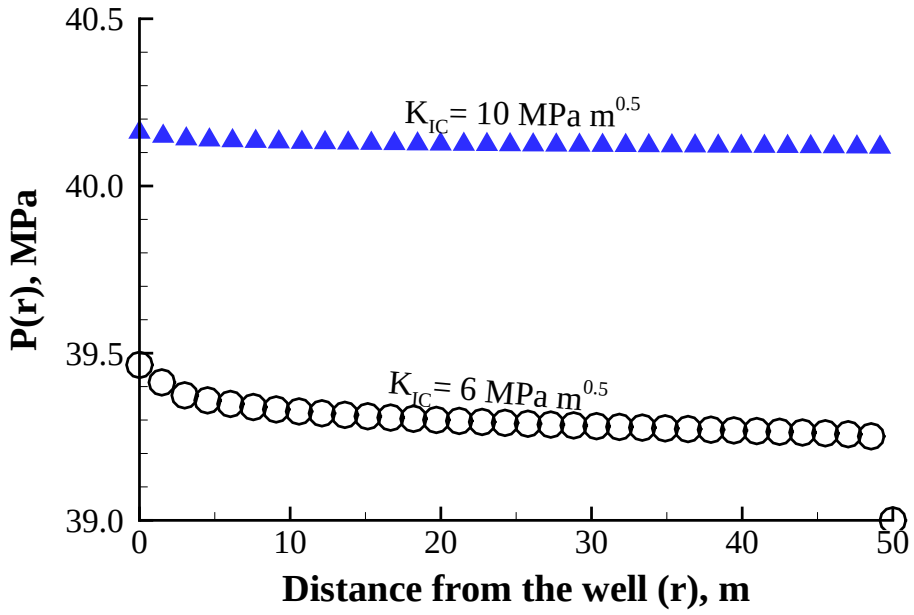

Fig. 5.20 Fluid pressure profile for different fracture toughness.

Fig. 5.21 shows the distributions of pore pressure in the horizontal cross-section of the formation. Note that the pore pressure around the fracture is raised significantly compared to the original reservoir pressure of 25 MPa. This increase in pore pressure

lowers the effective compressive stress and can cause failure on weakness planes around the hydraulic fracture.

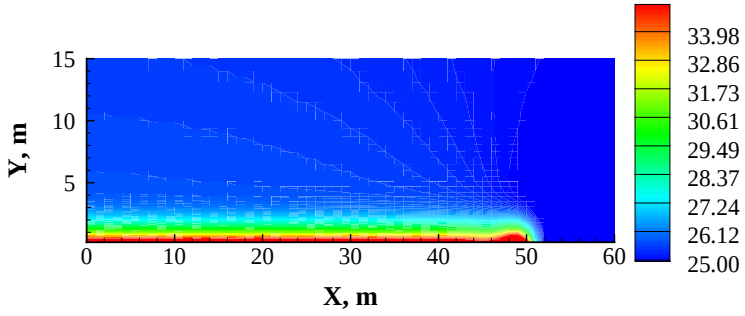

(a)

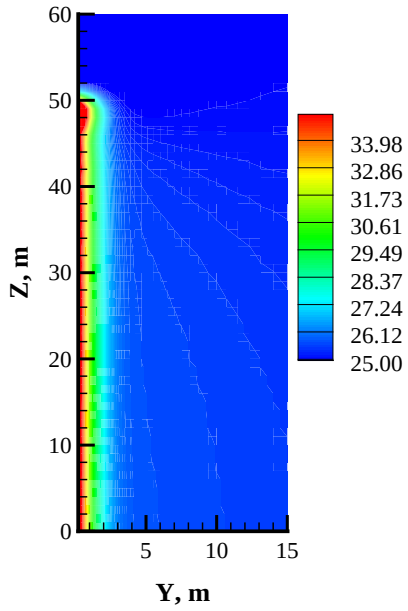

(b)

Fig. 5.21 Pore pressure (MPa) at 4.5 minutes in the cross-sections in the formation (a) X-Z plane (b) Y-Z plane.

Furthermore, stress distributions in horizontal cross-sections of the formation are shown in **Fig. 5.22.**

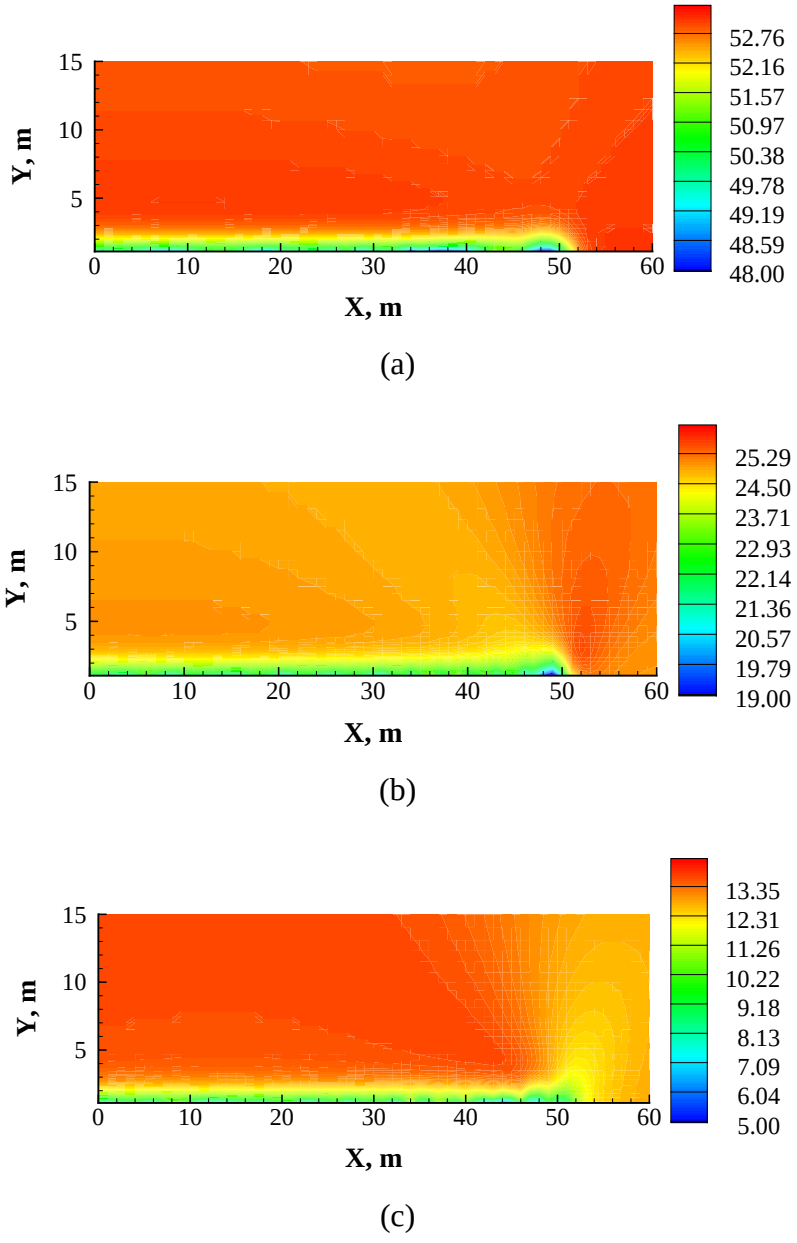

Fig. 5.22 Distribution of (a) maximum, (b) intermediate and (c) minimum principal effective stress (MPa) in the cross-sections (X-Y plane) in the formation.

The plotted stresses are effective principal stress; there is a zone of low effective stress in the rock near the fracture walls where the pore pressure has been disturbed (see Fig. 5.22 and **Fig. 5.23**).. In fact, the minimum principal stress is near zero, indicating potential failure in tension. Also, the stress distributions show the enhanced intensity of induced tension near the tip region.

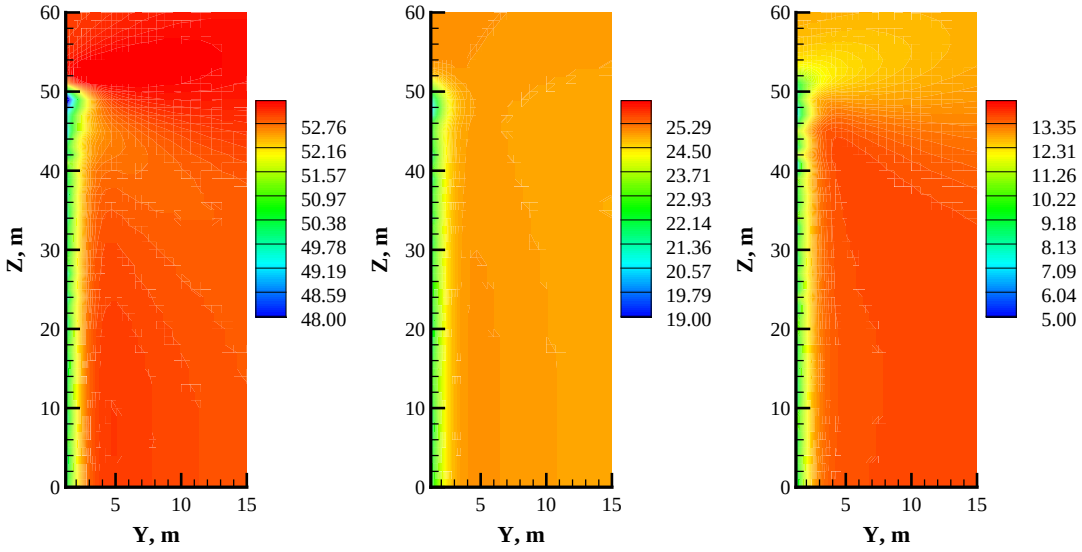

(a) (b) (c)

Fig. 5.23 Distribution of (a) maximum, (b) intermediate and (c) minimum principal effective stress (MPa) in the cross-sections (Y-Z plane) in the formation.

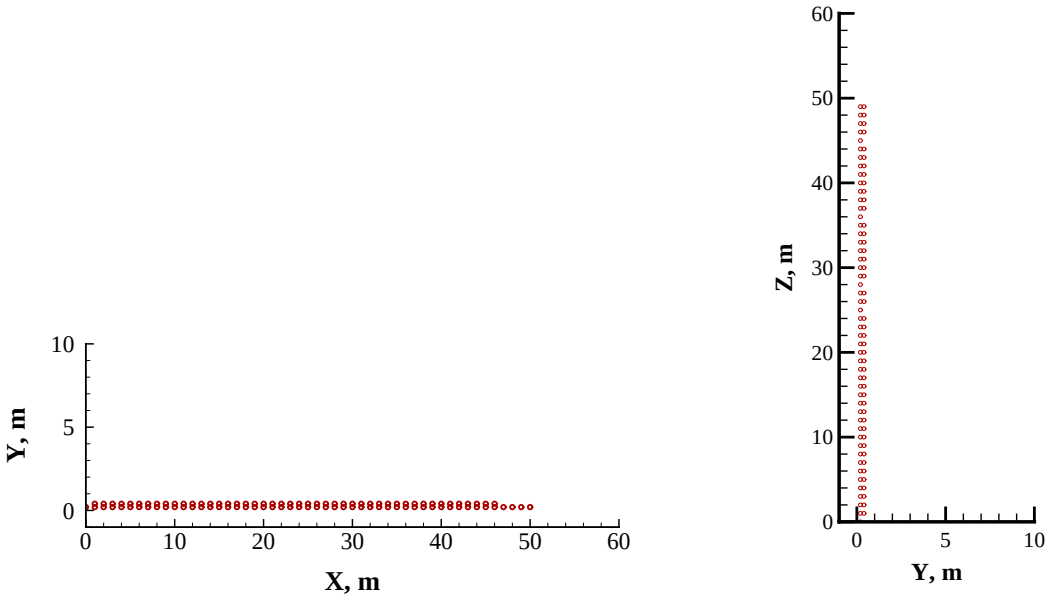

Fig. 5.24 Failure area in the formation at 4.5 minutes. Tensile failure dominates near the fracture walls.

The corresponding region of likely rock failure surrounding the fracture is shown in **Fig. 5.24** for both cross-sections (X-Y plane and Y-Z plane) at 4.5 minutes; in which the symbols signify the potential rock failure zone. The failure mode is tension for an area that extends from 1-2 m off the fracture walls.

5.2.1.1 Summary of Results

Numerical simulation shows that high pore pressures are induced in the fracture area. Zones of intense rock failure form near the fracture tips and surfaces, which is consistent with the field observations of micro-seismic events during hydraulic fracturing process. It is found that the pore pressures in the vicinity of the fracture are enhanced

significantly due to the fluid leak-off from the fracture into the formation. The higher pore pressure decreases the effective stresses and enhances rock failure potential. The pore pressure can play an important role in areas away from the tip and in contributions to slip and micro-seismicity development associated with injection process.

5.2.2 Multiple Fractures

In this example, we present an application of hybrid technique to simulate multiple fractures in poroelastic rock highlighting the characteristics of stress and pore pressure distributions and their effect on extent of the potential rock failure zone.

We consider simultaneous fluid injection into three parallel and equally spaced (50 m) transverse fractures originating from a horizontal well in the Barnett Shale. Fluid is pumped at rate of 0.03 m^3/s into the center of each fracture. It is considered that the entire planar fractures have been created at the end of the treatment, and are subjected to the injection pressures. For simplicity, we assume the rock matrix permeability is constant during the pumping process.

The elliptical shaped fractures are considered at a depth of 2460 m in in-situ stress field as: $\sigma_v = 56.5$ MPa, $\sigma_h = 39.0$ MPa, $\sigma_H = 43.3$ and $p = 28.3$ MPa. Each fracture surface is divided into 1789 four-node quadrilateral elements with 1850 nodes (see **Fig. 5.25**). It is assumed that the Barnett Shale has cohesion of 0.69 MPa, friction angle of 31^o and tensile strength of 10 MPa.

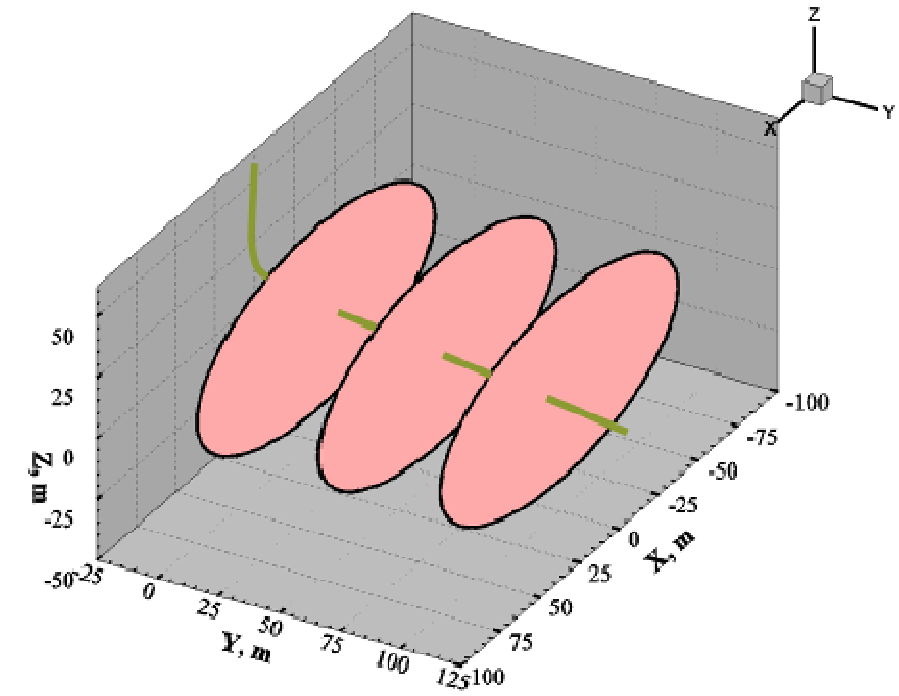

(a)

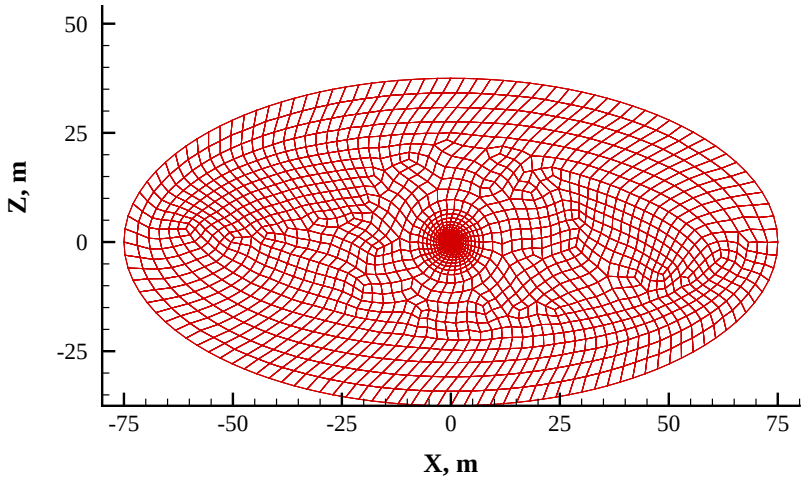

(b)

Fig. 5.25 Sketch showing (a) three parallel fractures (spacing= 50 m) in a horizontal well and (b) discretization of a fracture using four-node quadrilateral elements.

The poroelastic properties of Barnett Shale and other parameters used in this example are given in **Table 5.3.**

Table 5.3 Input data considered for multiple fracture simulation

Parameter	Value	Units
Young's modulus, E	20.7	GPa
Drained Poisson's ratio, ν	0.25	-
Undrained Poisson's ratio, ν_u	0.46	-
Fluid viscosity, μ	3.0×10^{-4}	Pa-.s
Reservoir permeability, k	0.1	md
Fluid density, ρ_f	1000	Kg/m^3
Rock density, ρ_r	2300	Kg/m^3
Fracture dimension: a, b	75, 37.5	m
Number of fractures	3	-
Fracture spacing	50	m
Pumping time	3	Hours

Fig. 5.26 shows the distribution of fracture width for the system of three parallel fractures after 3 hours of pumping. The maximum width of two outer fractures is 20 mm, whereas that of middle fracture is 17 mm. The relatively large aperture can be explained by low fluid leak-off and not enforcing $K_I = K_{IC}$ condition for this simulation. Note that

aperture of the middle crack is smaller than the other two. This is because the opening of two outer fractures compresses and tends to restrict the width of middle fracture. However, this effect decays around the edges of the middle fracture where the compressive stress from outer fractures is lower; so the opening near edges is similar to that of outer fractures. Consequently, the middle fracture will be restricted to propagate.

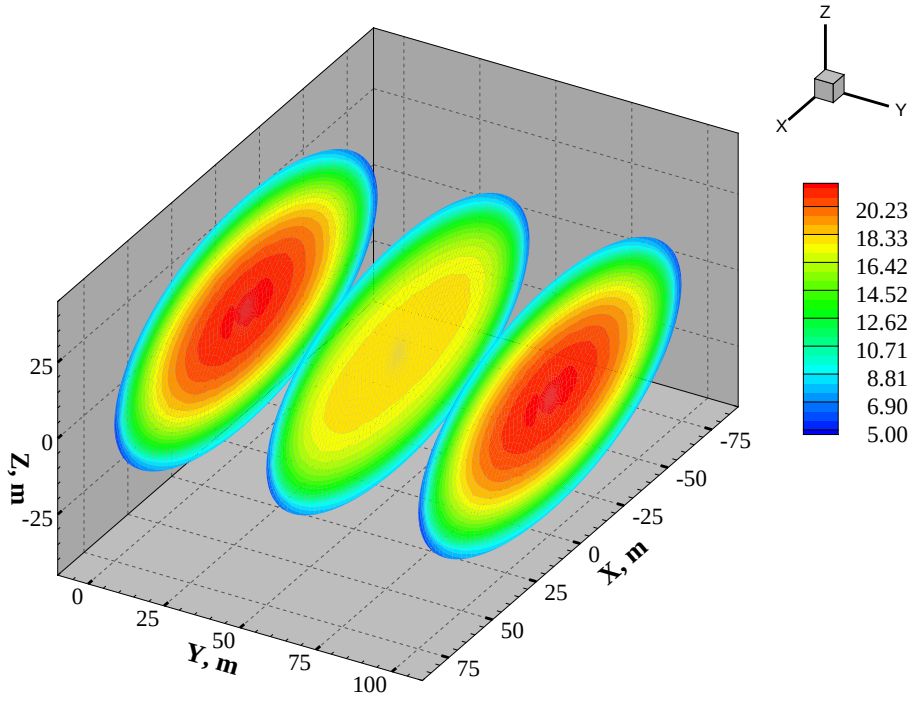

Fig. 5.26 Fracture aperture distribution (mm) after 3 hours of pumping.

The mass balance of the multiple fracture simulation is shown in **Fig. 5.27,** in which the volumes of fractures and fluid leak-off are compared. It illustrates the "shadow effect" due to stress state around the outer fractures on fracture volume. It is

observed that the fluid leak-off volume in the outer cracks is 11 m^3 less than it is from the middle one. Similarly, the volumes of an exterior fracture and the middle facture are 141 m^3 and 131 m^3, respectively.

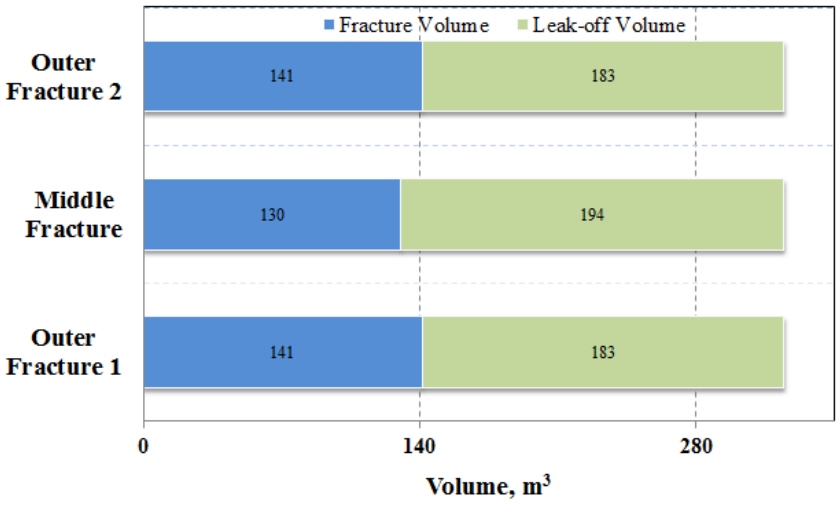

Fig. 5.27 Mass balance of multiple fracture simulation: outer fracture 1 (y = 0 m), middle fracture (y = 50 m) and outer fracture 2 (y = 100 m).

Fig. 5.28 and **Fig. 5.29** show the pore pressure distribution in the formation delineating the "shadow effect". Note that the pore pressure around the fracture is raised significantly compared to the original reservoir pressure of 28.3 MPa. The increase in fluid pressure in the middle fracture is higher (by ~1.5 MPa) compared to that in the outer fractures, which leads to higher fluid leak-off (see Fig. 5.28). However, as expected, the high pore pressure is restricted to smaller region (see Fig. 5.29) around the middle fracture due to the "shadow effect" of stresses generated around the outer ones.

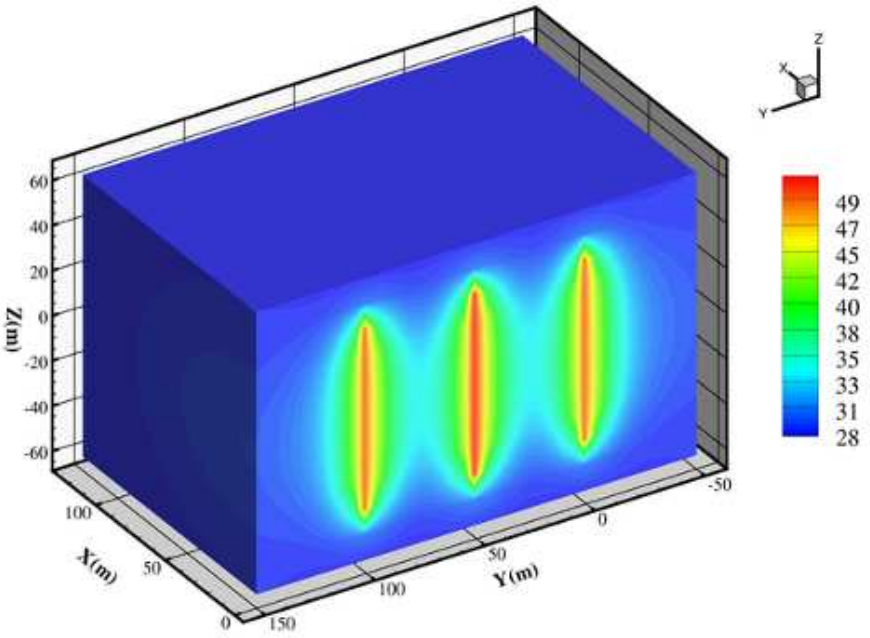

Fig. 5.28 Distribution of pore pressure (MPa) in the reservoir.

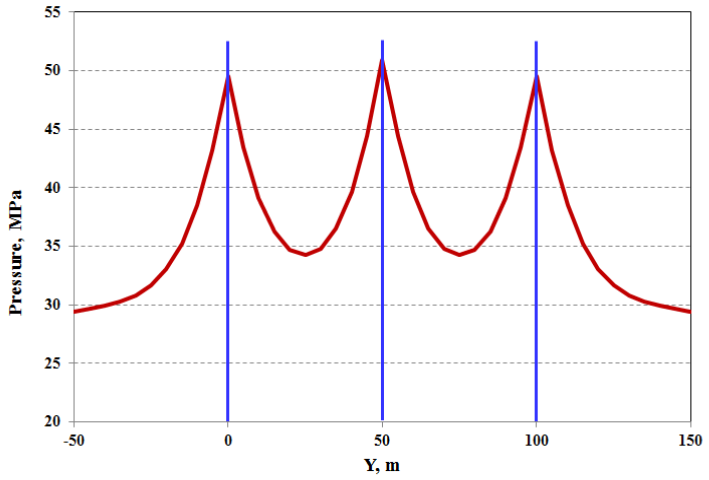

Fig. 5.29 Pore pressure profile in the reservoir.

Moreover, increase in pore pressures lowers the effective compressive stresses and can cause failure on weakness planes around the hydraulic fracture. Significant pore pressure increase around the multiple fractures develops a critically stressed rock of higher potential for failure and micro-seismicity. The corresponding distributions of the effective principal stress in the reservoir are shown next. In **Fig. 5.30,** maximum principal stresses in the reservoir are plotted**.** There are zones of low effective stress in the rock near the fractures where the pore pressure has been disturbed. In fact, the minimum principal stress is near or below zero, indicating potential failure in tension.

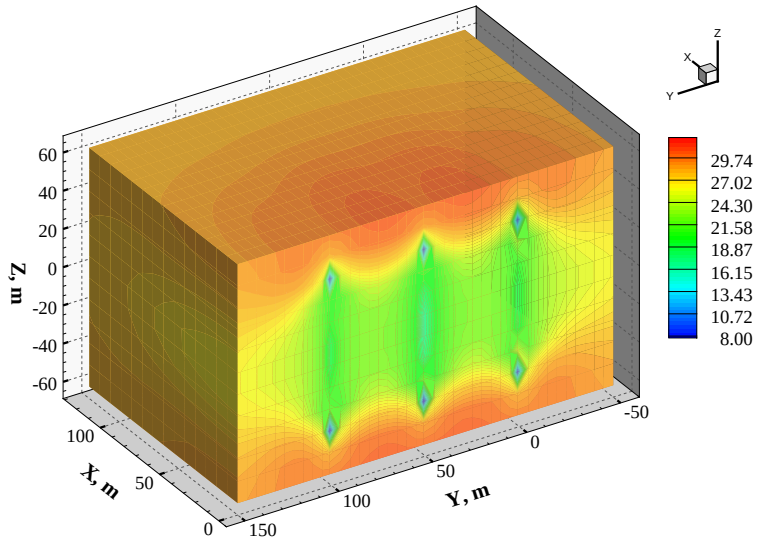

Fig. 5.30 Distribution of maximum effective principal stress (MPa) in the reservoir.

Also, the intermediate (**Fig. 5.31**) and minimum (**Fig. 5.32**) effective principal stresses are greatly reduced in the vicinity of the fractures with enhanced intensity of induced tension near the tip region.

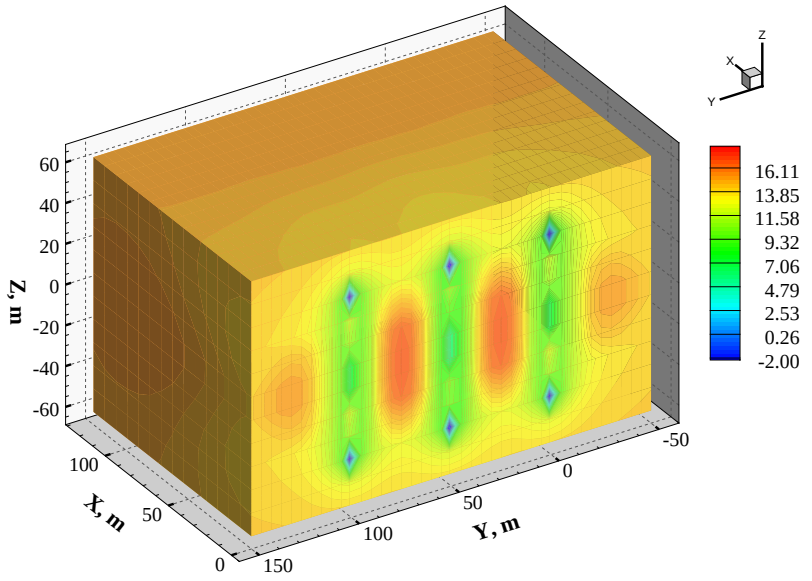

Fig. 5.31 Distribution intermediate effective principal stress (MPa) in the reservoir.

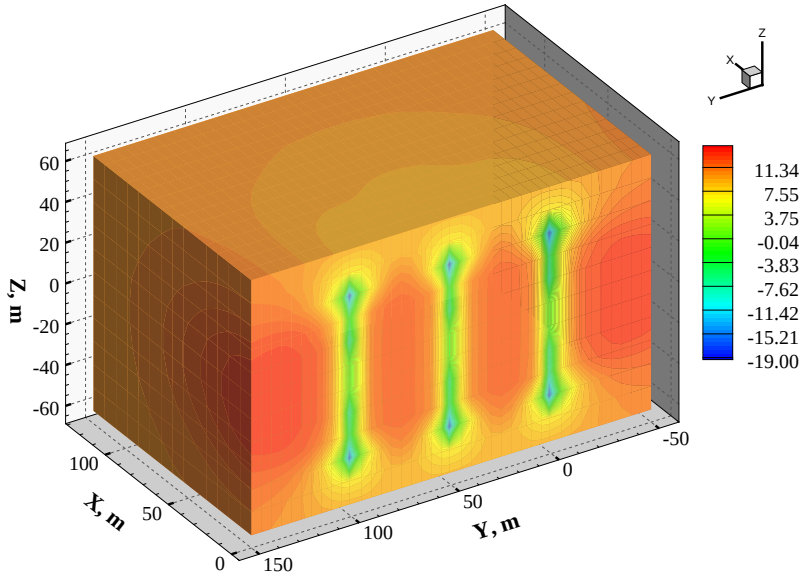

Fig. 5.32 Distribution minimum effective principal stress (MPa) in the reservoir.

The regions of potential rock failure surrounding the fractures are shown in **Fig. 5.33a and Fig. 5.33b.** The symbols are used to signify the potential rock failure zone. The failure mode is shear (Fig. 5.33a) for the area that extends from 1-10 m off the fracture walls, whereas tensile failure (Fig. 5.33b) is observed at the fracture surfaces.

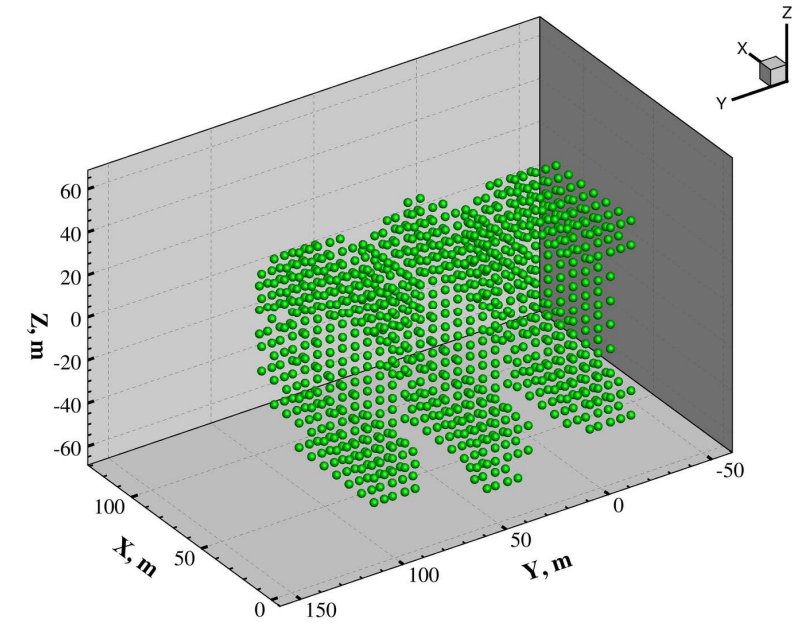

(a)

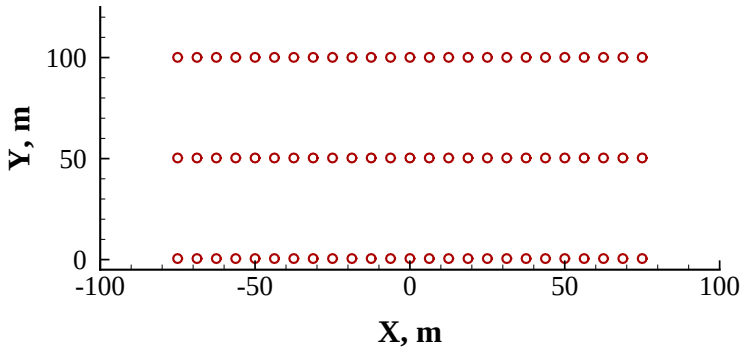

(b)

Fig. 5.33 Failure potential in the reservoir: (a) shear failure and (b) tensile failure.

5.2.2.1 Summary of Results

We have analyzed the potential for rock failure resulting from water injection during the hydraulic fracture treatment using hybrid BEFEM model. Results from this experiment show that zones of intense rock failure can form near the fracture tips and surfaces, which is consistent with the field observations of micro-seismic events during hydraulic fracturing process. It is observed that the maximum, intermediate and minimum effective principal stresses are greatly reduced in the vicinity of the fractures due to the large induced pore pressure. The higher pore pressure decreases the effective stresses and enhances rock failure potential. The pore pressure also plays an important role in areas away from the tip and contributes to slip and micro-seismicity development associated with injection process.

5.3 Deformation Due to Injection and Production in the Reservoir

In this section, the hybrid BEFEM model incorporating coupled geomechanics and reservoir flow is applied to investigate reservoir response to the fluid injection and/or production. The poroelastic reservoir layer deformation module applied here is described in detail in Section **3.3.3**.

In this section, we present two example problems to highlight the distributions of pore pressure, stress and reservoir deformation during injection and/or production from the reservoir. First, a single well production from the reservoir is studied; the purpose of this experiment is to validate the modeling capability of the hybrid technique

highlighting Mandel-Cryer effects. Next, an inverted 5-spot problem is simulated to investigate the influence of injection and production procedures on pore pressure, stress state and deformation in the reservoir.

5.3.1 Single Well Production

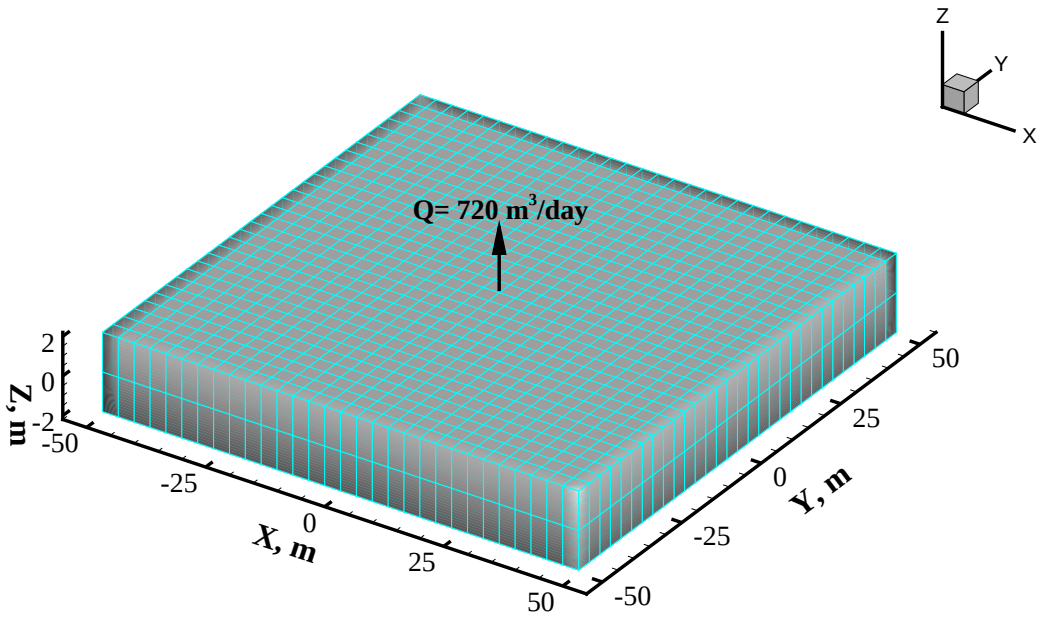

Fig. 5.34 Reservoir discretization: a producing well is placed at the center.

In this example, a single well producing at a constant rate from the reservoir is considered, assuming single phase and isothermal fluid flow in the reservoir. The reservoir size is of 100×100×4 m and production well is placed at the middle of the reservoir. The production well is produced at constant rate 720 m^3/day and the reservoir is subjected to zero pressure boundaries. The reservoir is discretized using 20-node 1800

brick elements with 10385 nodes for FEM, while 4-node 900 quadrilateral elements with 961 nodes are used in BEM representing the overburden (see **Fig. 5.34**). The input parameters considered for this example are given in **Table 5.4.**

Table 5.4 Input data considered for single well production simulation

Parameter	Value	Units
Reservoir		
Young's modulus, E	1.0×10^{7}	Pa
Drained Poisson's ratio, v	0.3	-
Undrained Poisson's ratio, v_u	0.49	-
Fluid viscosity, μ	1.0×10^{-3}	Pa-s
Biot's coefficient, α	0.99	-
Reservoir permeability, k	1000.0	md
Overburden		
Young's modulus, E	1.0×10^{7}	Pa
Drained Poisson's ratio, v	0.3	-

Variable time steps (of 1 minute and 15 minute) are used to capture early time transient behavior in the reservoir. The average runtime per time step was approximately 45 seconds. The convergence history of displacement discontinuity in the hybrid BEFEM model during exchanging the information between FEM reservoir and BEM overburden zone is shown in **Fig. 5.35.**

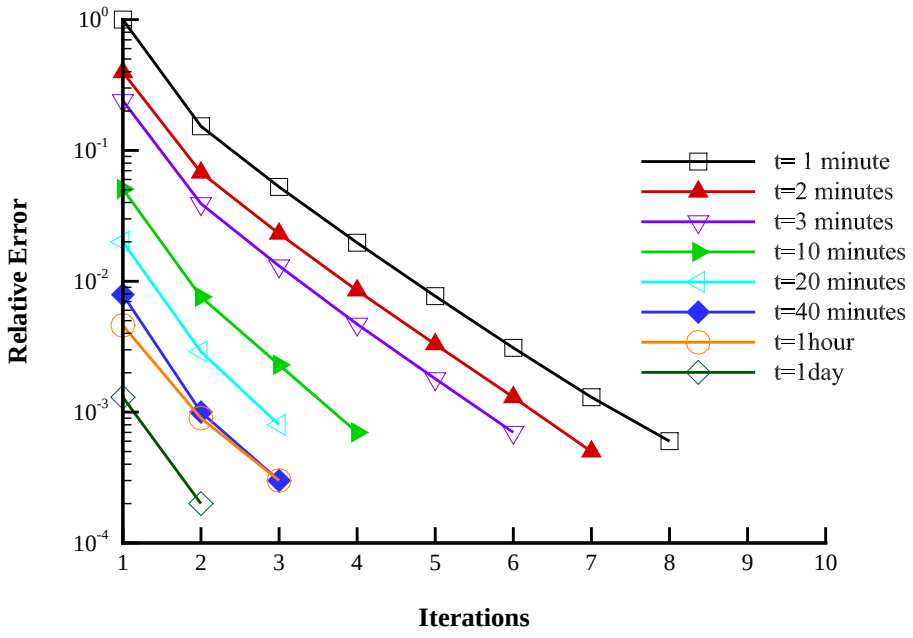

Fig. 5.35 Convergence in displacement discontinuity: maximum of 8 iterations are required for one time step in this example.

Similarly, the continuity of stress is demonstrated by the consistency of the stresses from both the FEM model and BEM model, shown in **Fig. 5.36,** in which the profiles of stress (σ_{zz}) at the top of the reservoir layer are plotted along the x-axis.

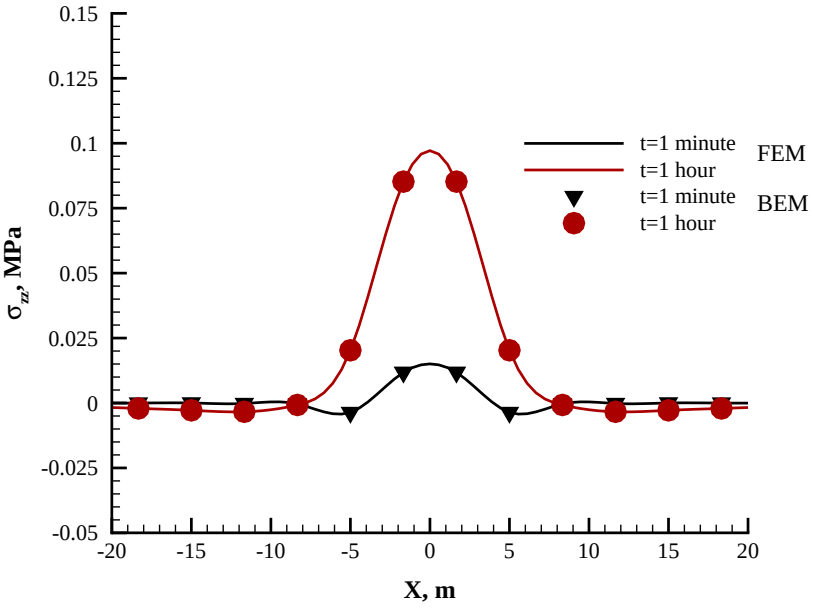

Fig. 5.36 Stress ccontinuity at the reservoir top layer.

Similar to Mandel's problem, the non-monotonic (first rising, then falling) pore pressure response adjacent to the center of the reservoir is observed (see **Fig. 5.37** and **Fig. 5.38**). This is because the initial sharp removal of the fluid from the single well at the center of the reservoir considerably softens the center reservoir region. Due to the compatibility requirement, compressive total stress is transferred towards the effectively stiffer region adjacent to the center. This load transfer generates pore pressure such that the pressure in the area adjacent to the center rises for a while before it dissipates. The truthful replication by the BEFEM model is part of this example.

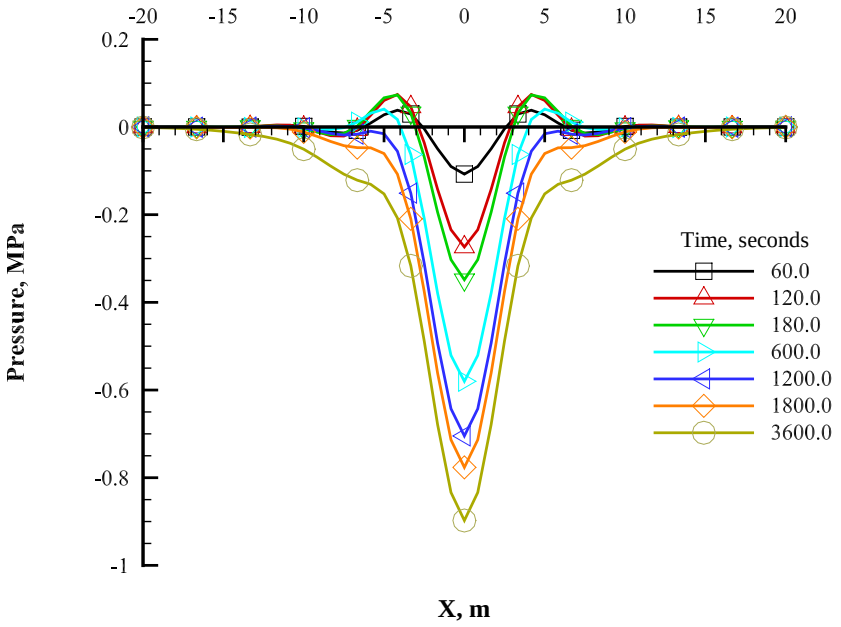

Fig. 5.37 Pore pressure profiles at different times: the x-coordinate is along the production well.

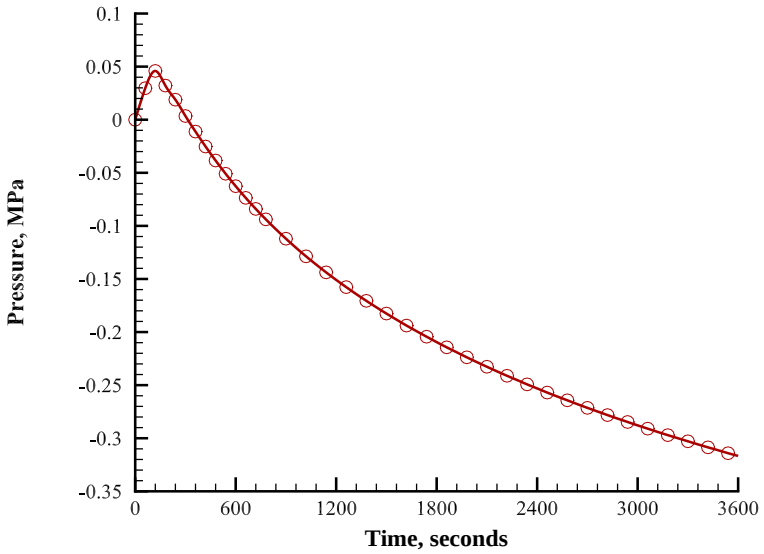

Fig. 5.38 Pore pressure evolution at node adjacent to the producing well.

The distributions of pore pressure, stress (σ_{zz}) and vertical displacements in the reservoir presented next. As expected, due to the fluid production at center of reservoir constrained by constant zero boundary pressures, the maximum pressure drawdown exist at production well. The drawdown in production well is 1.5 MPa after 1 day of production (see **Fig. 5.39**).

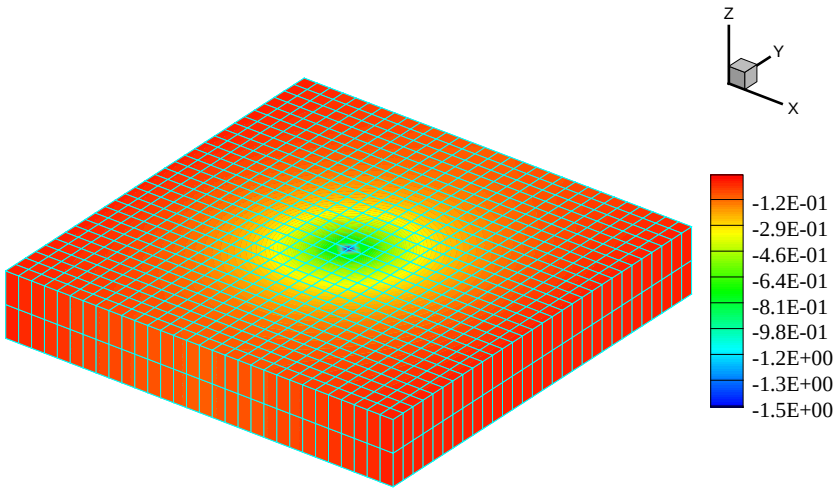

Fig. 5.39 Pore pressure (MPa) in the reservoir at 1 day.

Similarly, continuous depletion of pore pressure reduces the pore spaces in the reservoir and thus induces the compressive stress (see **Fig. 5.40**). Moreover, combined influence of both the reservoir and overburden stresses results the net effect of compaction of the reservoir. Maximum compaction of 15 cm is observed near the production well whereas the compaction in the far field reservoir is 8 mm (**Fig. 5.41**).

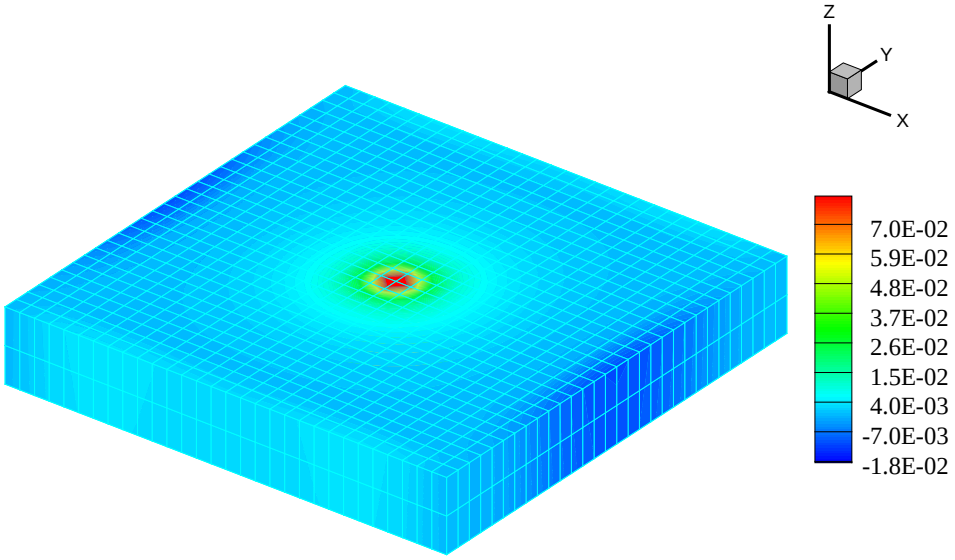

Fig. 5.40 Vertical stresses (MPa) in the reservoir at 1 day.

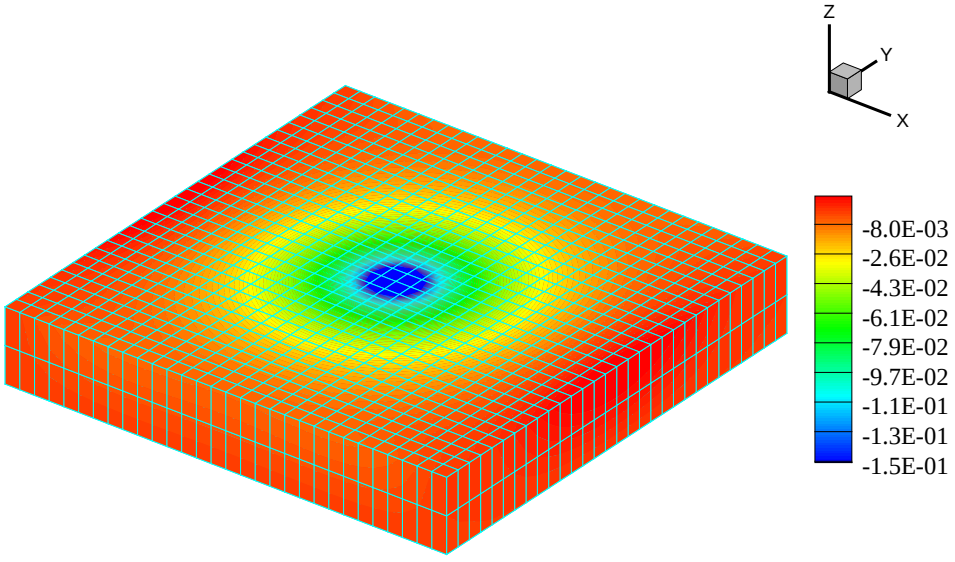

Fig. 5.41 Vertical displacement (m) in the reservoir at 1 day.

5.3.2 Inverted 5-Spot Well

In this example, we present an inverted 5-Spot well problem to investigate the effects of injection and production procedure on the reservoir deformation and stress in the reservoir. Suppose an injection well is placed at the center of 120×120×20 m reservoir, while production wells are placed at four corners of the reservoir. The constant injection and production rates considered are 800 m^3/day and 80 m^3/day respectively. A Cartesian coordinate system is considered where the top and bottom of the reservoir are normal to the z-axis and the all the sides are normal to X-Y plane. The reservoir boundaries are considered to be no flux boundary and initial in-situ stresses and pore pressures are taken zero for simplicity.

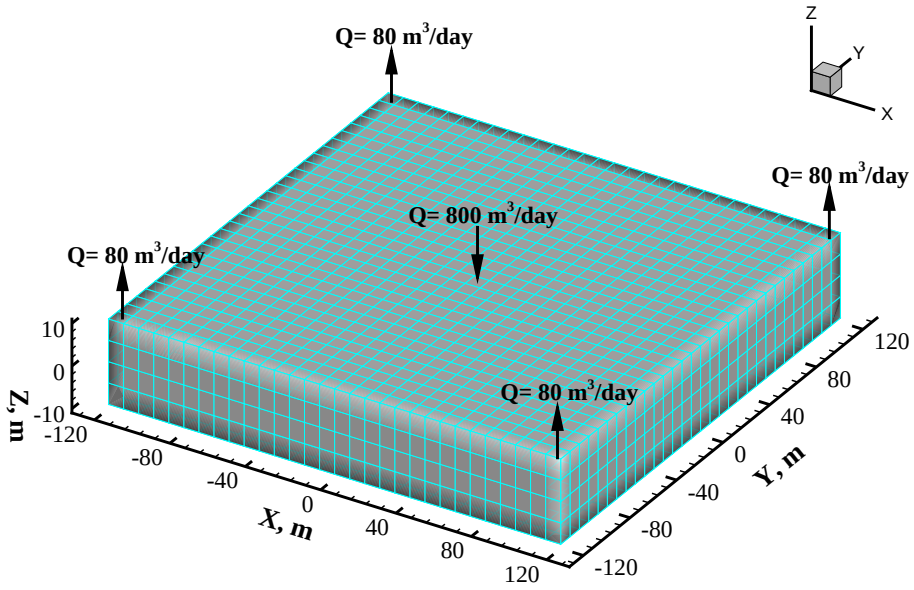

Fig. 5.42 Reservoir discretization: an injection well is at the center and four production wells are at the corners.

The reservoir is discretized with 20-node brick elements (total of 3600 elements and 17949 nodes) for FEM while overburden is discretized with 4-node quadrilaterals (total of 900 elements and 961 nodes) for BEM (see **Fig. 5.42).** The input parameters considered in this example are given in **Table 5.5.** Results for pore pressure, displacement and stresses in the reservoir are presented next.

Table 5.5 Input data considered for inverted 5-spot well simulation

Parameter	Value	Units
Reservoir		
Young's modulus, E	5.0×10^{8}	Pa
Drained Poisson's ratio, v	0.3	-
Undrained Poisson's ratio, v_u	0.47	-
Fluid viscosity, μ	1.0×10^{-3}	Pa-s
Biot's coefficient, α	0.99	
Reservoir permeability, k	1000.0	md
Overburden		
Young's modulus, E	2.0×10^{9}	Pa
Drained Poisson's ratio, v	0.3	-

In this example, $\Delta t = 0.1$ day and total $(\text{ns} = 50)$ time steps are used for simulating reservoir response. The average runtime per time step was approximately 1

minute. The convergence history of displacement discontinuity in the hybrid BEFEM during exchanging the information between FEM reservoir and BEM overburden zone is shown in **Fig. 5.43.**

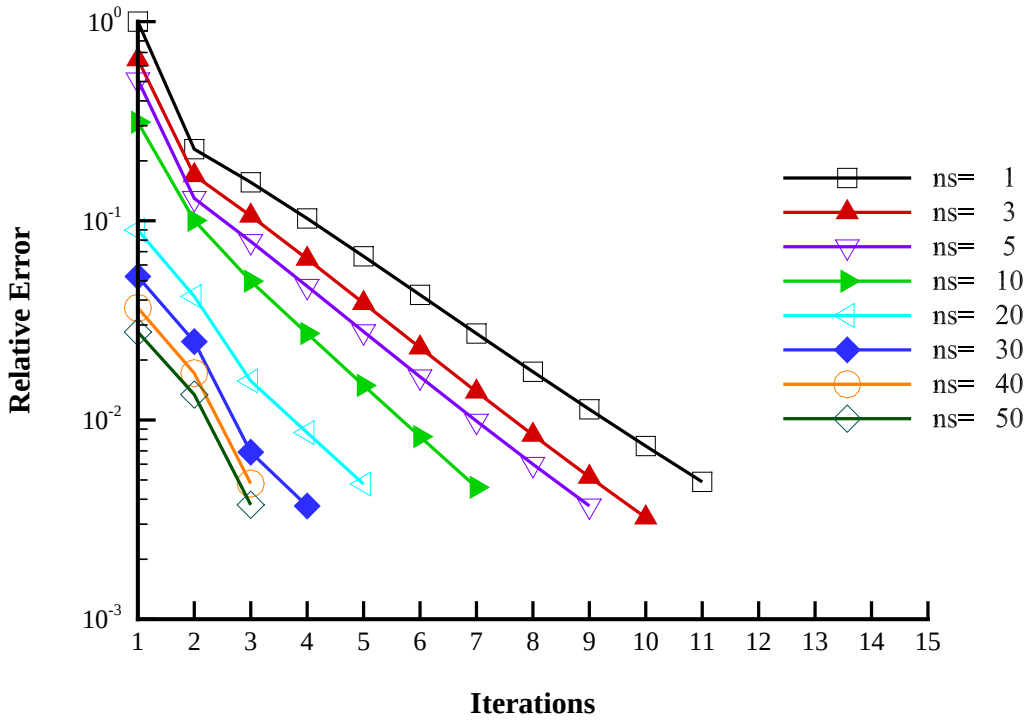

Fig. 5.43 Convergence in displacement discontinuity: maximum of 11 iterations required for one time step in this example.

Fig. 5.44 shows the induced pore pressures in the reservoir during injection and production procedure. The computed pressure at the injection well is 0.3 MPa and that at production wells is 0.04 MPa after 1 day. The high injection pressure is due to the "over injecting" since the reservoir boundaries are set to no-flow boundary.

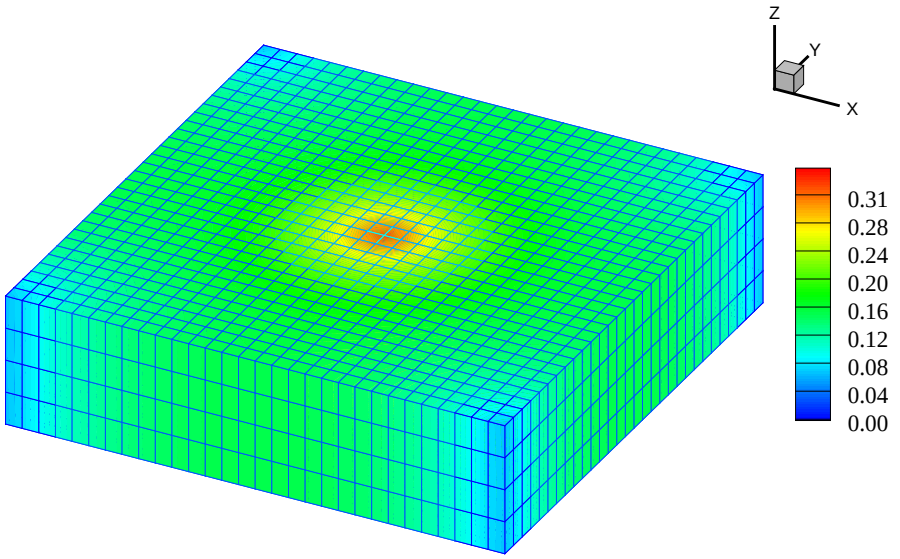

(a)

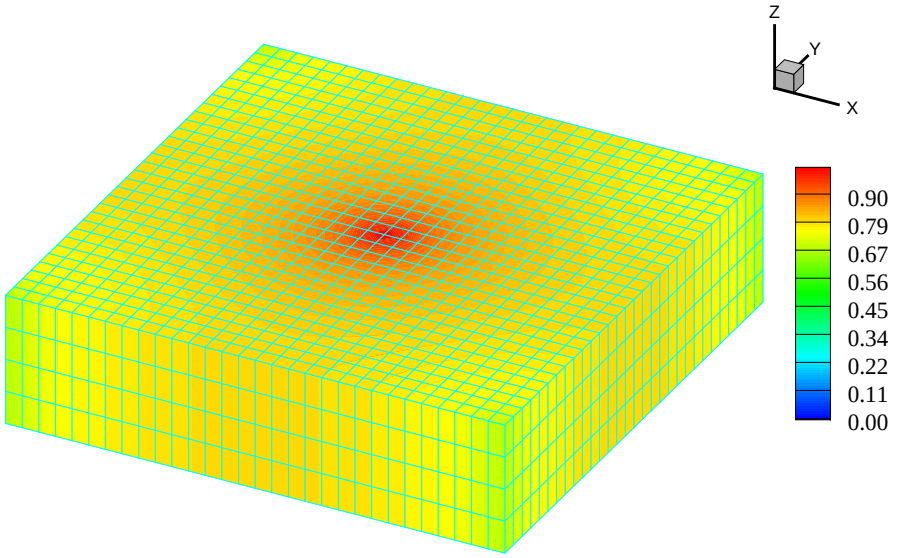

(b)

Fig. 5.44 Pore pressure in the reservoir at (a) 1 day and (b) 5 days.

Similarly, expansion of the reservoir due to the continuous fluid injection can be observed in **Fig. 5.45a and Fig. 5.45b** for 1 day and 5 days, respectively. The maximum expansion near to the injection well are of 3 mm and 1 cm after 1 day and 5 days, respectively.

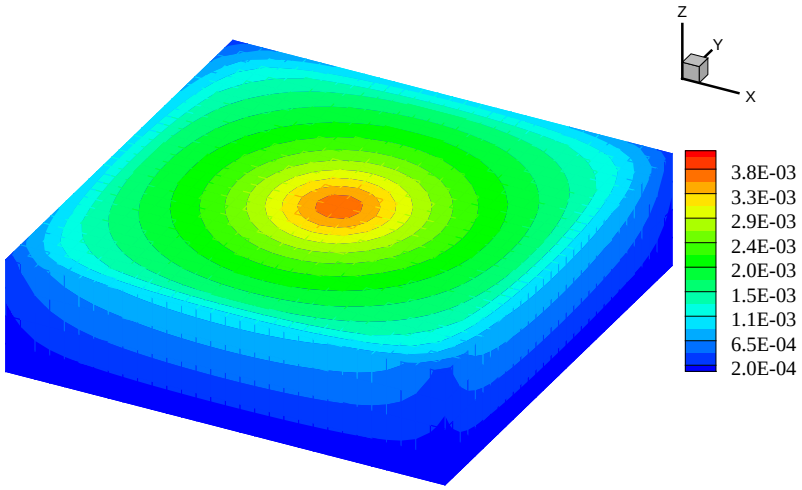

(a)

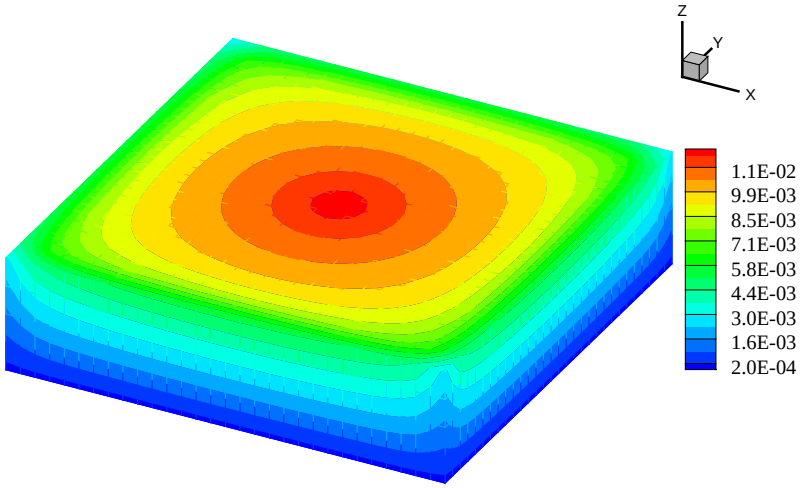

(b)

Fig. 5.45 Vertical displacement in the reservoir at (a) 1 day and (b) 5 days.

Next, the effects of stress redistribution in the overburden on reservoir stress state are computed.

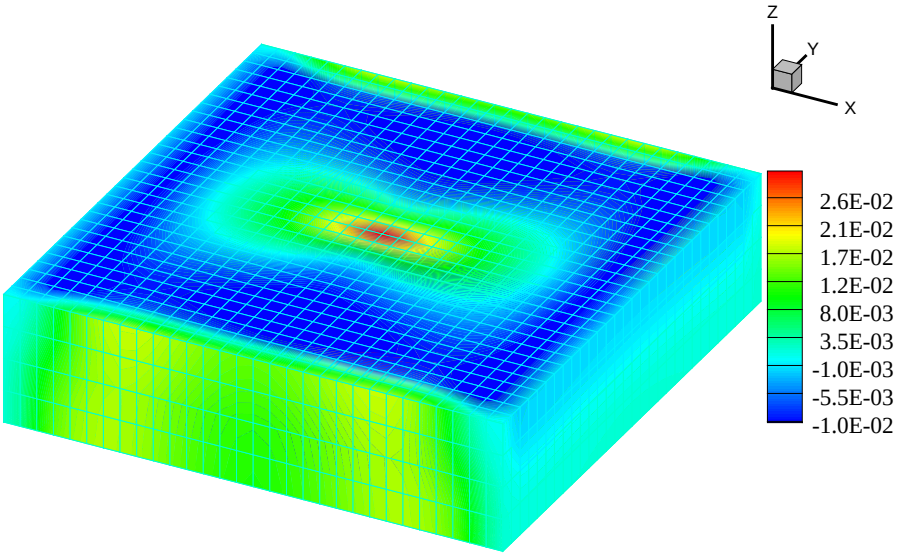

Fig. 5.46 Total stress (σ_{xx}) in the reservoir at 5 days.

After 5 days of operation, the induced stresses in the reservoir $(\sigma_{xx}, \sigma_{yy}$ and $\sigma_{zz})$ are shown in **Fig. 5.46, Fig. 5.47** and **Fig. 5.48**, respectively**.** The increase in fluid content near the injection well creates the high pore pressure, which causes the solid grains in the rock matrix to expand and thus the total stresses in the reservoir are less compressible or tensile in this example. Induced vertical stresses are of (60-180 KPa), whereas horizontal stresses are of (10-30 KPa).

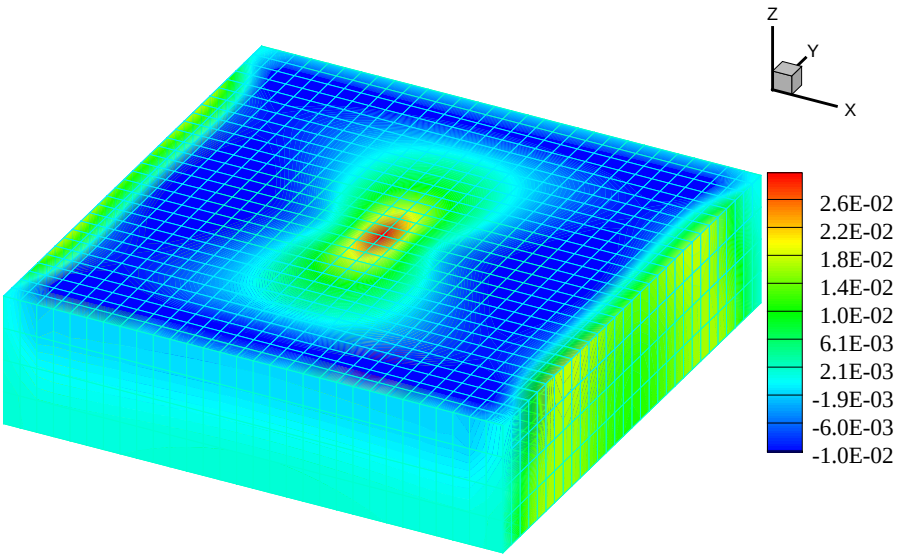

Fig. 5.47 Total stress (σ_{yy}) in the reservoir at 5 days.

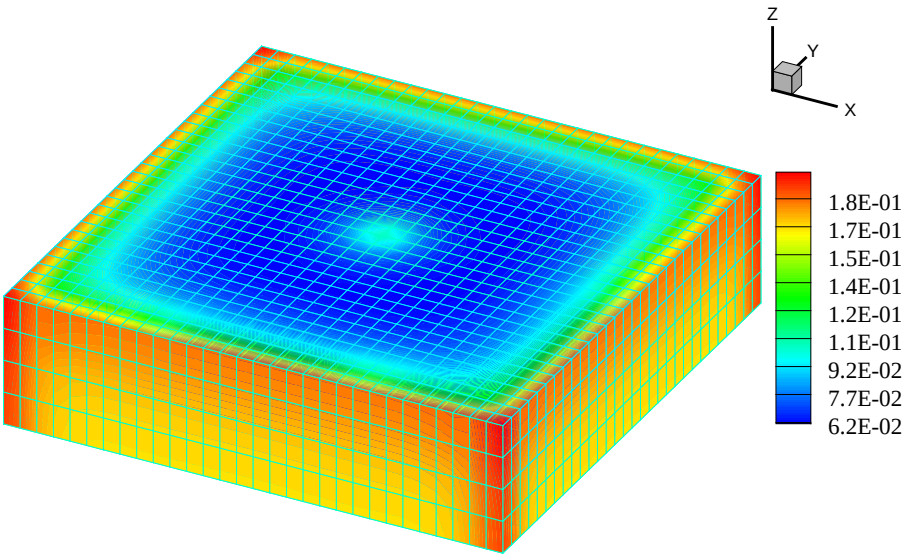

Fig. 5.48 Total stress (σ_{zz}) in the reservoir at 5 days.

5.4 Chapter Summary

In this section, we presented the applicability of the hybrid BEFEM model by analyzing series of numerical experiments. Examples of injection and extraction in the geothermal reservoir, hydraulic fracturing, and reservoir deformation and stresses due to injection and production are analyzed. The summary of the results from the numerical experiments is presented below.

1. Injecting undersaturated cold geothermal fluid causes large silica mass dissolution in the fracture zone that extends towards the extraction well, increasing fracture aperture with time in this zone.
2. During injection of supersaturated fluid, precipitation of silica in the fracture decreases the fracture aperture and it is more pronounced in areas of higher temperature (and thus reaction rate constant) and concentration gradient between rock and fluid. Therefore, fracture aperture change is non-uniform with bands of lower aperture behind the extraction well. The central cool zone has less silica precipitation because of slower silica reactivity at lower temperature. However, a significant amount (70%) of fracture width reduction due to silica precipitation is observed after one year of injection.
3. Thermo- and poroelastic stresses change the stress state in the reservoir matrix. The maximum normal tensile stress is induced at the injection well where the most cooling has occurred. However, it has observed that not only tensile stress develop due to cooling but also compressive stresses are induced outside of the

cooled zone. Thermoelastic effects have large impacts on fracture aperture than those compared to poroelastic effects.

4. Simulations that consider fracture stiffness heterogeneity show the development of a non-uniform flow path in the crack, with areas of higher joint normal stiffness showing lower aperture increase due to poro-thermoelasticity, while expansion of higher fracture aperture zone due to silica dissolution.
5. Due to induced large pore pressure during fluid injection in the reservoir, the compressive stresses are induced and are responsible for fracture closure.
6. Tensile thermal stresses are induced if the lower temperature fluid is injected into the hot reservoir, which reduce effective stresses responsible for the deformation of the reservoir.
7. Intense pore pressure increase during multiple hydraulic fracturing causes increases of tensile stresses at the fracture surface and shear failure around the main fracture.
8. The hybrid BEFEM model is successfully extended to incorporate the effects of induced overburden stresses on the injection and production procedures. The Mandel-Cryer effect is validated in current model by considering a single producing well in a reservoir. Reservoir deforms in expansion and stresses become less compressive in response to continuous injection.

6. SUMMARY AND CONCLUSIONS

6.1 Summary

Aspects of coupled rock deformation and thermo-poro-mechanical processes in the fractures have been described using the theory of thermo-poroelasticity. Thermoelasticity has incorporated considering theory of heat conduction. Reactive mineral transport in the fractures and mineral diffusion in the reservoir are also considered. The displacement discontinuity (DD) approach was adopted to define the boundary element formulation using the concept of source distribution and the principle of superposition. An integrated approach has implemented to represent the combined effects of the coupled processes in the reservoir.

A hybrid BEFEM model was then devised using the FEM and BEM to represent governing thermo-poro-mechanical processes in the fracture/fracture zone and reservoir. SUPG technique in FEM was adopted to solve convective transport. The DD method has implemented using three-dimensional DD and source solutions in poroelastic media. The hybrid BEFEM model has applied in problems of injection/extraction in the fracture, hydraulic fracturing and reservoir layer deformation.

6.2 Conclusions

The following conclusions are drawn from this study.

- Thermo-poro-mechanical processes in the fracture changes the fracture aperture (fracture conductivity) and influences the fluid flow.
- The stresses and pore pressure in the reservoir are changed in response to injection and production procedures. The predictions of stress and pore pressure in the reservoir are crucial in reservoir development and management works.
- Zones of intense rock failure can form near the fracture tips and surfaces, which is consistent with the field observations of micro-seismic events during hydraulic fracturing process. The pore pressure can play important role in areas away from the tip and contributes to slip.

The contribution resulting from this study is as follows:

- We developed an efficient model to consider thermo-poro-mechanical and mineral transport processes in the fracture-reservoir matrix system.
- We devised hybrid BEFEM model for coupled geomechanics and reservoir flow by considering single phase fluid flow in the reservoir and poroelastic deformation in overburden rock matrix.

REFERENCES

Abousleiman, Y., Cheng, A.H.-D., Cui, L., Detournay, E., and Roegiers, J.-C. 1996. Mandel's Problem Revisited. *Geotechnique* **46** (2): 187–195. doi: 10.1680/geot.1996.46.2.187.

Aboustit, B.L., Advani, S.H., Lee, J.K., and Sandhu, R.S. 1982. Finite Element Evaluations of Thermo-Elastic Consolidation. Paper presented at 23rd U.S. Symposium on Rock Mechanics, Berkeley, California, USA, 25–27 August.

Advani, S.H. and Lee, J.K. 1982. Finite Element Model Simulations Associated with Hydraulic Fracturing. *SPE Journal* **22** (2): 209–218. SPE-8941-PA. doi: 10.2118/8941-PA.

Archer, R. and Horne, R. 1998. Flow Simulation in Heterogeneous Reservoirs Using the Dual Reciprocity Boundary Element Method and the Green Element Method. Paper presented at ECMOR VI, Peebles, Scotland, 8–11 September.

Arnórsson, S. and Gudmundsson, B.T. 2003. Geochemical Monitoring of the Response of Geothermal Reservoirs to Production Load–Examples from Krafla, Iceland. Paper presented at International Geothermal Conference, Reykjavík, Iceland, 14–17 September.

Aziz, K. and Settari, A. 1979. *Petroleum Reservoir Simulation*, first edition. London and New York: Applied Science Publishers. ISBN 9780853347873.

Bagheri, M. and Settari, A. 2008. Modeling of Fluid Flow in Deformable Fractured Reservoirs Using Full Tensor Permeability. Paper SPE 113319 presented at Europec/EAGE Conference and Exhibition, Rome, Italy, 9–12 June. doi: 10.2118/113319-MS.

Bandis, S., Lumsden, A.C., and Barton, N.R. 1981. Experimental Studies of Scale Effects on the Shear Behaviour of Rock Joints. *International Journal of Rock Mechanics and Mining Sciences & Geomechanics Abstracts* **18** (1): 1–21. doi: 10.1016/0148-9062(81)90262-x.

Bandis, S.C., Lumsden, A.C., and Barton, N.R. 1983. Fundamentals of Rock Joint Deformation. *International Journal of Rock Mechanics and Mining Sciences & Geomechanics Abstracts* **20** (6): 249–268. doi: Doi: 10.1016/0148-9062(83)90595-8.

Banerjee, P.K. and Butterfield, R. 1981. *Boundary Element Methods in Engineering Science*. London: McGraw-Hill Book Co. (UK). ISBN 9780070841208.

Barenblatt, G.I. 1962. The Mathematical Theory of Equilibrium Cracks in Brittle Fracture. In *Advances in Applied Mechanics Vol 7*, ed. H.L. Dryden and T.v. Kármán, 55–129, Waltham, Massachusetts: Academic Press.

Barton, N., Bandis, S., and Bakhtar, K. 1985. Strength, Deformation and Conductivity Coupling of Rock Joints. *International Journal of Rock Mechanics and Mining Sciences & Geomechanics Abstracts* **22** (3): 121–140. doi: 10.1016/0148-9062(85)93227-9.

Barton, N.R. 1976. The Shear Strength of Rock and Rock Joints. *International Journal of Rock Mechanics and Mining Sciences & Geomechanics Abstracts* **13** (9): 255–279. doi: 10.1016/0148-9062(76)90003-6.

Barton, N.R. 1986. Deformation Phenomena in Jointed Rock. *Geotechnique* **36** (2): 147–167. doi: 10.1680/geot.1986.36.2.147.

Batchelor, G.K. 1967. *An Introduction to Fluid Dynamics*. Cambridge: Cambridge University Press. ISBN 9780521663960.

Becker, E.B., Carey, G.F., and Oden, J.T. 1981. *Finite Elements: An Introduction*. Upper Saddle River, New Jersey: Prentice-Hall. ISBN 9780133170573.

Biot, M.A. 1941. General Theory of Three-Dimensional Consolidation. *Journal of Applied Physics* **12** (2): 155–164.

Boone, T.J. and Detournay, E. 1990. Response of a Vertical Hydraulic Fracture Intersecting a Poroelastic Formation Bounded by Semi-Infinite Impermeable Elastic Layers. *International Journal of Rock Mechanics and Mining Sciences & Geomechanics Abstracts* **27** (3): 189–197. doi: 10.1016/0148-9062(90)94327-p.

Boone, T.J. and Ingraffea, A.R. 1990. A Numerical Procedure for Simulation of Hydraulically-Driven Fracture Propagation in Poroelastic Media. *International Journal for Numerical and Analytical Methods in Geomechanics* **14** (1): 27–47. doi: 10.1002/nag.1610140103.

Brebbia, C.A. and Dominguez, J. 1992. *Boundary Elements: An Introductory Course*. Berlin: Computational Mechanics. ISBN 9781853121609.

Brebbia, C.A., Telles, J.C.F., and Wrobel, L.C. 1984. *Boundary Element Techniques: Theory and Applications in Engineering*. Berlin: Springer-Verlag. ISBN 9783540124849.

Brooks, A.N. and Hughes, T.J.R. 1982. Streamline Upwind/Petrov-Galerkin Formulations for Convection Dominated Flows with Particular Emphasis on the Incompressible Navier-Stokes Equations. *Computer Methods in Applied Mechanics and Engineering* **32** (1–3): 199–259. doi: 10.1016/0045-7825(82)90071-8.

Carroll, S., Mroczek, E., Alai, M., and Ebert, M. 1998. Amorphous Silica Precipitation (60 to 120°C): Comparison of Laboratory and Field Rates. *Geochimica et Cosmochimica Acta* **62** (8): 1379–1396. doi: 10.1016/s0016-7037(98)00052-0.

Carvalho, J.L. 1990. Poroelastic Effects and Influence of Material Interfaces on Hydraulic Fracture Behaviour. PhD dissertation, University of Toronto, Toronto.

Chen, H.Y., Teufel, L.W., and Lee, R.L. 1995. Coupled Fluid Flow and Geomechanics 1.Theory and Governing Equations. Paper SPE 30752 presented at SPE Annual Technical Conference and Exhibition, Dallas, Texas, USA, 22–25 October. doi: 10.2118/30752-MS.

Chen, J. 1992. Fundamental Solutions and Boundary Element Formulations for Dynamic Problems of Poroelasticity and Thermoelasticity. PhD dissertation, State University of New York at Buffalo, New York.

Cheng, A.H.-D. and Detournay, E. 1988. Direct Boundary Element Method for Plane Strain Poroelasticity *International Journal for Numerical and Analytical Methods in Geomechanics* **12**: 551–572. doi: 10.1002/nag.1610120508.

Cheng, A.H.-D. and Detournay, E. 1998. On Singular Integral Equations and Fundamental Solutions of Poroelasticity. *International Journal of Solids and Structures* **35** (34–35): 4521–4555. doi: 10.1016/s0020-7683(98)00082-1.

Cheng, A.H.-D., Ghassemi, A., and Detournay, E. 2001. Integral Equation Solution of Heat Extraction from a Fracture in Hot Dry Rock. *International Journal for Numerical and Analytical Methods in Geomechanics* **25** (13): 1327–1338. doi: 10.1002/nag.182.

Cheng, A.H.-D. and Predeleanu, M. 1987. Transient Boundary Element Formulation for Linear Poroelasticity. *Applied Mathematical Modelling* **11** (4): 285–290. doi: 10.1016/0307-904x(87)90144-2.

Chin, L.Y., Raghavan, R., and Thomas, L.K. 1998. Fully-Coupled Geomechanics and Fluid-Flow Analysis of Wells with Stress-Dependent Permeability. Paper SPE 48857 presented at SPE International Oil and Gas Conference and Exhibition in China, Beijing, China, 2–6 November. doi: 10.2118/48857-MS.

Clifton, R.J. and Abou-Sayed, A.S. 1979. On the Computation of the Three-Dimensional Geometry of Hydraulic Fractures. Paper SPE 7943 presented at Symposium on Low Permeability Gas Reservoirs, Denver, Colorado, USA, 20–22 May. doi: 10.2118/7943-MS.

Clifton, R.J. and Abou-Sayed, A.S. 1981. A Variational Approach to the Prediction of the Three-Dimensional Geometery of Hydraulic Fractures. Paper SPE 9879 presented at SPE/DOE Low Permeability Gas Reservoirs Symposium, Denver, Colorado, USA, 27–29 May. doi: 10.2118/9879-MS.

Coats, K.H. 1982. Reservoir Simulation:State of the Art. *Journal of Petroleum Technology* **34** (8): 1633–1642. SPE-10020-PA. doi: 10.2118/10020-PA.

Coussy, O. 1989. A General Theory of Thermoporoelastoplasticity for Saturated Porous Materials. *Transport in Porous Media* **4**: 281–293. doi: 10.1007/BF00138040.

Crouch, S.L. and Starfield, A.M. 1983. *Boundary Element Methods in Solid Mechanics*, first edition. London: George Allen & Unwin. ISBN 0-04-620010-X.

Cryer, C.W. 1963. A Comparison of the Three-Dimensional Consolidation Theories of Biot and Terzaghi. *The Quarterly Journal of Mechanics and Applied Mathematics* **16** (4): 401–412. doi: 10.1093/qjmam/16.4.401.

Curran, J.H. and Carvalho, J.L. 1987. A Displacement Discontinuity Model for Fluid-Saturated Porous Media. Paper presented at 6th ISRM Congress, Montreal, Canada, 30 August–3 September.

Dargush, G.F. and Banerjee, P.K. 1989. A Time Domain Boundary Element Method for Poroelasticity. *International Journal for Numerical Methods in Engineering* **28** (10): 2423–2449. doi: 10.1002/nme.1620281014.

Dean, R.H., Gai, X., Stone, C.M., and Minkoff, S.E. 2003. A Comparison of Techniques for Coupling Porous Flow and Geomechanics *SPE Journal* **11** (1): 132–140. SPE-79709-PA. doi: 10.2118/79709-PA.

Detournay, E. 2004. Propagation Regimes of Fluid-Driven Fractures in Impermeable Rocks. *International Journal of Geomechanics* **4** (1): 35-45. doi: 10.1061/(asce)1532-3641(2004)4:1(35).

Detournay, E. and Cheng, A.H.-D. 1991. Plane Strain Analysis of a Stationary Hydraulic Fracture in a Poroelastic Medium. *International Journal of Solids and Structures* **27** (13): 1645–1662. doi: 10.1016/0020-7683(91)90067-p.

Detournay, E. and Cheng, A.H.-D. 1993. Fundamentals of Poroelasticity. In *Comprehensive Rock Engineering: Principles, Practice and Projects, Vol. Ii*, ed. C. Fairhurst, Chap. 5, 113–171, Oxford: Analysis and Design Method, Pergamon Press.

Detournay, E., McLennan, J.D., and Roegiers, J.-C. 1986. Poroelastic Concepts Explain Some of the Hydraulic Fracturing Mechanisms. Paper SPE 15262 presented at SPE Unconventional Gas Technology Symposium, Louisville, Kentucky, USA, 18–21 May. doi: 10.2118/15262-MS.

Dobson, P.F., Kneafsey, T.J., Sonnenthal, E.L., Spycher, N., and Apps, J.A. 2003. Experimental and Numerical Simulation of Dissolution and Precipitation: Implications for Fracture Sealing at Yucca Mountain, Nevada. *Journal of*

Contaminant Hydrology **62–63**: 459–476. doi: Doi: 10.1016/s0169-7722(02)00155-9.

Douglas, J.J. 1997. On the Numerical Simulation of Waterflooding of Heterogeneous Petroleum Reservoirs. *Computational Geosciences* **1** (2): 155–190.

Douglas , J.J., Dupont, T., and Rachford, H.H.J. 1969. The Application of Variational Methods to Waterflooding Problems. *Journal of Canadian Petroleum Technology* **8** (3): 79–85. 69-03-01. doi: 10.2118/69-03-01.

Edwards, H. and Chicago, I. 1951. Stress Concentrations around Spheroidal Inclusions and Cavities. *Journal of Applied Mechanics* **18**: 19–30. doi: 10.1115/1.3408494.

Fung, L.S.-K., Buchanan, L., and Wan, R.G. 1994. Coupled Geomechanical-Thermal Simulation for Deforming Heavy-Oil Reserviors. *Journal of Canadian Petroleum Technology* **33** (4): 22-28.

Fung, L.S.K. 1992. A Coupled Geomechanic-Multiphase Flow Model for Analysis of in Situ Recovery in Cohesionless Oil Sands. *Journal of Canadian Petroleum Technology* **31** (6): 56–67.

Gai, X., Sun, S., Wheeler, M.F., and Klie, H. 2005. Coupled Stress and Fluid Flow Using a Finite Element Method in a Commercial Reservoir Simulator Paper SPE 88616 presented at SPE Asia Pacific Oil and Gas Conference and Exhibition, Perth, Australia, 18–20 October. doi: 10.2118/88616-MS.

Gambolati, G. and Freeze, R.A. 1973. Mathematical Simulation of the Subsidence of Venice: 1. Theory. *Water Resources Research* **9** (3): 721–733. doi: 10.1029/WR009i003p00721.

Ge, J. and Ghassemi, A. 2008. Analysis of Failure Potential around a Hydraulic Fracture in Jointed Rock. Paper presented at 42nd U.S. Rock Mechanics Symposium, San Francisco, California, USA, 29 June–2 July.

Geertsma, J. 1966. Problems of Rock Mechanics in Petroleum Production Engineering. Paper presented at First Congress of International Society of Rock Mechanics, Lisbon, Portugal, 25 September–1 October.

Geertsma, J. and Klerk, F.d. 1969. A Rapid Method of Predicting Width and Extent of Hydraulically Induced Fractures. *SPE Journal of Petroleum Technology* **21** (12): 1571–1581. SPE-2458-PA. doi: 10.2118/2458-PA.

Ghassemi, A. 1996. Three-Dimensional Poroelastic Hydraulic Fracture Simulation Using the Displacement Discontinuity Method. PhD dissertation, The University of Oklahoma, Norman, Oklahoma.

Ghassemi, A. and Diek, A. 2003. Linear Chemo-Poroelasticity for Swelling Shales: Theory and Application. *Journal of Petroleum Science and Engineering* **38** (3-4): 199–212. doi: 10.1016/S0920-4105(03)00033-0.

Ghassemi, A. and Kumar, G.S. 2007. Changes in Fracture Aperture and Fluid Pressure Due to Thermal Stress and Silica Dissolution/Precipitation Induced by Heat Extraction from Subsurface Rocks. *Geothermics* **36** (2): 115–140. doi: 10.1016/j.geothermics.2006.10.001.

Ghassemi, A., Nygren, A., and Cheng, A. 2008. Effects of Heat Extraction on Fracture Aperture: A Poro–Thermoelastic Analysis. *Geothermics* **37** (5): 525–539. doi: 10.1016/j.geothermics.2008.06.001.

Ghassemi, A., Tarasovs, S., and Cheng, A.H.-D. 2003. An Integral Equation Solution for Three-Dimensional Heat Extraction from Planar Fracture in Hot Dry Rock. *International Journal for Numerical and Analytical Methods in Geomechanics* **27** (12): 989–1004. doi: 10.1002/nag.308.

Ghassemi, A., Tarasovs, S., and Cheng, A.H.-D. 2007. A 3-D Study of the Effects of Thermomechanical Loads on Fracture Slip in Enhanced Geothermal Reservoirs. *International Journal of Rock Mechanics and Mining Sciences* **44** (8): 1132–1148. doi: 10.1016/j.ijrmms.2007.07.016.

Ghassemi, A. and Zhang, Q. 2004. A Transient Fictitious Stress Boundary Element Method for Porothermoelastic Media. *Engineering Analysis with Boundary Elements* **28** (11): 1363–1373. doi: 10.1016/j.enganabound.2004.05.003.

Ghassemi, A. and Zhang, Q. 2006. Porothermoelastic Analysis of the Response of a Stationary Crack Using the Displacement Discontinuity Method. *Journal of*

Engineering Mechanics **132** (1): 26–33. doi: 10.1061/(asce)0733-9399(2006)132:1(26).

Ghassemi, A. and Zhou, X. 2011. A Three-Dimensional Thermo-Poroelastic Model for Fracture Response to Injection/Extraction in Enhanced Geothermal Systems. *Geothermics* **40** (1): 39–49. doi: 10.1016/j.geothermics.2010.12.001.

Gidley, J.L., Holditch, S.A., Nierode, D.E., and Veatch, R.W. 1989. *Recent Advances in Hydraulic Fracturing*. Spe Monograph Series Vol. 12: Society of Petroleum Engineers. ISBN 9781555630201.

Goodman, R.E. 1976. *Methods of Geological Engineering in Discontinuous Rocks*. San Francisco, California: West Publication Company. ISBN 9780829900668.

Griffith, A.A. 1921. The Phenomena of Rupture and Flow in Solids. *Philosophical Transactions of the Royal Society of London. Series A, Containing Papers of a Mathematical or Physical Character* **221**: 163–198.

Gringarten, A.C., JR., R., and J., H. 1973. The Use of Source and Green's Functions in Solving Unsteady-Flow Problems in Reservoirs. *SPE Journal* **3** (5): 285-296. SPE-3818-PA. doi: 10.2118/3818-PA.

Gui, P., Cunha, L.B., and Cunha, J.C. 2007. A Numerical Two-Phase Flow Model Coupling Reservoir and Multi-Segment Horizontal Well. Paper SPE 107989 presented at Rocky Mountain Oil & Gas Technology Symposium, Denver, Colorado, USA, 16–18 April. doi: 10.2118/107989-MS.

Guiggiani, M., Krishnasamy, G., Rudolphi, T.J., and Rizzo, F.J. 1992. A General Algorithm for the Numerical Solution of Hypersingular Boundary Integral Equations. *Journal of Applied Mechanics* **59** (3): 604–614. doi: 10.1115/1.2893766.

Gutierrez, M. and Lewis, R.W. 1998. The Role of Geomechanics in Reservoir Simulation. Paper SPE 47392 presented at SPE/ISRM Rock Mechanics in Petroleum Engineering, Trondheim, Norway, 8–10 July. doi: 10.2118/47392-MS.

Gutierrez, M., Lewis, R.W., and Masters, I. 2001. Petroleum Reservoir Simulation Coupling Fluid Flow and Geomechanics. *SPE Reservoir Evaluation & Engineering* **4** (3): 164-172. SPE-72095-PA. doi: 10.2118/72095-PA.

Heidug, W.K. and Wong, S.W. 1996. Hydration Swelling of Water-Absorbing Rocks: A Constitutive Model. *International Journal for Numerical and Analytical Methods in Geomechanics* **20** (6): 403–430. doi: 10.1002/(sici)1096-9853(199606)20:6<403::aid-nag832>3.0.co;2-7.

Huang, T.H., Chang, C.S., and Chao, C.Y. 2002. Experimental and Mathematical Modeling for Fracture of Rock Joint with Regular Asperities. *Engineering Fracture Mechanics* **69** (17): 1977–1996. doi: 10.1016/s0013-7944(02)00072-3.

Irwin, G.R. 1957. Analysis of Stresses and Strains near the End of a Crack Traversing a Plate. *Journal of Applied Mechanics* **24**: 361–364.

Jaeger, J.C., Cook, N.G.W., and Zimmerman, R.W. 2007. *Fundamentals of Rock Mechanics*. Hoboken, New Jersey: Blackwell Publication. ISBN 9780632057597.

Johnson, J.W., Knauss, K.G., Glassley, W.E., DeLoach, L.D., and Tompson, A.F.B. 1998. Reactive Transport Modeling of Plug-Flow Reactor Experiments: Quartz and Tuff Dissolution at 240°C. *Journal of Hydrology* **209** (1–4): 81–111. doi: 10.1016/s0022-1694(98)00159-0.

Jongkittinarukorn, K. and Tiab, D. 1998. Development of the Boundary Element Method for a Horizontal Well in Multilayer Reservoir. Paper SPE 39939 presented at SPE Rocky Mountain Regional/Low-Permeability Reservoirs Symposium, Denver, Colorado, USA, 5–8 April.

Kikani, J. and Horne, R. 1989. Application of Boundary Element Method to Reservoir Engineering Problems. *Journal of Petroleum Science and Engineering* **3** (3): 229–241. doi: 10.1016/0920-4105(89)90020-x.

Kikani, J. and Horne, R.N. 1992. Pressure-Transient Analysis of Arbitrarily Shaped Reservoirs with the Boundary-Element Method. *SPE Formation Evaluation* **7** (1): 53–60. SPE-18159-PA. doi: 10.2118/18159-PA.

Kikani, J. and Horne, R.N. 1993. Modeling Pressure-Transient Behavior of Sectionally Homogeneous Reservoirs by the Boundary-Element Method. *SPE Formation Evaluation* **8** (2): 145–152. SPE-19778-PA. doi: 10.2118/19778-PA.

Knott, J.F. 1973. *Fundamentals of Fracture Mechanics*. Hoboken, New Jersey: Wiley. ISBN 9780470495650.

Kohl, T., Evansi, K.F., Hopkirk, R.J., and Rybach, L. 1995. Coupled Hydraulic, Thermal and Mechanical Considerations for the Simulation of Hot Dry Rock Reservoirs. *Geothermics* **24** (3): 345–359. doi: 10.1016/0375-6505(95)00013-g.

Kohl, T. and Hopkirk, R.J. 1995. "Frac"—a Simulation Code for Forced Fluid Flow and Transport in Fractured, Porous Rock. *Geothermics* **24** (3): 333–343. doi: 10.1016/0375-6505(95)00012-f.

Kolditz, O. and Clauser, C. 1998. Numerical Simulation of Flow and Heat Transfer in Fractured Crystalline Rocks: Application to the Hot Dry Rock Site in Rosemanowes (U.K.). *Geothermics* **27** (1): 1–23. doi: 10.1016/s0375-6505(97)00021-7.

Koning, E.J.L. 1985. Fractured Water Injection Wells-Anlytical Modeling of Fracture Propagation. Paper SPE 14684 available from SPE, Richardson, Texas.

Koutsabeloulis, N.C. and Hope, S.A. 1996. Coupled Stress/Fluid/Thermal Multi-Phase Reservoir Simulation Studies Incorporating Rock Mechanics. Paper SPE 47393 presented at SPE/ISRM Rock Mechanics in Petroleum Engineering, Trondheim, Norway, 8–10 July. doi: 10.2118/47393-MS.

Krogstad, S. and Durlofsky, L.J. 2007. Multiscale Mixed-Finite-Element Modeling of Coupled Wellbore/near-Well Flow. Paper 106179 presented at SPE Reservoir Simulation Symposium, Houston, Texas, USA, 26–28 February. doi: 10.2118/106179-MS.

Kumar, G.S. and Ghassemi, A. 2005. Numerical Modeling of Non-Isothermal Quartz Dissolution/Precipitation in a Coupled Fracture–Matrix System. *Geothermics* **34** (4): 411–439. doi: 10.1016/j.geothermics.2005.04.003.

Kurashige, M. 1989. A Thermoelastic Theory of Fluid-Filled Porous Materials. *International Journal of Solids and Structures* **25** (9): 1039–1052. doi: 10.1016/0020-7683(89)90020-6.

Lewis, R.W., Majorana, C.E., and Schrefler, B.A. 1986. A Coupled Finite Element Model for the Consolidation of Nonisothermal Elastoplastic Porous Media. *Transport in Porous Media* **1** (2): 155–178. doi: 10.1007/bf00714690.

Lewis, R.W. and Schrefler, B.A. 1998. *The Finite Element Method in the Static and Dynamic Deformation and Consolidation of Porous Media*, second edition. Hoboken, New Jersey: John Wiley. ISBN 9780471928096.

Lewis, R.W., Schrefler, B.A., and Simoni, L. 1991. Coupling Versus Uncoupling in Soil Consolidation. *International Journal for Numerical and Analytical Methods in Geomechanics* **15**: 553–548. doi: 10.1002/nag.1610150803.

Li, X., Cui, L., and Roegiers, J.C. 1998. Thermoporoelastic Modelling of Wellbore Stability in Non-Hydrostatic Stress Field. *International Journal of Rock Mechanics and Mining Sciences* **35** (4–5). Paper No. 063. doi: 10.1016/s0148-9062(98)00079-5.

Li, X.L. and Zienkiewicz, O.C. 1992. Multiphase Flow in Deforming Porous Media and Finite Element Solutions. *Computers & structures* **45** (2): 211–227. doi: 10.1016/0045-7949(92)90405-O.

Liggett, J.A. and Liu, P.L.F. 1979. Unsteady Flow in Confined Aquifers: A Comparison of Two Boundary Integral Methods. *Water Resources Research* **15** (4): 861–866. doi: 10.1029/WR015i004p00861.

Liu, J., Sheng, J., Polak, A., Elsworth, D., Yasuhara, H., and Grader, A. 2006. A Fully-Coupled Hydrological–Mechanical–Chemical Model for Fracture Sealing and Preferential Opening. *International Journal of Rock Mechanics and Mining Sciences* **43** (1): 23–36. doi: 10.1016/j.ijrmms.2005.04.012.

Mandel, J. 1953. Consolidation Des Sols(Etude Mathematique). *Geotechnique* **3** (7): 287–299. doi: 10.1680/geot.1953.3.7.287.

Manning, C.E. 1994. The Solubility of Quartz in H2o in the Lower Crust and Upper Mantle. *Geochimica et Cosmochimica Acta* **58** (22): 4831–4839. doi: 10.1016/0016-7037(94)90214-3.

Martin, T. and Valkó, P. 2007. Hydraulic Fracture Design for Production Enhancement. In *Modern Fracturing: Enhancing Natural Gas Production*, ed. M.J. Economides and T. Martin, Chap. 4, 93–166, Houston, Texas: ET Publishing.

McTigue, D.F. 1986. Thermoelastic Response of Fluid-Saturated Porous Rock. *Journal of Geophysical Research* **91** (B9): 9533–9542. doi: 10.1029/JB091iB09p09533.

Mossop, A. 2001. Seismicity, Subsidence and Strain at the Geysers Geothermal Field. PhD dissertation, Stanford University, Stanford, California.

Norris, A. 1992. On the Correspondence between Poroelasticity and Thermoelasticity. *Journal of Applied Geophysics* **71** (3): 1138–1141. doi: 10.1063/1.351278.

Numbere, D.T. and Tiab, D. 1988. An Improved Streamline-Generating Technique That Uses the Boundary (Integral) Element Method. *SPE Reservoir Engineering* **3** (3): 1061–1068. SPE-15135-PA. doi: 10.2118/15135-PA.

Nygren, A. and Ghassemi, A. 2006. Poroelastic and Thermoelastic Effects of Injection into a Geothermal Reservoir. Paper presented at 41st U.S. Rock Mechanics Symposium, Golden, Colorado, USA, 17–21 June.

Osorio, J.G., Chen, H.-Y., and Teufel, L.W. 1999. Numerical Simulation of the Impact of Flow-Induced Geomechanical Response on the Productivity of Stress-Sensitive Reservoirs. Paper SPE 51929 presented at SPE Reservoir Simulation Symposium, Houston, Texas, USA, 14–17 February. doi: 10.2118/51929-MS.

Palciauskas, V.V. and Domenico, P.A. 1982. Characterization of Drained and Undrained Response of Thermally Loaded Repository Rocks. *Water Resources Research* **18** (2): 281–290. doi: 10.1029/WR018i002p00281.

Palmer, I.D., Moschovidis, Z.A., and Cameron, J.R. 2005. Coal Failure and Consequences for Coalbed Methane Wells. Paper 96872 presented at SPE

Annual Technical Conference and Exhibition, Dallas, Texas, USA, 9–12 October.

Palmer, I.D., Moschovidis, Z.A., and Cameron, J.R. 2007. Modeling Shear Failure and Stimulation of the Barnett Shale after Hydraulic Fracturing. Paper SPE 106113 presented at SPE Hydraulic Fracturing Technology Conference, College Station, Texas, USA, 29–31 January.

Pao, W.K.S. and Lewis, R.W. 2002. Three-Dimensional Finite Element Simulation of Three-Phase Flow in a Deforming Fissured Reservoir. *Computer Methods in Applied Mechanics and Engineering* **191** (23-24): 2631–2659. doi: 10.1016/s0045-7825(01)00420-0.

Pao, W.K.S., Lewis, R.W., and Masters, I. 2001. A Fully Coupled Hydro-Thermo-Poro-Mechanical Model for Black Oil Reservoir Simulation. *International Journal for Numerical and Analytical Methods in Geomechanics* **25**: 1229–1256. doi: 10.1002/nag.174.

Peaceman, D.W. 1977. *Fundamentals of Numerical Reservoir Simulation*. Amsterdam: Elsevier. ISBN 9780444416254.

Pecher, R. 1999. Boundary Element Simulation of Petroleum Reservoirs with Hydraulically Fractured Wells. PhD dissertation, University of Calgary, Calgary, Canada.

Perkins, T.K. and Gonzalez, J.A. 1985. The Effect of Thermoelastic Stresses on Injection Well Fracturing. *SPE Journal* **25** (1): 78–88. SPE-11332-PA. doi: 10.2118/11332-PA.

Pointing, D.K., Foster, B.A., Naccache, P.F., Nicholas, M.O., Pollard, R.K., Rae, J., Banks, D., and Walsh, S.K. 1983. An Efficient Fully Implicit Simulator. *SPE Journal* **23** (3): 544–552. SPE-11817-PA. doi: 10.2118/11817-PA.

Price, H.S., Cavendish, J.C., and Varga, R.S. 1968. Numerical Methods of Higher-Order Accuracy for Diffusion- Convection Equations. *SPE Journal* **8** (3): 293–303. SPE-1877-PA. doi: 10.2118/1877-PA.

Pruess, K. 1991. Tough2-a General-Purpose Numerical Simulator for Multiphase Fluid and Heat Flow. Berkely: Lawrence Berkeley Laboratory, LBL-29400.

Rawal, C. and Ghassemi, A. 2010a. A 3d Analysis of Rock Failure around a Hydraulic Fracture with Reference to Induced Seismicity. Paper presented at 34th Geothermal Research Council Annual Meeting, Sacramento, California, USA, 24–27 October.

Rawal, C. and Ghassemi, A. 2010b. Reactive Flow in a Natural Fracture in Poro-Thermo-Elastic Rock. Paper presented at 35th Workshop on Geothermal Reservoir Engineering, Stanford, California, USA, 1–3 February.

Rawal, C. and Ghassemi, A. 2010c. Reactive Transport in a Planar Fracture in Hot- and Poroelastic Rock. Paper 10-335 presented at 44th U.S. Rock Mechanics Symposium and 5th U.S.-Canada Rock Mechanics Symposium, Salt Lake City, Utah, USA, 27–30 June.

Reddy, J.N. 2006. *An Introduction to the Finite Element Method*. New York City, New York: McGraw-Hill Higher Education. ISBN 9780072466850.

Rice, J.R. 1968. Mathematical Anlysis in the Mechanics of Fracture. In *Fracture: An Advanced Treatise*, ed. H. Liebowitz, Chap. 3, 191–311, Waltham, Massachusetts: Mathematical Fundamentals, Academic Press.

Rice, J.R. and Cleary, M.P. 1976. Some Basic Stress Diffusion Solutions for Fluid-Saturated Elastic Porous Media with Compressible Constituents. *Reviews of Geophysics and Space Physics* **14** (2): 227–241. doi: 10.1029/RG014i002p00227.

Rimstidt, J.D. and Barnes, H.L. 1980. The Kinetics of Silica-Water Reactions. *Geochimica et Cosmochimica Acta* **44** (11): 1683–1699. doi: 10.1016/0016-7037(80)90220-3.

Robinson, B.A. 1982. Quartz Dissolution and Silica Deposition in Hot-Dry-Rock Geothermal Systems. MS thesis, Massachusetts Institute of Technology, Cambridge, Massachusetts.

Robinson, B.A. and Pendergrass, J. 1989. A Combined Heat Transfer and Quartz Dissolution/Deposition Model for a Hot Dry Rock Geothermal Reservoir. Paper presented at 14th Stanford Geothermal Workshop Stanford, California, USA, 24–26 January.

Roegiers, J.-C. and Zhao, X.L. 1991. Rock Fracture Tests in Simulated Downhole Conditions. Paper 91-221 presented at 32nd U.S. Symposium on Rock Mechanics, Norman, Oklahoma, USA, 10–12 July.

Rutqvist, J., Borgesson, L., Chijimatsu, M., Kobayashi, A., Jing, L., Nguyen, T.S., Noorishad, J., and Tsang, C.-F. 2001. Thermohydromechanics of Partially Saturated Geological Media: Governing Equations and Formulation of Four Finite Element Models. *International Journal of Rock Mechanics and Mining Sciences* **38**: 105–127. doi: 10.1016/S1365-1609(00)00068-X.

Rutqvist, J., Majer, E., Oldenburg, C., Peterson, J., and Vasco, D. 2006. Integrated Modeling and Field Study of Potential Mechanisms Forinduced Seismicity at the Geysers Goethermal Field, California. Paper LBNL-60939 presented at Geothermal Resources Council Annual Meeting, San Diego, California, USA, 9–13 September.

Samardzioska, T. 2009. Boundary Elements for Modeling Fractured Porous Media: Single and Two Phase Flow and Transport. Paper presented at International Symposium on Water Management and Hydraulic Engineering, Ohrid, Macedonia, 1–5 September.

Sandhu, R.S. and Wilson, E.L. 1969. Finite Element Analysis of Seepage in Elastic Medium. *Journal of the Engineering Mechanics Division* **95** (3): 641–652.

Sekine, H. and Mura, T. 1980. Characterization of a Penny-Shaped Reservoir in a Hot Dry Rock. *Journal of Geophysical Research* **85** (B7): 3811–3816. doi: 10.1029/JB085iB07p03811.

Settari, A. and Mourits, F.M. 1998. A Coupled Reservoir and Geomechanical Simulation System. *SPE Journal* **3** (3): 219–226. SPE-50939-PA. doi: 10.2118/50939-PA.

Settari, A., Price, H.S., and Dupont, T. 1977. Development and Application of Variational Methods for Simulation of Miscible Displacement in Porous Media. *SPE Journal* **17** (3): 228–246. SPE-5721-PA. doi: 10.2118/5721-PA.

Settari, A. and Walters, D.A. 2001. Advances in Coupled Geomechanical and Reservoir Modeling with Applications to Reservoir Compaction. *SPE Journal* **6** (3). SPE-74142-PA. doi: 10.2118/74142-PA.

Skempton, A.W. 1954. The Pore Pressure Coefficients a and B. *Geotechnique* **4** (4): 143–147. doi: 10.1680/geot.1954.4.4.143.

Small, J.C., Booker, J.R., and Davis, E.H. 1976. Elasto-Plastic Consolidation of Soil. *International Journal of Solids and Structures* **12** (6): 431–448. doi: 10.1016/0020-7683(76)90020-2.

Smith, I.M. and Griffiths, D.V. 1998. *Programming the Finite Element Method*, third edition. Hoboken, New Jersey: Wiley. ISBN 9780470849699.

Sneddon, I.N. 1946. The Distribution of Stress in the Neighbourhood of a Crack in an Elastic Solid. *Proceedings of the Royal Society of London. Series A, Mathematical and Physical Sciences* **187** (1009): 229–260.

Steefel, C.I. and Lichtner, P.C. 1998. Multicomponent Reactive Transport in Discrete Fractures: I. Controls on Reaction Front Geometry. *Journal of Hydrology* **209** (1–4): 186–199. doi: 10.1016/S0022-1694(98)00146-2.

Stroud, A.H. and Secrest, D. 1966. *Gaussian Quadrature Formulas*. Upper Saddle River, New Jersey: Prentice-Hall. ISBN B0006BNRQ2.

Sukirman, Y. and Lewis, R.W. 1993. A Finite Element Solution of a Fully Coupled Implicit Formulation for Reservoir Simulation. *International Journal for Numerical and Analytical Methods in Geomechanics* **17** (10): 677–698. doi: 10.1002/nag.1610171002.

Suzuki, I. and Morita, N. 2004. Subsidence and Horizontal Earth Surface Movement During Reservoir Depletion for 3d Reservoirs with 3d Earth Surface. Paper SPE

89960 presented at SPE Annual Technical Conference and Exhibition, Houston, Texas, USA, 26–29 September doi: 10.2118/89960-MS.

Tang, D.H., Frind, E.O., and Sudicky, E.A. 1981. Contaminant Transport in Fractured Porous Media: Analytical Solution for a Single Fracture. *Water Resources Research* **17** (3): 555–564. doi: 10.1029/WR017i003p00555.

Taron, J. and Elsworth, D. 2009. Thermal-Hydrologic-Mechanical-Chemical Processes in the Evolution of Engineered Geothermal Reservoirs. *International Journal of Rock Mechanics and Mining Sciences* **46** (5): 855–864. doi: 10.1016/j.ijrmms.2009.01.007.

Terzaghi, K. 1923. Die Berechnung Der Durchlassigkeitsziffer Des Tones Aus Dem Verlauf Der Hydrodynamischen Spannungserscheinungen. *Sitzurnber Akad. Wiss. Wien* **132**: 105–124.

Thomas, L.K., Chin, L.Y., Pierson, R.G., and Sylte, J.E. 2003. Coupled Geomechanics and Reservoir Simulation. *SPE Journal* **8** (4). SPE-87339-PA. doi: 10.2118/87339-PA.

Tortike, W.S. and Ali, S.M.F. 1993. Reservoir Simulation Integrated with Geomechanics. *Journal of Canadian Petroleum Technology* **32** (5). 93-05-02. doi: 10.2118/93-05-02.

Tran, D., Settar, A., and Nghiem, L. 2002. New Iterative Coupling between a Reservoir Simulator and a Geomechanics Module. Paper 78192 presented at SPE/ISRM Rock Mechanics Conference, Irving, Texas, USA, 20–23 October. doi: 10.2118/78192-MS.

Valkó, P. and Economides, M.J. 1995. *Hydraulic Fracture Mechanics*. Hoboken, New Jersey: Wiley. ISBN 9780471956648.

Vandamme, L. and Curran, J.H. 1989. A Three-Dimensional Hydraulic Fracturing Simulator. *International Journal for Numerical Methods in Engineering* **28** (4): 909–927. doi: 10.1002/nme.1620280413.

Vandamme, L., Detournay, E., and Cheng, A.H.-D. 1989. A Two-Dimensional Poroelastic Displacement Discontinuity Method for Hydraulic Fracture Simulation. *International Journal for Numerical and Analytical Methods in Geomechanics* **13** (2): 215–224. doi: 10.1002/nag.1610130209.

Vandamme, L., Jeffrey, R.G., and Curran, J.H. 1988. Pressure Distribution in Three-Dimensional Hydraulic Fractures. *SPE Production Engineering* **3** (2): 181–186. SPE-15265-PA. doi: 10.2118/15265-PA.

Vandamme, L.M.P. 1986. A Three-Dimensional Displacement Discontinuity Model for the Analysis of Hydraulically Propagated Fractures. PhD dissertation, University of Toronto, Toronto, Ontario, Canada.

Verruijt, A. 1969. Elastic Storage of Aquifers. In *Flow through Porous Media*, ed. R.J.M. DeWiest and J. Bear, Chap. 8, 331–376, Waltham, Massachusetts: Academic Press.

Wangen, M. and Munz, I.A. 2004. Formation of Quartz Veins by Local Dissolution and Transport of Silica. *Chemical Geology* **209** (3-4): 179–192. doi: 10.1016/j.chemgeo.2004.02.011.

Warpinski, N.R., Wolhart, S.L., and Wright, C.A. 2001. Analysis and Prediction of Microseismicity Induced by Hydraulic Fracturing. Paper SPE 71649 presented at SPE Annual Technical Conference and Exhibition, New Orleans, Louisiana, USA, 30 September–3 October.

Wells, J.T. and Ghiorso, M.S. 1991. Coupled Fluid Flow and Reaction in Mid-Ocean Ridge Hydrothermal Systems: The Behavior of Silica. *Geochimica et Cosmochimica Acta* **55** (9): 2467–2481. doi: 10.1016/0016-7037(91)90366-d.

Witherspoon, P.A., Wang, J.S.Y., Iwai, K., and Gale, J.E. 1980. Validity of Cubic Law for Fluid Flow in a Deformable Rock Fracture. *Water Resources Research* **16** (6): 1016–1024. doi: 10.1029/WR016i006p01016.

Wood, W.L. and Lewis, R.W. 1975. A Comparison of Time Marching Schemes for the Transient Heat Conduction Equation. *International Journal for Numerical Methods in Engineering* **9** (3): 679–689. doi: 10.1002/nme.1620090314.

Xu, T. and Pruess, K. 1998. Coupled Modeling of Non-Isothermal Multiphase Flow, Solute Transport and Reactive Chemistry in Porous and Fractured Media: 1. Model Development and Validation. Berkeley: University of California, LBNL-42050.

Xu, T. and Pruess, K. 2001. Modeling Multiphase Non-Isothermal Fluid Flow and Reactive Geochemical Transport in Variably Saturated Fractured Rocks: 1. Methodology. *American Journal of Science* **301** (1): 16–33.

Yale, D.P. 2002. Coupled Geomechanics-Fluid Flow Modeling:Effects of Plasticity and Permeability Alteration. Paper 78202 presented at SPE/ISRM Rock Mechanics Conference, Irving, Texas, USA, 20–23 October. doi: 10.2118/78202-MS.

Yamamoto, K., Shimamoto, T., and Sukemura, S. 2004. Multiple Fracture Propagation Model for a Three-Dimensional Hydraulic Fracturing Simulator. *International Journal of Geomechanics* **4** (1): 46–57. doi: 10.1061/(asce)1532-3641(2004)4:1(46).

Yariv, S. and Cross, H. 1979. *Geochemistry of Colloid Systems for Earth Scientists*. Berlin: Springer-Verlag. ISBN 9783540089803.

Yasuhara, H. and Elsworth, D. 2006. A Numerical Model Simulating Reactive Transport and Evolution of Fracture Permeability. *International Journal for Numerical and Analytical Methods in Geomechanics* **30** (10): 1039–1062. doi: 10.1002/nag.513.

Yew, C.H. 1997. *Mechanics of Hydraulic Fracturing*, first edition. Houston, Texas: Gulf Publishing. ISBN 9780884154747.

Yew, C.H. and Liu, G.H. 1993. The Fracture Tip and Critical Stress Intensity Factor of a Hydraulically Induced Fracture. *SPE Production & Operations* **8** (3): 171-177. SPE-22875-PA. doi: 10.2118/22875-PA.

Yin, S., Dusseault, M.B., and Rothenburg, L. 2010. Fully Coupled Numerical Modeling of Ground Surface Uplift in Steam Injection. *Journal of Canadian Petroleum Technology* **49** (1): 16–21. SPE-132755-PA. doi: 10.2118/132755-PA.

Zhou, X.X., Ghassemi, A., and Cheng, A.H.-D. 2009. A Three-Dimensional Integral Equation Model for Calculating Poro- and Thermoelastic Stresses Induced by Cold Water Injection into a Geothermal Reservoir. *International Journal for Numerical and Analytical Methods in Geomechanics* **33** (14): 1613–1640. doi: 10.1002/nag.780.

Zienkiewicz, O.C. 1976. The Finite Element Method and the Solution of Some Geophysical Problems. *Philosophical Transactions of the Royal Society of London. Series A, Mathematical and Physical Sciences* **283** (1312): 139–151.

Zienkiewicz, O.C. 1984. Coupled Problems and Their Numerical Solution. In *Numerical Methods in Coupled Systems*, ed. R.W. Lewis, P. Bettess, and E. Hinton, 35–58, Chichester: Wiley & Sons.

Zienkiewicz, O.C. and Taylor, R.L. 1991. *The Finite Element Method*, fourth edition. New York City, New York: McGraw-Hill International. ISBN 0070841756.

Zienkiewicz, O.C. and Taylor, R.L. 2000. *Finite Element Method, Volume 1: The Basis*, fifth edition. Amsterdam: Butterworth-Heinemann. ISBN 978-0-7506-5049-6.

Zimmerman, R.W. and Bodvarsson, G.S. 1996. Hydraulic Conductivity of Rock Fractures. *Transport in Porous Media* **23** (1): 1–30. doi: 10.1007/bf00145263.

APPENDIX A

DERIVATION OF CUBIC LAW

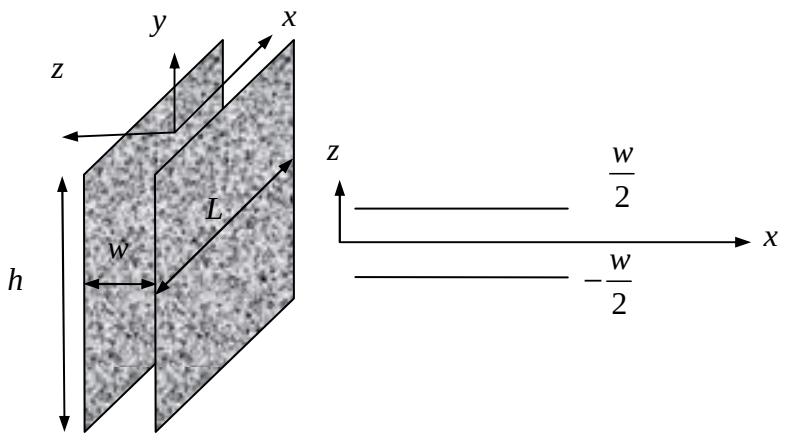

Fig. A.1 Idealized geometry of flow between parallel plates.

Consider laminar flow of Newtonian fluid between smooth parallel plates, the governing Navier-Stokes equation can be written as:

$$\rho_F\left(\frac{\partial}{\partial t}+u\frac{\partial}{\partial x}+v\frac{\partial}{\partial y}+w\frac{\partial}{\partial z}\right)\mathbf{v}=\rho_F\mathbf{F}-\nabla p+\mu\nabla^2\mathbf{v}+(\mu+\lambda)\nabla(\nabla.\mathbf{v})\ldots\ldots\ldots\ldots\ldots\ldots\ldots\ldots(A.1)$$

where $\nabla.$, ∇ and ∇^2 are the divergence, gradient and Laplacian operator respectively. Similarly, ρ_F is fluid density and u, v, w are the components of velocity $\mathbf{v}$ in x-, y- and z- direction respectively. $\mathbf{F}$ is body force vector, μ is the viscosity of the fluid and λ is the second viscosity coefficient.

For incompressible flow, Eq. A.1 can be simplified, as μ=constant, λ = 0 and mass continuity $\nabla.\mathbf{v} = 0$. Therefore, it yields:

$$\left(\frac{\partial}{\partial t}+u\frac{\partial}{\partial x}+v\frac{\partial}{\partial y}+w\frac{\partial}{\partial z}\right)\mathbf{v}=\mathbf{F}-\frac{1}{\rho_F}\nabla p+\frac{\mu}{\rho_F}\nabla^2\mathbf{v} \quad \text{.....(A.2)}$$

The body force term can be considered as gravity and can be removed from Eq. A.2, by defining a reduced pressure:

$$P = p+\rho_F gz \quad \text{.....(A.3)}$$

Therefore,

$$\mathbf{F}-\frac{1}{\rho_F}\nabla p=-g\mathbf{e}_z-\frac{1}{\rho_F}\nabla p=-\frac{1}{\rho_F}\left(\rho_F g\mathbf{e}_z+\nabla p\right)=-\frac{1}{\rho_F}\nabla\left(p+\rho_F gz\right)=-\frac{1}{\rho_F}\nabla P \quad \text{....(A.4)}$$

Using steady-state flow and inserting Eq. A.4 into Eq. A.2 it yields;

$$\left(u\frac{\partial}{\partial x}+v\frac{\partial}{\partial y}+w\frac{\partial}{\partial z}\right)\mathbf{v}=\frac{\mu}{\rho_F}\nabla^2\mathbf{v}-\frac{1}{\rho_F}\nabla P \quad \text{.....(A.5)}$$

In the plane of fracture, velocity will have no z-component since w vanishes at the two walls of fracture $\left(\pm\frac{w}{2}\right)$. Similarly, the velocity components do not vary with x or y, therefore, $\left(\frac{\partial u}{\partial x}=\frac{\partial u}{\partial y}=\frac{\partial v}{\partial x}=\frac{\partial v}{\partial y}=0\right)$. Eq. A.5 yields;

$$\nabla P=\mu\nabla^2\mathbf{v}(z) \quad \text{.....(A.6)}$$

The gradient and Laplacian in Eq. A.6 can be simplified as

$$\nabla P=\left(\frac{\partial P}{\partial x},\frac{\partial P}{\partial y},\frac{\partial P}{\partial z}\right)=\left(\frac{\partial P}{\partial x},\frac{\partial P}{\partial y},0\right)$$
$$\nabla^2\mathbf{v}(z)=\left(\nabla^2u(z),\nabla^2v(z),\nabla^2w(z)\right)=\left(\frac{\partial^2u}{\partial z^2},\frac{\partial^2v}{\partial z^2},0\right) \quad \text{.....(A.7)}$$

Applying Eq. A.7 into Eq. A.6, it yields two equations as:

$$\frac{\partial P}{\partial x} = \mu \frac{\partial^2 u(z)}{\partial z^2}$$
$$\frac{\partial P}{\partial y} = \mu \frac{\partial^2 v(z)}{\partial z^2} \quad \text{……..……..…(A.8)}$$

To solve equations in Eq. A.8, two boundary conditions are necessary. For this, the symmetric assumptions and zero velocity at the fracture walls are used as the boundary conditions:

$$\left.\frac{\partial u}{\partial z}\right|_{z=0} = \left.\frac{\partial v}{\partial z}\right|_{z=0} = 0$$
$$u|_{z=\pm w/2} = v_{z=\pm w/2} = 0 \quad \text{…….(A.9)}$$

Each equation in Eq. A.8 is integrated twice with respect to z and using respective boundary conditions from Eq. A.9, we get:

$$u(z) = \frac{1}{2\mu}\left(z^2 - \frac{w^2}{4}\right)\frac{\partial P}{\partial x}$$
$$v(z) = \frac{1}{2\mu}\left(z^2 - \frac{w^2}{4}\right)\frac{\partial P}{\partial y} \quad \text{……..(A.10)}$$

The flux through the fracture in x- and y-direction can be computed by integrating the velocity across the fracture from $z = -\frac{w}{2}$ to $z = \frac{w}{2}$

$$q_x = \int_{-w/2}^{w/2} u(z)\,dz = \frac{1}{2\mu}\frac{\partial P}{\partial x}\int_{-w/2}^{w/2}\left(z^2 - \frac{w^2}{4}\right)dz = \frac{w^3}{12\mu}\frac{\partial P}{\partial x}$$
$$q_y = \int_{-w/2}^{w/2} u(z)\,dz = \frac{1}{2\mu}\frac{\partial P}{\partial y}\int_{-w/2}^{w/2}\left(z^2 - \frac{w^2}{4}\right)dz = \frac{w^3}{12\mu}\frac{\partial P}{\partial y} \quad \text{…….……...(A11)}$$

$$\text{or, } \nabla p(x, y, 0, t) = -\frac{12\mu}{w^3(x, y, t)}\mathbf{q}(x, y, t) \quad \text{……...(A12)}$$

APPENDIX B

DERIVATION OF FLUID CONTINUITY EQUATION IN THE FRACTURE

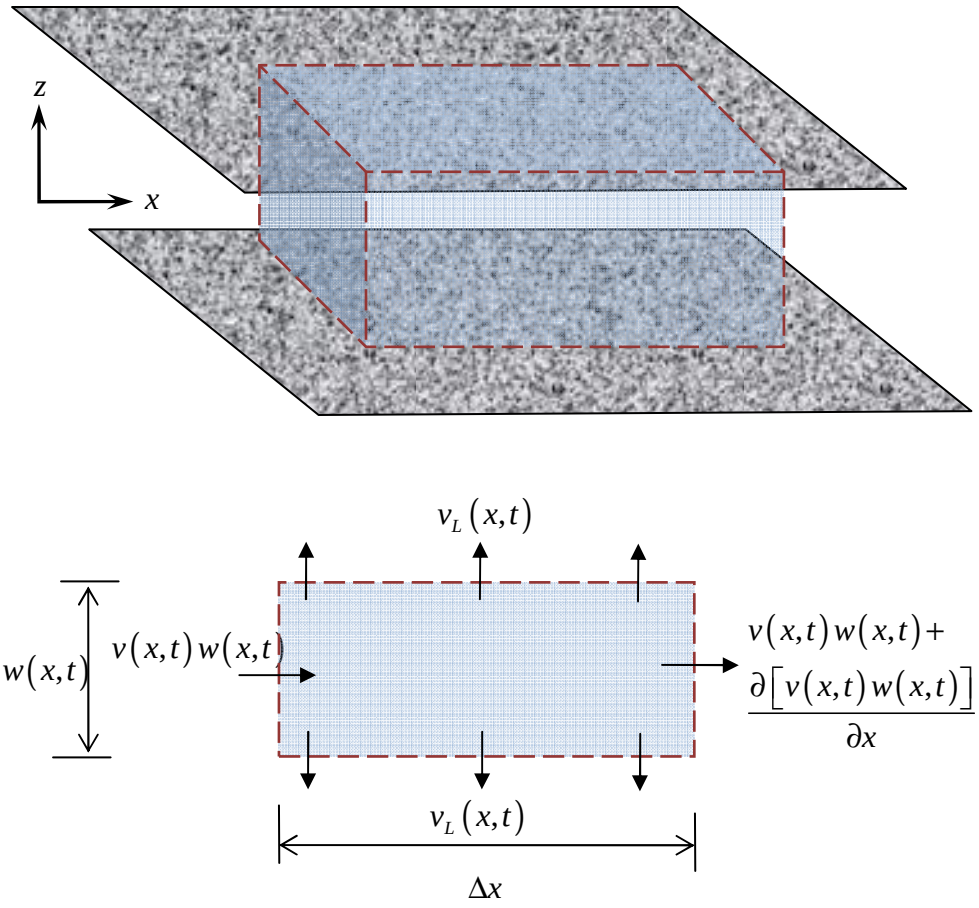

Fig. B.1 Representative elementary volume for mass balance in the fracture.

Assumptions:

1. Single phase fluid, incompressible fluid flow

2. Flow is laminar and Darcy's law is applicable

3. Width of the fracture is much smaller than its length

4. Transport along the fracture is much faster than transport within the reservoir

Considering the above assumptions and the representative volume of fracture as shown in **Fig. B.1,** the continuity equation is derived using the law of mass conservation as:

Mass In –Mass Out = Accumulation of Mass in control volume……..…..….(B.1)

where

Mass In = $\rho_F v(x,t)\, w(x,t) \times 1$ ……...…….…….(B.2)

Mass Out = $\rho_F v(x,t)\, w(x,t) \times 1 + \dfrac{\partial\left[\rho_F v(x,t)\, w(x,t)\right]}{\partial x} \times 1 \times \Delta x + 2\rho_F v_L(x,t) \times \Delta x \times 1$

Accumulation of mass in control volume= $\rho_F \dfrac{\Delta w(x,t)}{\Delta t} \times \Delta x \times 1$ ……..……..(B.3)

where ρ_F is the fluid density, v is the velocity of the fluid in the fracture, w is the fracture aperture, q is the fluid flux and v_L fluid leak-off velocity.

For an incompressible fluid, conservation of mass is equivalent to conservation of volume, therefore substituting Eqs. B.2 and B.3 into Eq. B.1 and canceling terms yields:

$$-\frac{\partial q(x,t)}{\partial x} - 2v_L(x,t) = \frac{\partial w(x,t)}{\partial t}$$ ……..……..(B.4)

where fluid flus is related to the velocity and fracture aperture as $q(x,t) = v(x,t)\, w(x,t)$

Similarly, Eq. B.4 can be written in two dimensions as:

$$-\nabla \cdot \mathbf{q}(x,y,t) - 2v_L(x,y,t) = \frac{\partial w(x,y,t)}{\partial t}$$ ……...……..…(B.5)

APPENDIX C

DERIVATION OF HEAT TRANSFER EQUATION IN THE FRACTURE

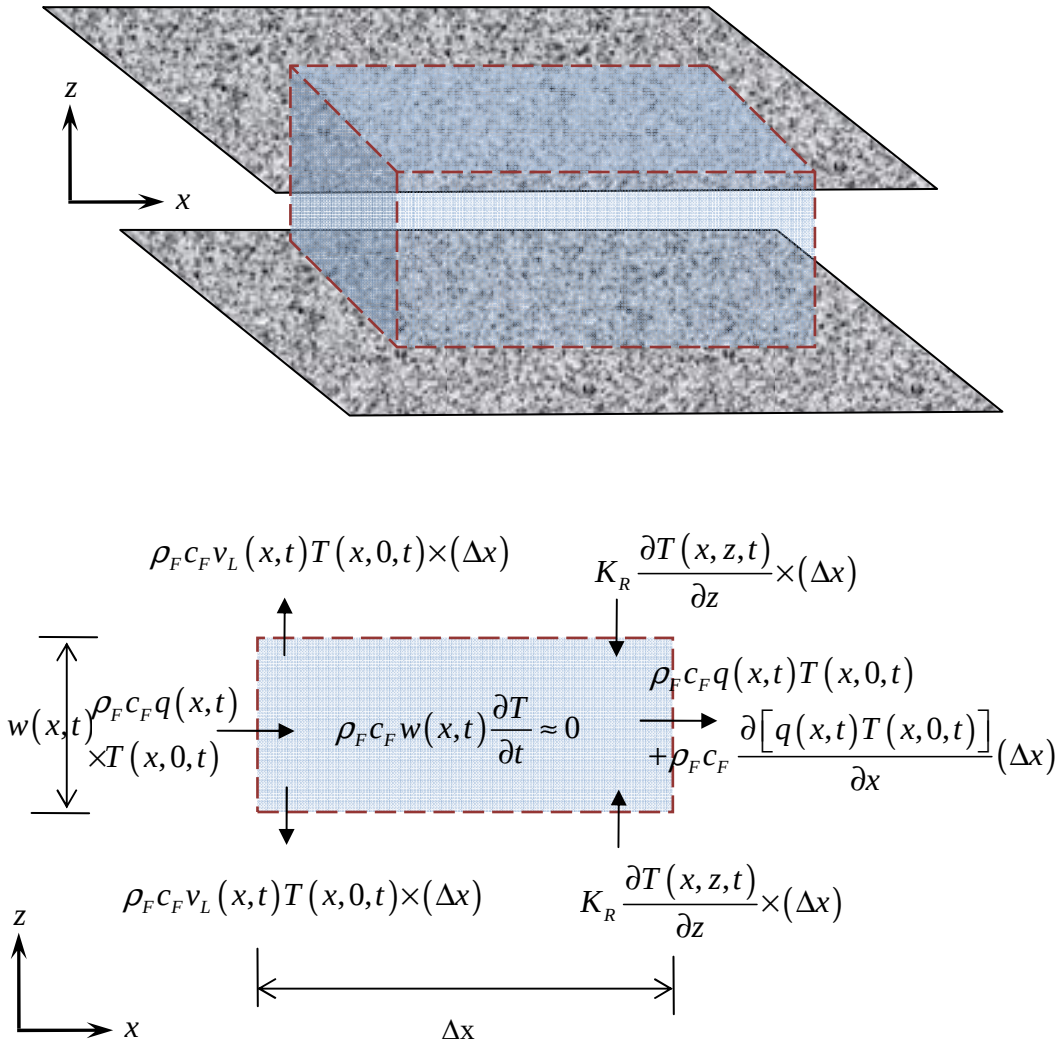

Fig. C.1 Representative elementary volume for heat balance in the fracture.

Assumptions:

1. Single phase fluid, incompressible fluid flow
2. Flow is steady and laminar; Darcy's law is applicable
3. Width of the fracture is much smaller than its length.
4. Thermal properties of the fluid and rock are constant.
5. Heat storage and dispersion in the fracture are negligible

With the above assumptions, by considering the heat balance over a fracture segment as shown in **Fig. C.1,** we can write heat transport equation as:

$$-\rho_F c_F \frac{\partial\left[q(x,t)T(x,0,t)\right]}{\partial x} - 2\rho_F c_F v_L(x,t)T(x,0,t) - \rho_F c_F \frac{\partial w(x,t)}{\partial t}T(x,0,t) + 2K_R \left.\frac{\partial T(x,z,t)}{\partial z}\right|_{z=0} = 0 \quad \text{.....(C.1)}$$

in which ρ_F is the fluid density, c_F is the specific heat of the fluid, and K_R is the rock thermal conductivity. As derived in Appendix B, the continuity of fluid in the fracture is:

$$-\frac{\partial q(x,t)}{\partial x} - 2v_L(x,t) = \frac{\partial w(x,t)}{\partial t} \quad \text{.....(C.2)}$$

Substituting the fluid continuity equation (Eq. C.2) into Eq. C.1 and simplifying it, the heat transport equation in the fracture is obtained:

$$-\rho_F c_F q(x,t)\frac{\partial T(x,0,t)}{\partial x} = 2K_R \left.\frac{\partial T(x,z,t)}{\partial z}\right|_{z=0} \quad \text{.....(C.3)}$$

and in two dimensions, it becomes:

$$\rho_F c_F \mathbf{q}(x,y).\nabla T\left(x,y,0,t\right)+q_H\left(x,y,0,t\right)=0 \quad \text{.....(C.4)}$$

where,

$$q_H\left(x,y,0,t\right)=-2K_R\left.\frac{\partial T\left(x,y,z,t\right)}{\partial z}\right|_{z=0}$$

APPENDIX D

DERIVATION OF SOLUTE TRANSPORT EQUATION IN THE FRACTURE

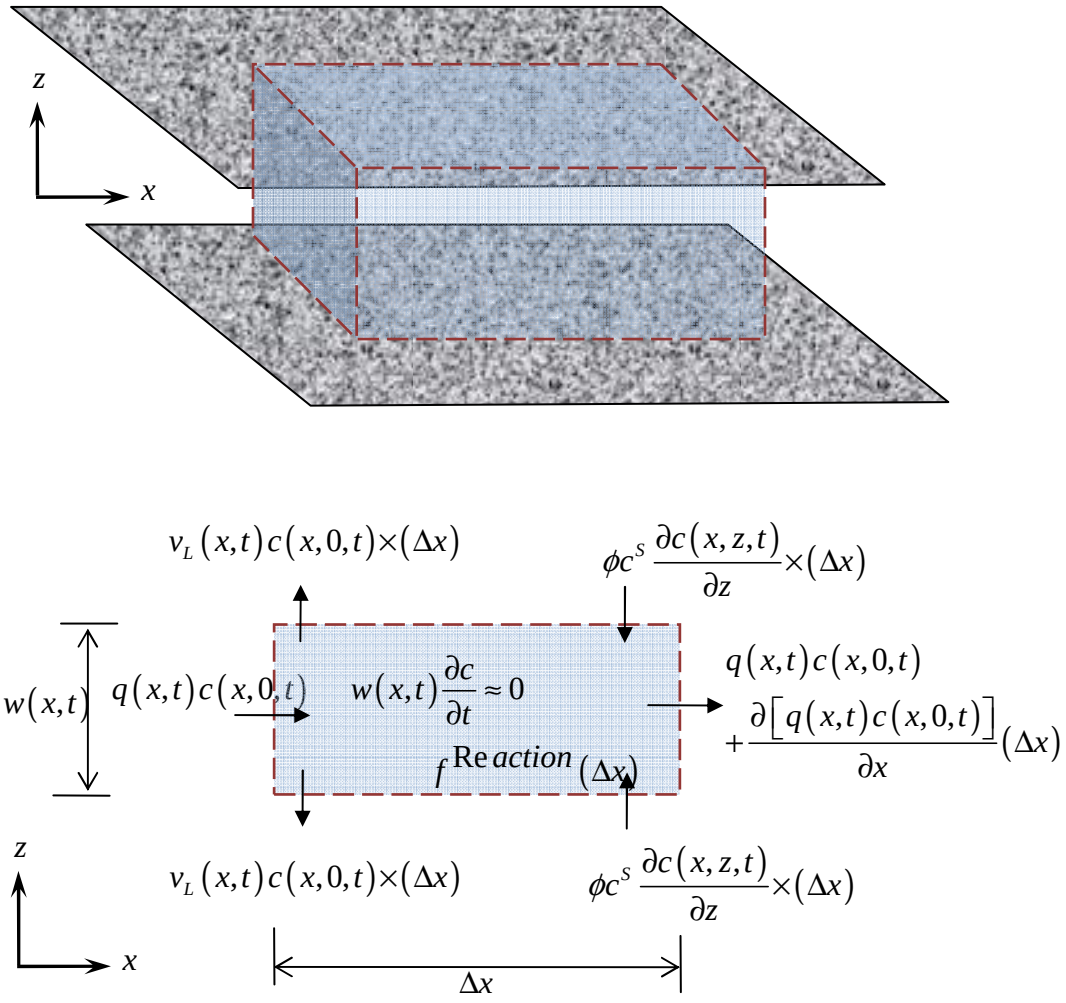

Fig. D.1 Representative elementary volume for solute mass balance in the fracture.

Assumptions:

1. Single phase fluid, single component mineral and, incompressible fluid flow
2. Flow is steady and laminar ; Darcy's law is applicable
3. Width of the fracture is much smaller than its length.
4. Solute storage and dispersion in the fracture are negligible

Assuming the linear reaction kinetics, the reaction component is written as:

$$f^{\mathrm{Re}} = -K_f\left(c(x,0,t) - c_{eq}(x,0,t)\right) \quad \text{.....(D.1)}$$

where K_f is the reaction rate constant. Similarly, c and c_{eq} are the total and equilibrium concentration. With the above assumptions, by considering the solute mass balance over a fracture segment as shown in **Fig. D.1,** the solute transport equation is:

$$-\frac{\partial\left[q(x,t)c(x,0,t)\right]}{\partial x} - 2v_L(x,t)c(x,0,t) - \frac{\partial w(x,t)}{\partial t}c(x,0,t) + 2\phi c^S \left.\frac{\partial c(x,z,t)}{\partial z}\right|_{z=0} - K_f\left(c(x,0,t) - c_{eq}(x,0,t)\right) = 0 \quad \text{.....(D.2)}$$

As derived in Appendix B, the continuity of fluid in the fracture is:

$$-\frac{\partial q(x,t)}{\partial x} - 2v_L(x,t) = \frac{\partial w(x,t)}{\partial t} \quad \text{.....(D.3)}$$

Substituting the fluid continuity equation (Eq. D.3) into Eq. D.2 and simplifying it, the solute transport equation in the fracture is obtained:

$$-q(x,t)\frac{\partial c(x,0,t)}{\partial x} - K_f\left(c(x,0,t) - c_{eq}(x,0,t)\right) = 2\phi c^S \left.\frac{\partial c(x,z,t)}{\partial z}\right|_{z=0} \quad \text{.....(D.4)}$$

Similarly, for two dimensions, Eq. D.4 can be written as:

$$\mathbf{q}(x,y).\nabla c\left(x,y,0,t\right)+2K_f c\left(x,y,0,t\right)+q_S(x,y,0,t)=2K_f c_{eq} \quad \text{……..…..(D.5)}$$

where $q_S(x,y,0,t)=-2\phi c^S \left.\dfrac{\partial c\left(x,z,t\right)}{\partial z}\right|_{z=0}$

APPENDIX E

THREE-DIMENSIONAL FUNDAMENTAL SOLUTIONS FOR THERMO-POROELASTIC MEDIA

E. 1 Continuous Displacement Discontinuity of Unit Strength

$$\sigma_{ijkn}^{cD} = \frac{G}{4\pi(1-\upsilon)}\frac{1}{R^3}\left\{(1-2\upsilon)\left(\delta_{in}\delta_{jk}+\delta_{ik}\delta_{jn}\right)-(1-4\upsilon)\delta_{ij}\delta_{kn}-15\frac{x_i x_j x_k x_n}{R^4}\right.$$
$$+\frac{3}{R^2}\left[(1-2\upsilon)\left(\delta_{ij}x_n x_k+\delta_{kn}x_i x_j\right)+\upsilon\left[\left(\delta_{ik}x_n+\delta_{in}x_k\right)x_j+\left(\delta_{jk}x_n+\delta_{jn}x_k\right)x_i\right]\right]$$
$$+\frac{\upsilon_u-\upsilon}{1-\upsilon_u}\left[\delta_{ij}\delta_{kn}\left[\left(3+\frac{3}{2\xi^2}\right)erf(\xi)-\left(8+\frac{3}{\xi^2}+8\xi^2\right)\frac{\xi}{\sqrt{\pi}}e^{-\xi^2}\right]\right.$$
$$-\delta_{ij}\delta_{kn}\left[\left(3+\frac{3}{2\xi^2}\right)erf(\xi)-\left(8+\frac{3}{\xi^2}+8\xi^2\right)\frac{\xi}{\sqrt{\pi}}e^{-\xi^2}\right] \quad \text{.....(E.1)}$$
$$+\frac{3}{R^2}\left[\begin{array}{l}\left(\delta_{ij}x_n x_k+\delta_{kn}x_i x_j\right)\left[\left(\frac{16}{3}+\frac{5}{\xi^2}+\frac{8\xi^2}{3}\right)\frac{\xi}{\sqrt{\pi}}e^{-\xi^2}-\left(1+\frac{5}{2\xi^2}\right)erf(\xi)\right]\\ +\left[\left(\delta_{ik}x_n+\delta_{in}x_k\right)x_j+\left(\delta_{jk}x_n+\delta_{jn}x_k\right)x_i\right]\left[\left(\frac{4}{3}+\frac{5}{\xi^2}\right)\frac{\xi}{\sqrt{\pi}}e^{-\xi^2}+\left(1-\frac{5}{2\xi^2}\right)erf(\xi)\right]\end{array}\right]$$
$$\left.-15\frac{x_i x_j x_k x_n}{R^4}\left[\left(\frac{8}{3}+\frac{7}{\xi^2}+\frac{8\xi^2}{15}\right)\frac{\xi}{\sqrt{\pi}}e^{-\xi^2}+\left(1-\frac{7}{2\xi^2}\right)erf(\xi)\right]\right]\right\}$$

$$p_{kn}^{cD} = \frac{G}{2\pi(1-2\upsilon)\alpha}\frac{\upsilon_u-\upsilon}{1-\upsilon_u}\frac{1}{R^3}\left\{\begin{array}{l}\delta_{kn}\left[\left(2+4\xi^2\right)\frac{\xi}{\sqrt{\pi}}e^{-\xi^2}-erf(\xi)\right]\\ +\frac{x_k x_n}{R^2}\left[3erf(\xi)-\left(6+4\xi^2\right)\frac{\xi}{\sqrt{\pi}}e^{-\xi^2}\right]\end{array}\right\} \quad \text{..... (E.2)}$$

E. 2 Continuous Point Source of Unit Strength

$$p^{cF} = \frac{1}{4\pi\kappa R} erfc(\xi) \quad \text{(E.3)}$$

$$T^{cH} = \frac{1}{4\pi K_R R} erfc(\xi) \quad \text{(E.4)}$$

$$c^{cS} = \frac{1}{4\pi\phi c^S R} erfc(\xi) \quad \text{(E.5)}$$

$$\sigma_{ij}^{cF} = \text{Coefficient}\frac{1}{R}\begin{Bmatrix} \delta_{ij}\left[\left(\frac{1}{2\xi^2}+1\right)erf(\xi) - 1 - \frac{1}{\xi\sqrt{\pi}}e^{-\xi^2}\right] \\ -\frac{x_i x_j}{R^2}\left[1 - \frac{3}{\xi\sqrt{\pi}}e^{-\xi^2} + \left(\frac{1}{2\xi^2}-1\right)erf(\xi)\right] \end{Bmatrix} \quad \text{(E.6)}$$

where

$$R^2 = x^2 + y^2 + z^2$$

$$\xi = \begin{cases} \frac{R}{2\sqrt{c^F t}} & \text{.....for fluid source} \\ \frac{R}{2\sqrt{c^T t}} & \text{.....for heat source} \\ \frac{R}{2\sqrt{c^S t}} & \text{.....for solute source} \end{cases}$$

$$\text{Coefficient} = \begin{cases} \frac{\alpha(1-2\upsilon)}{8\pi\kappa(1-\upsilon)} & \text{.....for fluid source} \\ \frac{2G\alpha_T(1+\upsilon)}{4\pi K_R(1-\upsilon)} & \text{.....for heat source} \end{cases}$$

$$E_i(u) = \int_u^\infty \frac{e^{-x}}{x} dx$$

$$erf(u) = \frac{2}{\sqrt{\pi}}\int_0^u e^{-x^2} dx \quad \text{(E.7)}$$

$$erfc(u) = 1 - erf(u)$$

$E_i(u)$, $erf\,(u)$ and $erfc(u)$ represent the exponential integral, error function and complementary error function of u

The subscripts dc and sc denotes

cD : continuous displacement discontinuity

cH : continuous heat source

cS : continuous heat source

R represents the distance between a field point and a source point, t is time and c^F, c^T and c^S represent the diffusivity for fluid, heat and solute. κ and K_R represent the permeability and rock thermal conductivity, respectively. Similarly, p, T, c and σ denote pore pressure, temperature, concentration and stress components, respectively (see Section 2).

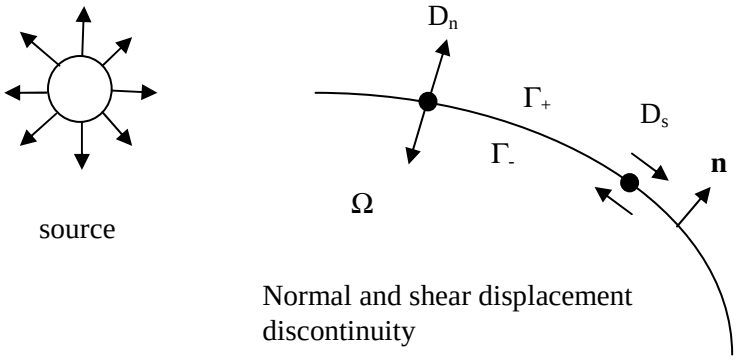

Fig. E.1 Convention of singularities.

APPENDIX F

FINITE ELEMENT SHAPE FUNCTIONS AND NODAL LOADS AND MESH

F.1 Quadrilateral

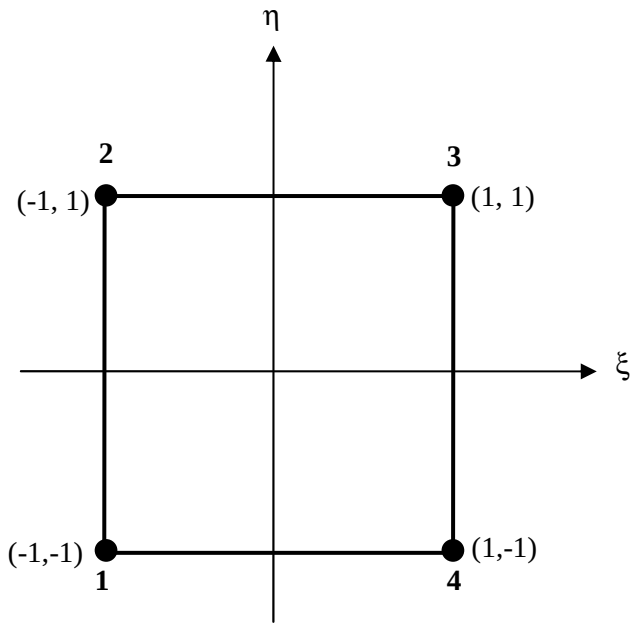

Fig. F.1 4-node quadrilateral.

$$N_1 = \frac{1}{4}(1-\xi)(1-\eta)$$
$$N_2 = \frac{1}{4}(1-\xi)(1+\eta)$$
$$N_3 = \frac{1}{4}(1+\xi)(1+\eta)$$
$$N_4 = \frac{1}{4}(1+\xi)(1-\eta)$$

……(F.1)

F.2 Hexahedron

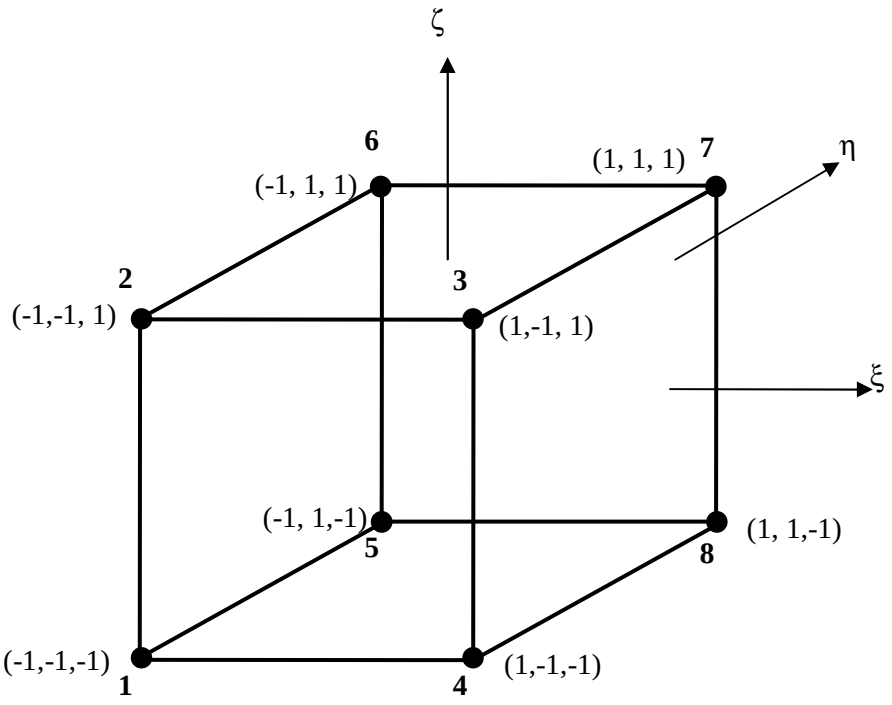

Fig. F.2 8-node hexahedron.

$$N_1=\frac{1}{8}(1-\xi)(1-\eta)(1-\zeta);\ N_2=\frac{1}{8}(1-\xi)(1-\eta)(1+\zeta)$$
$$N_3=\frac{1}{8}(1+\xi)(1-\eta)(1+\zeta);\ N_4=\frac{1}{8}(1+\xi)(1-\eta)(1-\zeta)$$ ……..……(F.2)
$$N_5=\frac{1}{8}(1-\xi)(1+\eta)(1-\zeta);\ N_6=\frac{1}{8}(1-\xi)(1+\eta)(1+\zeta)$$
$$N_7=\frac{1}{8}(1+\xi)(1+\eta)(1+\zeta);\ N_8=\frac{1}{8}(1+\xi)(1+\eta)(1-\zeta)$$

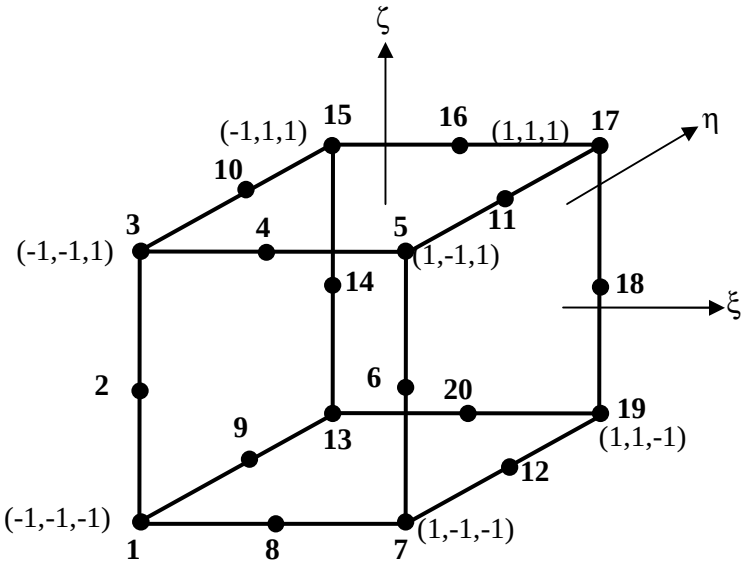

Fig. F.3 20-node hexahedron.

$$N_1=\frac{1}{8}(1-\xi)(1-\eta)(1-\zeta)(-\xi-\eta-\zeta-2);\ N_2=\frac{1}{4}(1-\xi)(1-\eta)(1-\zeta^2)$$

$$N_3=\frac{1}{8}(1-\xi)(1-\eta)(1+\zeta)(-\xi-\eta+\zeta-2);\ N_4=\frac{1}{4}(1-\xi^2)(1-\eta)(1+\zeta)$$

$$N_5=\frac{1}{8}(1+\xi)(1-\eta)(1+\zeta)(\xi-\eta+\zeta-2);\ N_6=\frac{1}{4}(1+\xi)(1-\eta)(1-\zeta^2)$$

$$N_7=\frac{1}{8}(1+\xi)(1-\eta)(1-\zeta)(\xi-\eta-\zeta-2);\ N_8=\frac{1}{4}(1-\xi^2)(1-\eta)(1-\zeta)$$

$$N_9=\frac{1}{4}(1-\xi)(1-\eta^2)(1-\zeta);\ N_{10}=\frac{1}{4}(1-\xi)(1-\eta^2)(1+\zeta) \quad \text{.....(F.3)}$$

$$N_{11}=\frac{1}{4}(1+\xi)(1-\eta^2)(1+\zeta);\ N_{12}=\frac{1}{4}(1+\xi)(1-\eta^2)(1-\zeta)$$

$$N_{13}=\frac{1}{8}(1-\xi)(1+\eta)(1-\zeta)(-\xi+\eta-\zeta-2);\ N_{14}=\frac{1}{4}(1-\xi)(1+\eta)(1-\zeta^2)$$

$$N_{15}=\frac{1}{8}(1-\xi)(1+\eta)(1+\zeta)(-\xi+\eta-\zeta-2);\ N_{16}=\frac{1}{4}(1-\xi^2)(1+\eta)(1+\zeta)$$

$$N_{17}=\frac{1}{8}(1+\xi)(1+\eta)(1+\zeta)(\xi+\eta-\zeta-2);\ N_{18}=\frac{1}{4}(1+\xi)(1+\eta)(1-\zeta^2)$$

$$N_{19}=\frac{1}{8}(1+\xi)(1+\eta)(1-\zeta)(\xi+\eta-\zeta-2);\ N_{20}=\frac{1}{4}(1-\xi^2)(1+\eta)(1-\zeta)$$

F3. Equivalent Nodal Loads in 2D

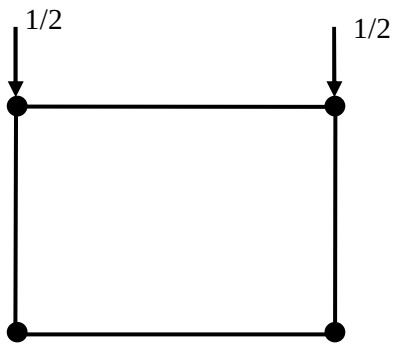

Fig. F.4 Nodal loads in 4-node quadrilateral.

F4. Equivalent Nodal Loads in 3D

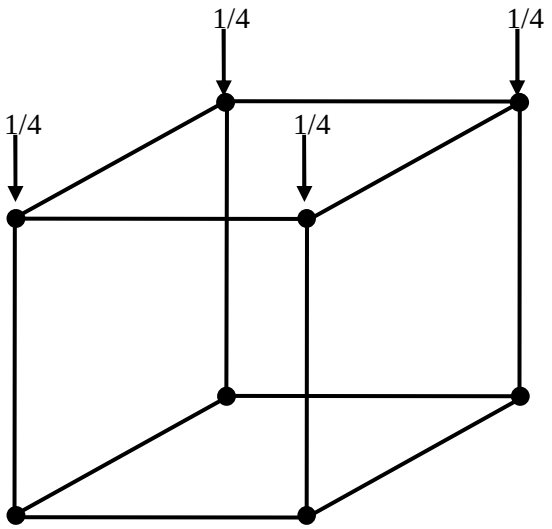

Fig. F.5 Nodal loads in 8-node hexahedron.

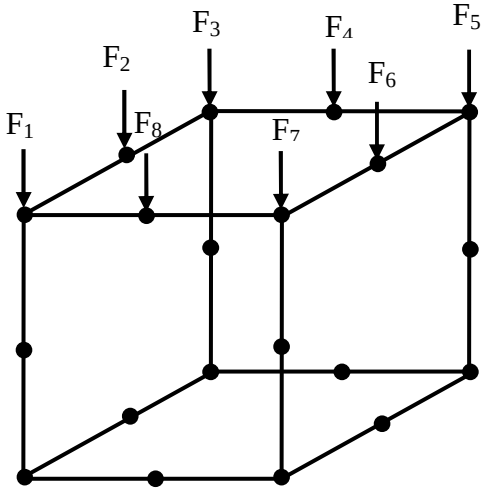

$$F_1 = F_3 = F_5 = F_7 = -\frac{1}{12}$$

$$F_2 = F_4 = F_6 = F_8 = \frac{1}{3}$$

Fig. F.6 Nodal loads in 20-node hexahedron.

APPENDIX G

SENSITIVITY ANLYSIS OF EXAMPLE PRESENTED IN SECTION 5.1

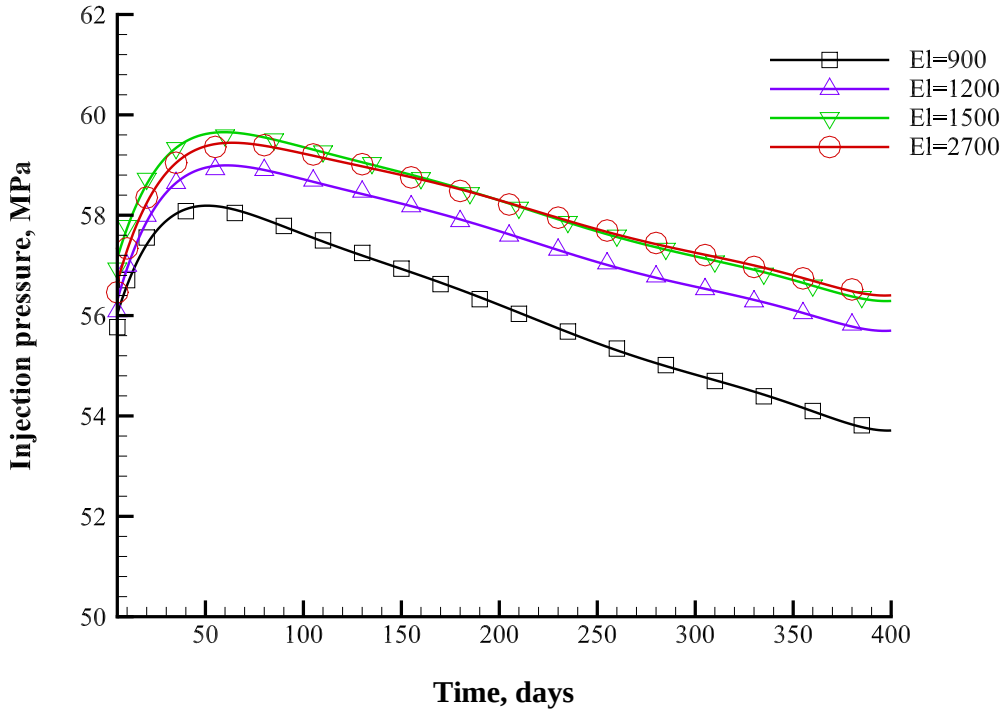

Fig. G.1 Computed injection pressure using different fracture elements.

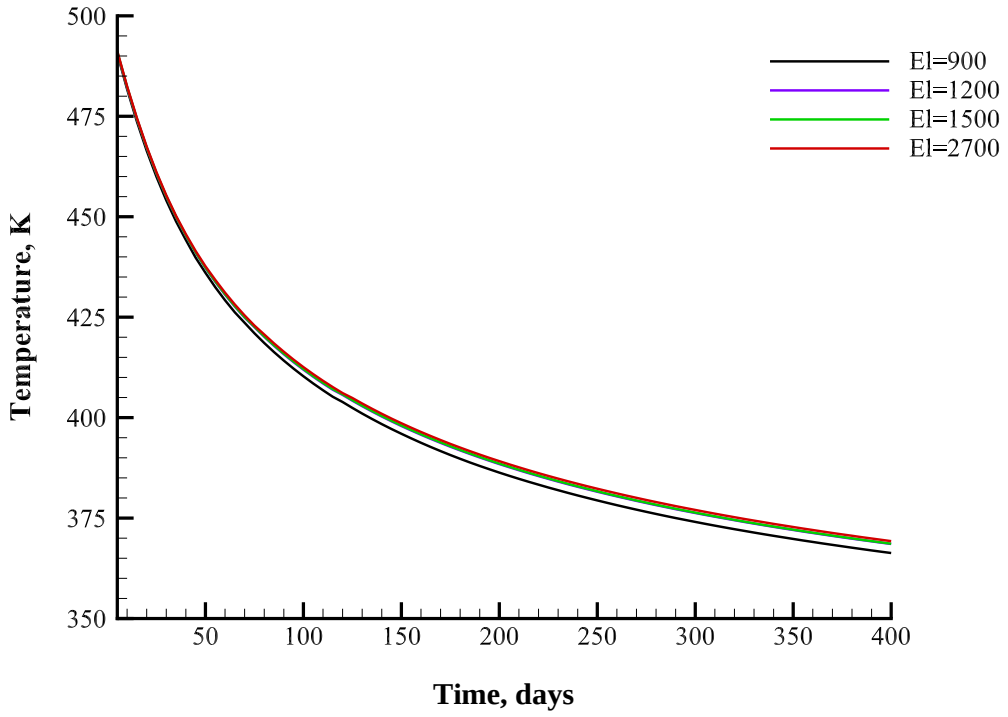

Fig. G.2 Computed extraction temperature using different fracture elements.

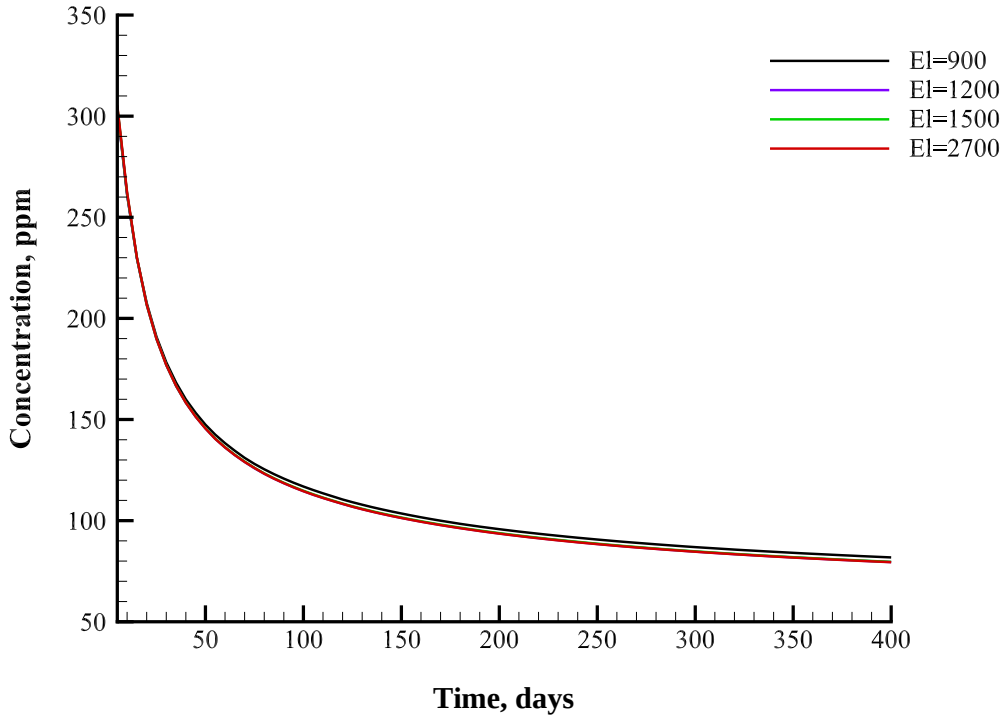

Fig. G.3 Computed extraction fluid concentration using different fracture elements.

VITA

Name:	Chakra Rawal
Address:	Harold Vance Department of Petroleum Engineering,
	3116 TAMU, College Station, TX 77843-3116
Email Address:	rawalchakra@gmail.com
Education:	B.E., Civil Engineering, Tribhuvan University, 2003
	M.Sc., Water Resources Engineering, Tribhuvan University, 2006
	Ph.D., Petroleum Engineering, Texas A&M University, 2012
Affiliation:	Society of Petroleum Engineers
	American Rock Mechanics Association
	Honor Society of Pi Tau Epsilon